High Efficiency Solar-based Catalytic Structure for CO₂ Reforming

FINAL REPORT

Reporting Period:

10/01/2010-09/30/2013

DE-FE0004224

SUBMITTED BY

PhosphorTech Corporation 3645 Kennesaw North Industrial Pkwy Kennesaw, Ga 30144

PRINCIPAL INVESTIGATOR

Hisham Menkara Phone: 404-664-5008 Fax: 770-828-0672 E-mail: hisham@phosphortech.com

SUBMITTED TO

William O'Dowd
U.S. Department of Energy
National Energy Technology Laboratory
PO Box 10940
626 Cochrans Mill Road
Pittsburgh, PA 15236
412-386-4778

01/10/2014

DISCLAIMER: "This report was prepared as an account of work sponsored by an agency of the United States Government. Neither the United States Government nor any agency thereof, nor any of their employees, makes any warranty, express or implied, or assumes any legal liability or responsibility for the accuracy, completeness, or usefulness of any information, apparatus, product, or process disclosed, or represents that its use would not infringe privately owned rights. Reference herein to any specific commercial product, process, or service by trade name, trademark, manufacturer, or otherwise does not necessarily constitute or imply its endorsement, recommendation, or favoring by the United States Government or any agency thereof. The views and opinions of authors expressed herein do not necessarily state or reflect those of the United States Government or any agency thereof."

Table of Contents

Abstract	2
Executive Summary	3
Statement of Project Objectives (SOPO):	7
Tasks Progress	8
Task 1.0 Project Management and Planning	8
Task 2.0 Development & Optimization of Solution-based Thin-film Processes	8
Task 3.0 Development & Fabrication of PN Structure for CO ₂ reduction	25
Task 4.0 Refinement of CO ₂ reactor	47
Task 5.0 Build and Demonstrate CO ₂ Reactor Prototype	74
List of Significant Accomplishments	82
Conclusions & Future Roadmap	84
References	86

Abstract

Throughout this project, we developed and optimized various photocatalyst structures for CO_2 reforming into hydrocarbon fuels and various commodity chemical products. We also built several closed-loop and continuous fixed-bed photocatalytic reactor system prototypes for a larger-scale demonstration of CO_2 reforming into hydrocarbons, mainly methane and formic acid. The results achieved have indicated that with each type of reactor and structure, high reforming yields can be obtained by refining the structural and operational conditions of the reactor, as well as by using various sacrificial agents (hole scavengers). We have also demonstrated, for the first time, that an aqueous solution containing acid whey (a common bio waste) is a highly effective hole scavenger for a solar-based photocatalytic reactor system and can help reform CO_2 into several products at once.

The optimization tasks performed throughout the project have resulted in efficiency increase in our conventional reactors from an initial 0.02% to about 0.25%, which is 10X higher than our original project goal. When acid whey was used as a sacrificial agent, the achieved energy efficiency for formic acid alone was ~0.4%, which is 16X that of our original project goal and higher than anything ever reported for a solar-based photocatalytic reactor. Therefore, by carefully selecting sacrificial agents, it should be possible to reach energy efficiency in the range of the photosynthetic efficiency of typical crop and biofuel plants (1-3%).

Executive Summary

In the first year of this project, we developed and optimized various photocatalyst structures for CO₂ reforming into hydrocarbon fuel products. We confirmed that Degussa P25 exhibits the best performance in an equivalent structure compared to other commercial TiO2 products. Several types of substrates were also investigated, including pure titanium mesh, but the focus in the first year was primarily on copper (Cu) substrates, which were proven to have very high methane (CH4) yield and selectivity for CO2 reforming by solar-based photocatalysis. In addition, we pursued the development of narrow bandgap (NBG) materials for increased solar absorption and have successfully synthesized CdS nanorods/tetrapods grown over CdSe nanocrystal seeds, which were capable of sunlight absorption up to 600 nm. During all experiments involving Cu substrates, it was again noticed that the methane yield decreased as the photocatalytic reaction progressed. Examination of the Cu substrates revealed that some zones became dark, as a result of the formation of CuO and graphitic carbon from CO2 and oxidation reactions, which were confirmed by EDS analysis. We have also demonstrated that, by choosing a specific structure, we are able to exercise some degree of control over the hydrocarbon product selectivity resulting from CO2 photocatalytic reforming activity. The reforming activities from several metal-semiconductor structures were compared. In the case of the simple TiO2/Cu structure, only methane was detected as a result of reforming CO2 and H2O by light. However, when other semiconductor layers were introduced, we also detected additional formation of what appears to be formic acid (CH2O2), which is the result of hydrogenation of CO2 by the H+ ions formed from H2O. In some semiconductor structures, only formic acid was formed and no methane, which confirmed our ability to selectively control the formation of these two useful hydrocarbons. Formic acid, also known as methanoic acid, is an important intermediate in a variety of chemical synthesis processes and is also used as a fuel in some proton exchange membrane fuel cells (PEMFC). We have also investigated visible light-driven narrow-bandgap (NBG) photocatalysts and corresponding PN structures. Several new types of substrates and solution-based deposition processes were examined for the purpose of growing various nano-structures for CO2 reforming under sunlight. We successfully synthesized CdSe/CdS nanocrystals capable of sunlight absorption up to 650 nm. Additional nanorod structures of TiO2 on titanium mesh were also fabricated and some catalytic activity was detected under UVA light, but the performance of such structures under sunlight was still low compared to P25 Degussa nano-particles on titanium mesh. We've also increased our efforts into the evaluation of metal-oxide NBG materials and structures, which were deemed more suitable for solar energy harvesting. One particular heterojunction developed and evaluated, during the first year of this project, showed significant potential for CO2 reforming into methane (CH4) under sunlight radiation. A PN junction formed between CuO (n-type) and Cu2O (p-type) materials grown on a copper (Cu) substrate has yielded the highest selectivity and reforming activity to date for methane (CH4) production under sunlight radiation. As a result, we have demonstrated two significant achievements during Q3. One using commercial P25 TiO2 on titanium substrates and the other using a metal-oxide NBG heterojunction formed with copper oxide semiconductors (Cu2O/CuO) and copper metal. Both structures have shown significant catalytic activity under sunlight. These enhanced effects were attributed to the overall 3-dimensional reactor structure employed as well as the NBG characteristics of the copper oxides, which enabled the absorption of a significant portion of the visible and near-IR solar radiation. Another important factor in the high activity of the Cu2O/CuO system is believed to be due to the built-in electric field in the PN structure, which provides for better separation of electron-hole pairs and reduced recombination rates.

In addition, we also evaluated new metal/oxide structures as well as various nanorods of TiO2 grown by both solution and thin-film processes. After completing the first Year 1 milestone regarding the demonstration of various solution-based nanocrystal synthesis and deposition processes, we then extended our synthesis of CdSe nanocrystals and have been able to demonstrate core-shell systems of various dimensionalities. We've shown that the 3-dimensional structures of these nanocrystals such as tetrapods offer significant optical and thermal advantages compared to the conventional quantum dots (QDs) or even the nanorods (NRs) structures. Furthermore, following completion of our second Year 1 milestone regarding the development of post-deposition heat treatment processes for TiO2 photocatalyst structures, we pusued the development of the solution-based process for fabricating titania nanorod arrays on the surface of titanium mesh. We modified the former preparation method to improve the physical properties of the titania nanorods, such as improved mechanical stability and layer resistance to peeling. It was found that the amount of CH4 produced through CO2 reforming from the titania nanorod array system continuously increased during 168 hours (7 days) inside a closed reactor where samples were collected daily. The cumulative CH4 concentration was found to be about 3330 ppmV after 168 hours of photocatalysis by a UVA lightbulb. In addition, FTIR spectra showed that formic acid was also present in relatively high amounts.

During the second year of this project, we continued the development and optimization of various photocatalyst structures for CO2 reforming into hydrocarbon fuel products. We also evaluated various low-cost substrate materials that offer the potential for increased stability and oxidation resistance for long-term photocatalytic reactor operation. After we completed one of our Year 2 milestones regarding the development and optimization of the computer modeling for the PN structure, continuing on previously reported work, we had extended our simulation to include a 3-layer heterostructure composed of CeO2-CuO-TiO2 systems that offer enhanced oxidation resistance for Cu-based photocatalyst structures. The model was validated experimentally using oxidation experiments on CeO2-coated copper substrates compared to uncoated copper. We've also developed various new metal-oxide structures that exhibit high CO2 reforming activity into formic acid as well as good long-term stability. Such structures included green NiO as well as NiO/TiO2 structures on nickel substrates, which has the ability to absorb visible sunlight energy. We have also demonstrated strong CO2 reforming activity on simple structures that involve P25 Degussa TiO2 coated on stainless steel meshes. Finally, a quantitative FTIR analysis and calibration were performed using a commercial formic acid compound that enabled us to accurately estimate the formic acid yield from the various photo catalytic experiments.

In addition, we continued the development and optimization of various photocatalyst structures for CO₂ reforming into hydrocarbon fuel products. We evaluated new and

promising low-cost structures that showed high reforming yields under visible light irradiation. Specifically, we had expanded our work on simple structures that involve P25 Degussa TiO₂ coated on stainless steel meshes and performed analysis to better understand their high yields under visible light. We found that the TiO₂/steel mesh system is a promising solar-driven photocatalytic system for converting CO₂ and water into formic acid. Such a semiconductor-metal system seems to better utilize solar energy including both UV and visible light for reasons that we will explain later. We've also investigate new semiconductor/metal systems based on tungsten trioxide (WO₃) on copper as well as stainless steel, which can also absorb visible light and can be relatively stable (on steel) for long operations. Furthermore, by optimizing catalyst loading and substrate size, we enhanced the photocatalytic activity of the Degussa P25 titaniastainless steel mesh system under sunlight conditions. As a result, we have demonstrated a CO₂ reactor energy efficiency under natural sunlight equivalent to 15x10⁻³ %, which is 3X higher than the 5x10⁻³ % value reported by Nishimura. We found that, among the different substrate materials investigated, including copper, aluminum, bronze, brass, nickel, and stainless steel, the stainless steel substrate is still considered to be the most suitable metal substrate to support a PN junction using titania as a wide bandgap photocatalyst to produce formic acid from CO₂ and water.

Moreover, we had built a continuous fixed-bed photocatalytic reactor system for a largerscale demonstration of CO₂ reforming into formic acid. We've also modified the previously developed titania-stainless steel structure by deposition of NiCr thin-films on the surface of the stainless steel substrate, so as to further improve the properties of such system for CO₂ reforming. In addition, we fabricated and tested a PN structure prototype based on the optimized TiO₂/Cu model previously reported in the Q5 report where the copper substrate was modified by deposition of CeO₂ to protect from oxidation during the photocatalytic reaction. NiCr thin-films were also deposited by electron beam evaporation on copper substrates, which were later coated with P25 titania. Both the CeO₂ as well as he NiCr modified copper mesh systems have shown more stable and longer-term photocatalytic activity, as predicted by previous models. However their initial reforming yields were lower than those achieved using standard titania-copper systems. In addition, on the second year of this project, we have delivered an invited presentation at the 2012 Energy Materials Nanotechnology Meeting in Orlando, FL and were invited to present at Heterogeneous Catalysis Symposium, ACS Philadelphia Meeting in August 2012.

During the third year of this project, we built & tested a continuous modular photocatalytic reactor system for CO₂ reforming into formic acid and continued optimizing the radiator-style solar reactor prototype built in Q8. We've also demonstrated that the Ni/Cr surface-modified titania-stainless steel heterostructure enhances the stability of the substrate and protects the iron content from oxidation (rust formation), even following 500°C thermal treatment in air for 1 hour. In addition, we demonstrated a one-pass solar-based reforming of CO₂ into formic acid using a modular reactor system made of 10 units of stainless-based photocatalytic structures connected in series with a total length around 150 inches and inner diameter less than 0.5 inch. In addition, we tested the effectiveness of our previously developed modular photocatalytic reactor system for CO₂ reforming using gas feedstock containing lower concentrations of CO₂ gas in order to simulate conditions comparable to flue gas sources. The outcome of the

experiments conclusively demonstrated that a titania-stainless alloy heterostructure can also reform gas mixtures containing low concentrations of CO₂ into a formic compound. In addition, we've also continued work on improving the titania-stainless system by modifying it with Ni/Cr nanostructures via post heat treatment processes and have shown that such structures can increase the reforming efficiency of CO₂ in a continuous circulation reactor system. We have also demonstrated that our pilot-scale CO₂ reforming solar reactor can be operated in a continuous circulation mode using both low and high concentrations of CO₂ and at higher gas flow rates. The results achieved with varying gas flow rates have indicated that higher reforming yields can be obtained by optimizing the various operational conditions of the reactor such as gas flow rate, CO₂ concentrations, as well as the optimal levels of the sacrificial agent. Therefore, there exists a wide range of operational variables that will need to be studied and optimized for a given reactor design, which could lead to even higher performance.

Finally, we demonstrated, for the first time, the ability of our solar photocatalytic reactor to quickly reform CO₂ into several fuels and chemicals using a common waste source (as a sacrificial agent) and without any other artificial chemicals or a water source. Acid whey, an environmentally toxic and widely available (150 million gallons are produced annually by the US Northeast alone) by-product of the dairy industry, was used as the only agent in the reaction. The results were confirmed under natural sunlight as well as artificial UV and solar simulator lighting. There are still many unexplained observations such as an unprecedented 50% drop in CO₂ levels in under 3 hours and several yet unidentified products. In addition to the usual formic acid, we have so far identified the presence of methanol, methane, formaldehyde, and carbon monoxide. Considering only formic acid, our low-end estimate of energy efficiency (EE) is at around 0.4%, which is about 2X higher than the best EE achieved to date using isopropyl alcohol (common sacrificial agent) and 16X higher than our originally proposed target. Once all other products are accounted for, we anticipate the total EE will be much higher than 0.4% and might even exceed the photosynthetic efficiency of typical crop and biofuel plants (1-3%).

A photocatalytic reactor based on this approach will be far more superior to all biofuel technologies since it can be implemented in any geographic region, including deserts, and will not require an arable land. In addition, the photosynthetic pigments of plants cannot utilize the UV, green, and infrared portions of the solar radiation, while a photocatalytic reactor can be designed to do so. Finally, it is well known that photosynthesis is most efficient at low light intensities and will saturate at 20% of full sunlight, while a photocatalytic reactor increases in efficiency at higher intensities and temperature, as demonstrated throughout our project as well numerous published work.

In summary, not only have we completed all the proposed objectives and goals of this project, but in addition have demonstrated the possibility of further yield improvements through continuous optimization of various operation parameters and the introduction of commonly available sacrificial biomass agents (such as acid whey) into the reactor. Considering that acid whey, a waste biomass, is a widely available by-product of the dairy industry worldwide, it has proven to be a very effective hole scavenger candidate for large scale commercial implementation of a solar-based CO₂ reforming reactor.

Statement of Project Objectives (SOPO):

Objectives

The objective of this project is to develop and demonstrate a novel CO₂ catalytic structure having high CO₂ reduction potential, high absorption in the visible part of the solar spectrum, and high utilization of infrared solar energy. The structure will be built using commercially available nanocrystalline materials of TiO₂ and narrow-bandgap (NBG) semiconductors and quantum dots (QDs). A low-cost solution manufacturing as well as a higher-cost vacuum deposition processes will be developed and optimized to achieve a thin-film semiconducting p-n structure with optical and electrical properties consistent with those of high quality single crystal films. The program will be divided into three phases, as follows:

Phase I: Development & optimization of low-cost solution-based thin-film Coating processes

- <u>Objectives</u>: to develop solution-based thin-film coating processes for controlled and uniform coating of TiO_2 and NBG semiconductors on various substrates. Optical and physical properties will be measured and optimized.

Phase II: Development, fabrication, & characterization of p-n structures for CO₂ reduction

- <u>Objectives</u>: to develop and fabricate p-n structures using optimized thin-films from Phase I and any available high-quality thin-films from Phase III. CO₂ reduction properties of the structures will be determined and ideal planar structure and reactor unit geometries will be defined.

Phase III: Refinement of CO₂ reactor and prototype demonstration

- <u>Objectives</u>: to build a CO₂ reactor prototype and refine p-n structure using more complex vacuum deposition technologies that promote polycrystalline or columnar structures in order to compare performance with low-cost solution-deposition. This will help determine upper CO₂ reduction limits of the technology and evaluate the costs and benefits of using vacuum deposition.

Scope of Work

The scope of the proposed work is to develop a process and a structure that will achieve an efficient p-n semiconductor junction between the n-type TiO_2 and p-type NBG semiconductors. The objectives of this program will be accomplished if the multilayer structure can successfully function as a high absorber of sunlight radiation as well as an efficient e-h separator, which will significantly reduce the e-h recombination rate. As is well known, e-h recombination losses dominate in conventional nano-sized photocatalysts. Therefore, by coupling the photocatalyst with another semiconductor having favorable energetics, charge separation can be greatly improved.

In order to achieve such structures, two types of thin-film deposition techniques will be explored: (1) solution-based techniques using dispersed nanocrystals such as electrophoretic deposition, spray pyrolysis, dip coating, or polymer-assisted deposition; and (2) vacuum deposition techniques such as thermal and e-beam evaporation of solid targets, gas sources, and/or plasma. The various techniques will be followed by high temperature annealing to improve layer crystallinity and carrier diffusion rates. The first approach is being performed at the PhosphorTech Corporation (PTC) using existing capabilities, while the second approach is being investigated at the Georgia Tech Research Institute (GTRI), which has a comprehensive thin-film vacuum deposition and characterization capabilities.

Tasks Progress

Task 1.0 Project Management and Planning

PhosphorTech has managed the project in accordance with the details provided in the original project management plan (PMP).

Task 2.0 Development & Optimization of Solution-based Thin-film Processes

2.1 Preparation of Nanocrystal Solutions

In this project, various types of CdSe/ZnSe/CdTe narrow-bandgap (NBG) nanocrystals were fabricated and analyzed. Their optical and electrical properties (emission color and bandgap) along with particle size distribution were analyzed using UV/Vis fiber optic spectrometers and a Delsa Nano particle size analyzer. Zn/CdSe were grown by colloidal epitaxy in inert atmosphere (Argon) at temperatures below 300°C. As illustrated in Figure 1, longer synthesis time leads to increased particle size and shift of absorption properties to longer wavelengths, therefore enabling improved harvesting of solar light energy.

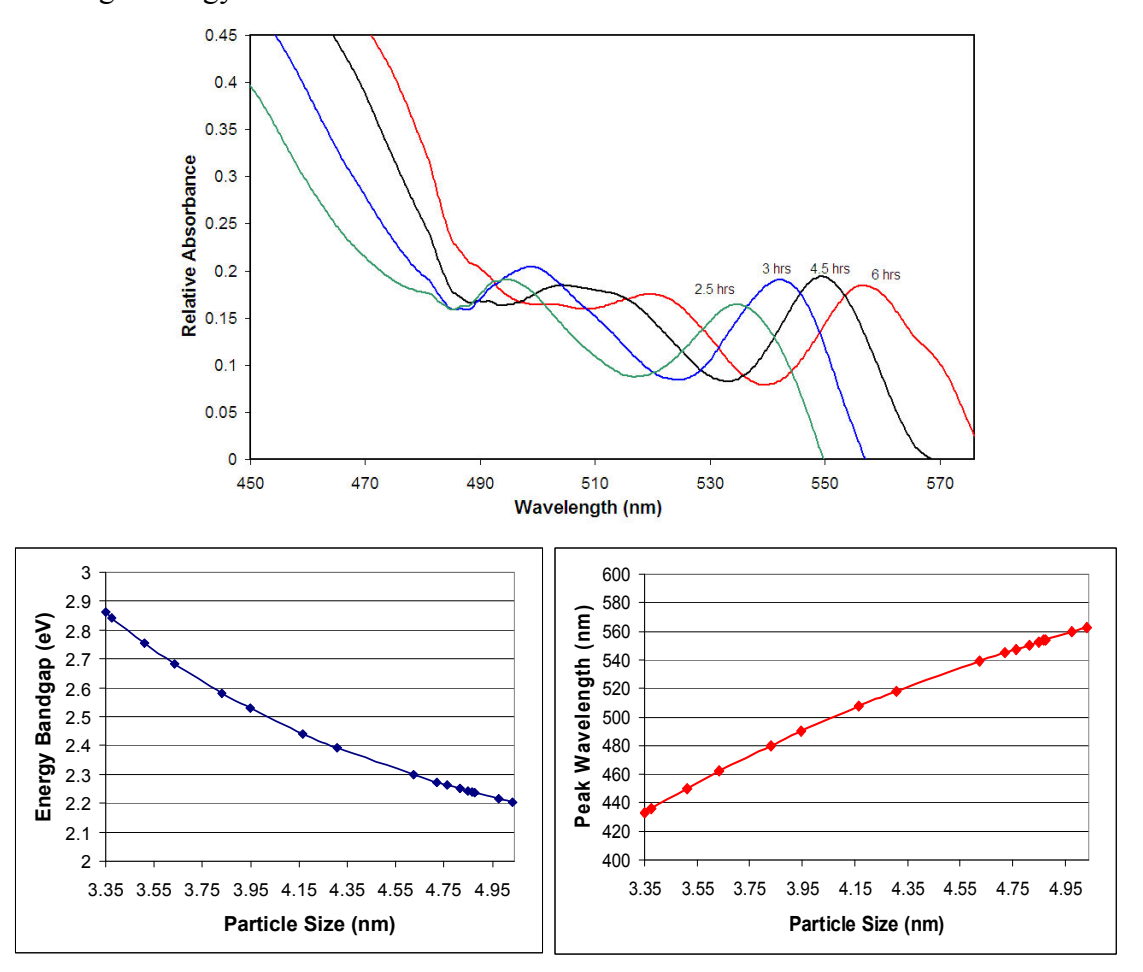


Figure 1. Top: Absorbance plots showing effect of particle size increase on visible light

absorption properties of Zn/CdSe nanocrystals. Bottom: Dependence of energy bandgap and peak emission wavelength on CdSe particle size

In addition, cadmium selenide and sulfide nanocrystals of various sizes capable of light absorption up to wavelengths of 600nm have been synthesized (Figure 2). The size of the synthesized nanocrystals was controlled by varying the types/equivalents of ligands used, nucleation and growth temperature and the growth time. Moreover, we had also synthesized heterogeneous nanostructures involving CdS, CdSe, ZnSe and TiO₂, because such heterogeneous nano-structured systems can enhance absorption of light in the visible region and facilitate the transfer of this energy towards photo-catalytic reactions and photocurrent generation. Seeded growth techniques were adapted to synthesize heterogeneous nano-structures. The pink line in Figure 2 shows absorbance of cadmium sulfide nanorods/tetrapods grown over CdSe nanocrystal seeds and the blue line in Figure 2 shows absorbance of cadmium sulfide grown over titanium dioxide nanoparticle seeds.

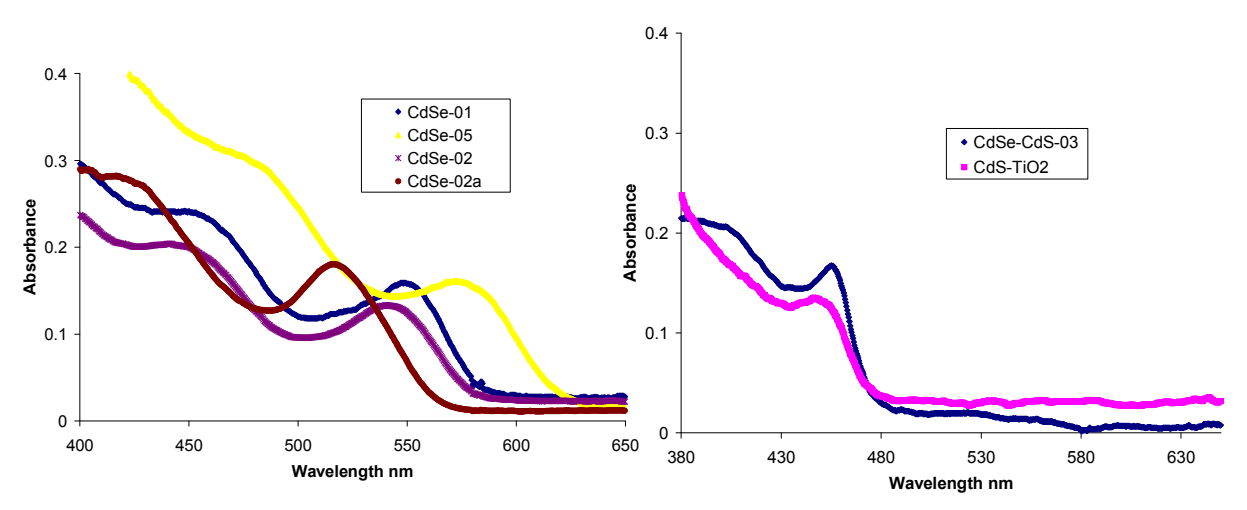


Figure 2. Left: Cadmium selenide nanocrystals of various sizes absorbing at various wavelengths. Right: Absorption spectra of nano heterostructures: CdS on TiO₂ (Pink), CdS on CdSe (Blue)

In a typical synthetic procedure, cadmium oxide with known equivalents of alkyl phosphonic acid or fatty acid and dodecylamine or hexadecylamine was weighed out in a three necked flask along with 1-octadecene. The middle neck of the flask was fitted with a condenser connected to a Schlenk line while a temperature probe connected to a temperature controller is fixed through one of the side necks and a septum cap on the third neck of the flask. The flask was placed over a heating mantle kept on a stirrer and its contents were de-gassed under stirring for 90 minutes at 120°C. The flask was then refilled with nitrogen and the temperature of the reaction mixture was raised to 310°C and maintained at 310°C until the contents of the solution becomes clear within 60 minutes. In a separate septum capped vial with a stir bar, selenium was dissolved in trioctylphosphine, de-gassed for 30 minutes and re-filled with nitrogen. Once the solution becomes clear the temperature was set at 290°C and selenium solution in trioctylphosphine from the vial was drawn into a syringe fitted with a 12 gauge needle

and injected rapidly into flask containing the reaction mixture. The temperature drops on injection and is then maintained between 260°C and 270°C. The growth of the nanocrystals is monitored by periodic sampling of the reaction contents and analyzing their absorption and emission spectra in a uv-visible spectrophotometer. Once the desired size is achieved, heating was stopped and the reaction mixture was cooled down. The contents of the reaction flask were then collected in a centrifuge tube. Acetone/methanol was used to precipitate the nanocrystals from crude reaction mixture before re-dispersing them in toluene or hexanes.

In the seeded growth technique used to grow CdSe/CdS nanorods/tetrapods, previously synthesized CdSe nanocrystal seeds were introduced along with sulfur in trioctylphosphine during injection at temperatures between 300 and 330°C to a degassed concentrated solution (~0.4M) of cadmium oxide and alkylphosphonic acid ligands that facilitate rod/tetrapod growth in a flask (prepared as in the case of synthesizing CdSe nanocrystals) in an inert atmosphere. To grow heterogeneous nanostructures of cadmium sulfide on titania, commercially available titania nanocrystal seeds were included along with the cadmium oxide precursor solution in the flask and sulfur in trioctylphosphine was injected at high temperature.

The synthetic methods adapted for quantum dots and nanorods/tetrapods involve utilizing readily available relatively less expensive and less reactive precursors and are being tested for reproducibility and scalability. Though the synthesis is carried out under air-free conditions, the processing methods adapted to purify the nanocrystals are done in aerobic atmosphere and the purified nanocrystals are found to be stable for months at room temperature and atmosphere. In addition, we had also studied the utility of these synthetic methods to synthesize cadmium-free nanomaterials. Preliminary current-voltage studies using a prototype structure made using the synthesized heterogeneous nanostructures of cadmium sulfide on titania deposited on indium tin oxide show a mild increase in photocurrent on exposure to blue light indicating possible transfer of energy from cadmium to titania.

Furthermore, we have extended our synthetic methodology to synthesize CdSe nanocrystals absorbing up to 650nm. Figure 3 (Top Left) shows the absorption spectra of CdSe nanocrystals of various sizes. The nanocrystals synthesized are found to be stable at ambient laboratory conditions for several months. Considering that there has been an enhanced interest in utilizing heterogeneous nanostructures in energy harvesting applications, we have also developed methods to synthesize two-component nanorod structures involving cadmium selenide and cadmium sulfide (CdSe/CdS). Seeded growth methods were adapted in synthesizing these materials. The cadmium selenide nanocrystals synthesized as represented above were used as nanocrystal seeds over which cadmium sulfide rod structures were grown. In such a heterogeneous nanostructure, the absorption wavelength of cadmium selenide seed shifts further into the red region due to the de-localization of electron and hole wave functions into the cadmium sulfide rod while cadmium sulfide rod component contributes mostly to the absorption of light below 500nm. A typical absorption spectrum of CdSe/CdS nanorods is shown in Figure 3 (Top Right) with a mild absorption peak due to CdSe seed around 590nm.

We further extended the synthesis of cadmium selenide nanocrystals by attempting synthesis of cadmium selenide sulfide (CdSeS) nanocrystals. Figure 3 (Bottom Left) shows the absorption spectra of CdSeS nanocrystals synthesized during Q3. The size of

these materials could be tuned by merely adjusting the ratio of selenium and sulfur precursors to that of the cadmium precursors. The size distribution of these materials are relatively narrow compared to the CdSe nanocrystals as can be inferred from the relatively sharp absorbance peaks that are obtained from the solutions.

In addition, we've also recently attempted cadmium sulfide rod growth using CdSeS seeds and obtained an interesting new nanomaterial (CdSeS/CdS) with absorption spectrum as represented in Figure 3 (Bottom Right). Similar to the CdSe/CdS nanorod structure, we do see a red shift in the absorption wavelength of the CdSeS seeds added in this case indicating the formation of a heterogeneous nanostructure

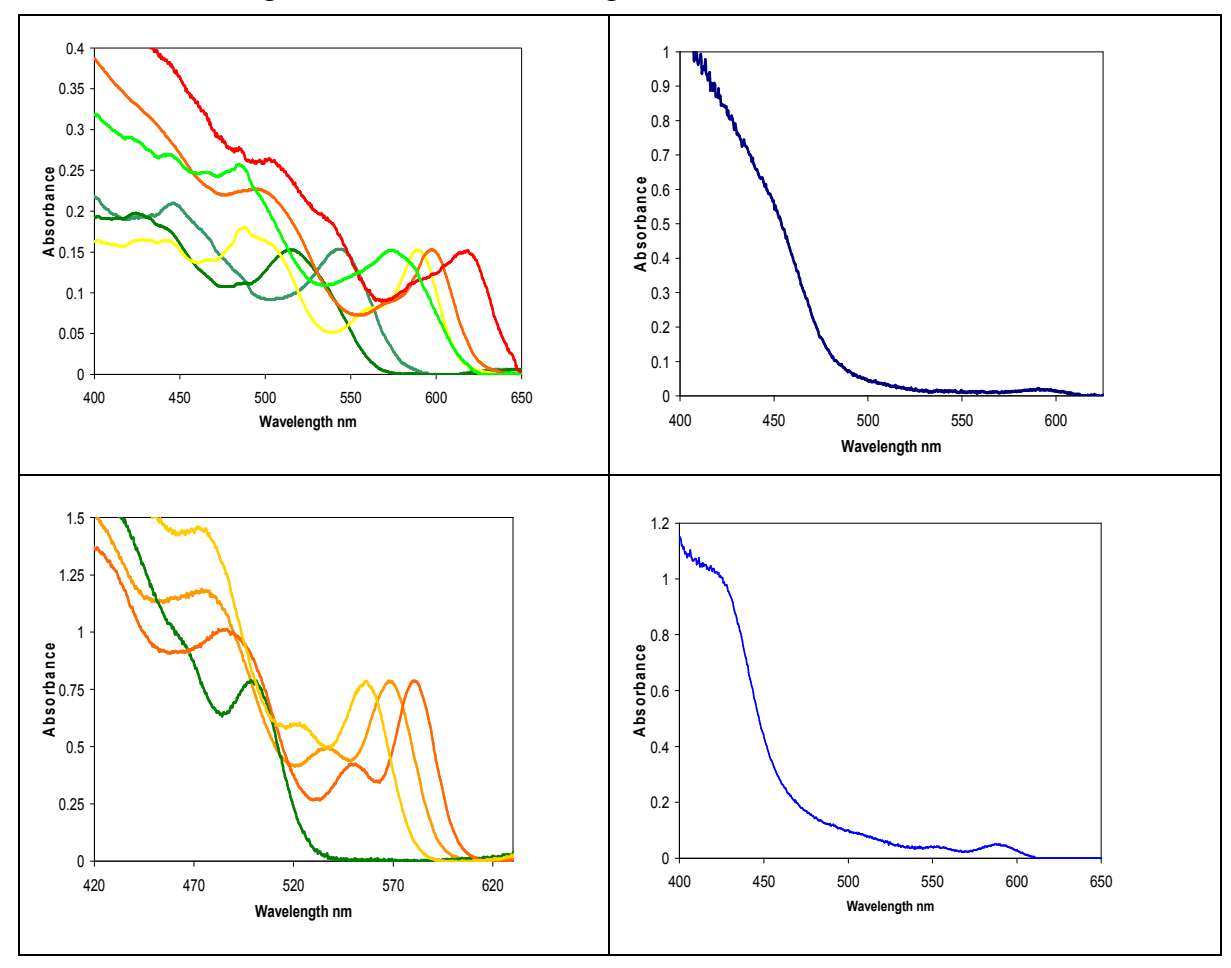


Figure 3. Top Left: Cadmium selenide nanocrystals of various sizes absorbing up to 650nm. Top Right: Absorption spectrum of CdSe/CdS nanorods, Bottom Left: Cadmium sulfide/selenide nanocrystals of various sizes absorbing up to 590nm. Bottom Right: Absorption spectrum of CdSeS/CdS heterostructure

Experimental methods:

In a typical synthetic procedure, cadmium oxide with known equivalents of alkyl phosphonic acid or fatty acid and dodecylamine or hexadecylamine was weighed out in a three necked flask along with 1-octadecene. The middle neck of the flask was fitted with

a condenser connected to a Schlenk line while a temperature probe connected to a temperature controller is fixed through one of the side necks and a septum cap on the third neck of the flask. The flask was placed over a heating mantle kept on a stirrer and its contents were de-gassed under stirring for 90 minutes at 120°C. The flask was then refilled with nitrogen and the temperature of the reaction mixture was raised to 300°C (250C if amines are used as co-solvents) and maintained at 300°C (250C when amines are used as co-solvents) until the contents of the solution becomes clear within 60 minutes. In a separate septum capped vial with a stir bar, selenium was dissolved in trioctylphosphine, de-gassed for 30 minutes and re-filled with nitrogen. Once the solution becomes clear the temperature was set at 290°C and selenium solution in trioctylphosphine from the vial was drawn into a syringe fitted with a 12 gauge needle and injected rapidly into flask containing the reaction mixture. The temperature drops on injection and is then maintained between 260°C and 280°C during the nanocrystal growth. The growth of the nanocrystals is monitored by periodic sampling of the reaction contents and analyzing their absorption and emission spectra using a UV-visible spectrophotometer. Once the desired size is achieved, heating was stopped and the reaction mixture was cooled down. The contents of the reaction flask were then collected in a centrifuge tube. Acetone/methanol was used to precipitate the nanocrystals from crude reaction mixture before re-dispersing them in toluene or hexanes.

The synthesis of CdSeS nanocrystals involved a similar procedure with injection done between 270 and 288°C. The primary difference is the injection solution which contains known ratios of sulfur and selenium dissolved in trioctylphosphine. To prepare this injection solution, known quantities of sulfur is first dissolved in trioctylphosphine by mild heating and then selenium is dissolved into the same solution at room temperature. The contents of the vial are degassed and refilled with nitrogen before injection.

In the seeded growth technique used to grow CdSe/CdS nanorods/tetrapods, previously synthesized CdSe nanocrystal seeds dispersed in octadecene (~0.05M) were injected a minute after the injection of sulfur in trioctylphosphine at temperatures between 300 and 330°C to a degassed concentrated solution (~0.4M) of cadmium oxide and alkylphosphonic acid ligands that facilitate rod/tetrapod growth in a flask in an inert atmosphere. To grow heterogeneous nanostructures of cadmium sulfide on CdSeS, CdSeS nanocrystals dispersed in octadecene (~0.05M) were injected one minute after the injection of sulfur in trioctylphosphine at 315°C into the flask and allowed to grow for 10 minutes.

In addition, we have extended our methodology to synthesize CdSe nanocrystals and have been able to demonstrate core-shell systems of various dimensionalities. The 3-dimensional structures of these nanocrystals such as tetrapods offer significant advantages compared to the conventional quantum dots (QDs) or even the nanorods (NRs) structures, as illustrated in Figure 4. The added spatial dimensionality of the tetrapod structures results in complete separation between emission and absorption (large Stokes shift) while increasing their chemical and thermal stability. Figure 4 (left) shows the relative thermal stability of the various structures as the dimensionality is increased from zero (quantum dots) to three (tetrapods). Figure 4 (middle) shows the effect on optical properties where a complete separation between emission and absorption can be

achieved using tetrapods, which will help maximize the energy transfer efficiency of these systems compared to conventional quantum dots. These complex structures were synthesized using seeded growth solution methods where CdSe nanocrystals were used as nanocrystal seeds over which CdS multirod structures were grown. The size and shape of these structures could be changed by adjusting the ratio of Se/S precursors relative to that of the Cd precursors.

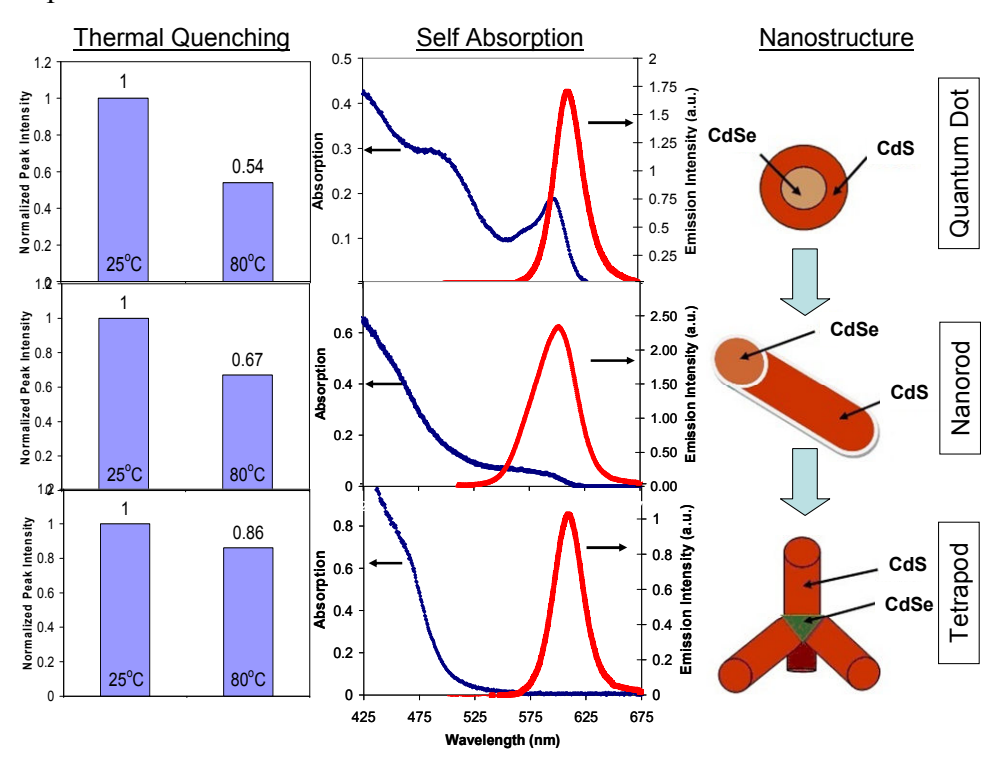


Figure 4. CdSe/CdS nanocrystals of various shapes illustrating the optical and thermal advantages of the higher dimensionality materials.

2.1.1 Deposition & Heat Treatment Process for TiO₂

During Q4 period, we employed titanium mesh as a substrate to support titania (TiO₂) films attached to the mesh using a sol gel method followed by post-deposition heat treatment inside a furnace. The surfactant self-assembling sol gel method can produce porous titania films with high BET surface area and pore volume, which is beneficial to absorbing larger amounts of CO₂ and water for the photocatalytic reduction reaction. The porous titania films were immobilized on the surface of a coarse titania mesh using a dip coating sol gel process, which is performed by employing Tween 20 as a template. Following film deposition, the coated titanim mesh was then heat treated and calcined at 500 °C in air to achieve proper TiO₂ crystallization and oxidation. FTIR analysis results on these structures showed that primarily formic acid (CH₂O₂) is produced from CO₂ and H₂O by such a porous TiO₂/Ti mesh structure under UV radiation (refer to Figure 5).

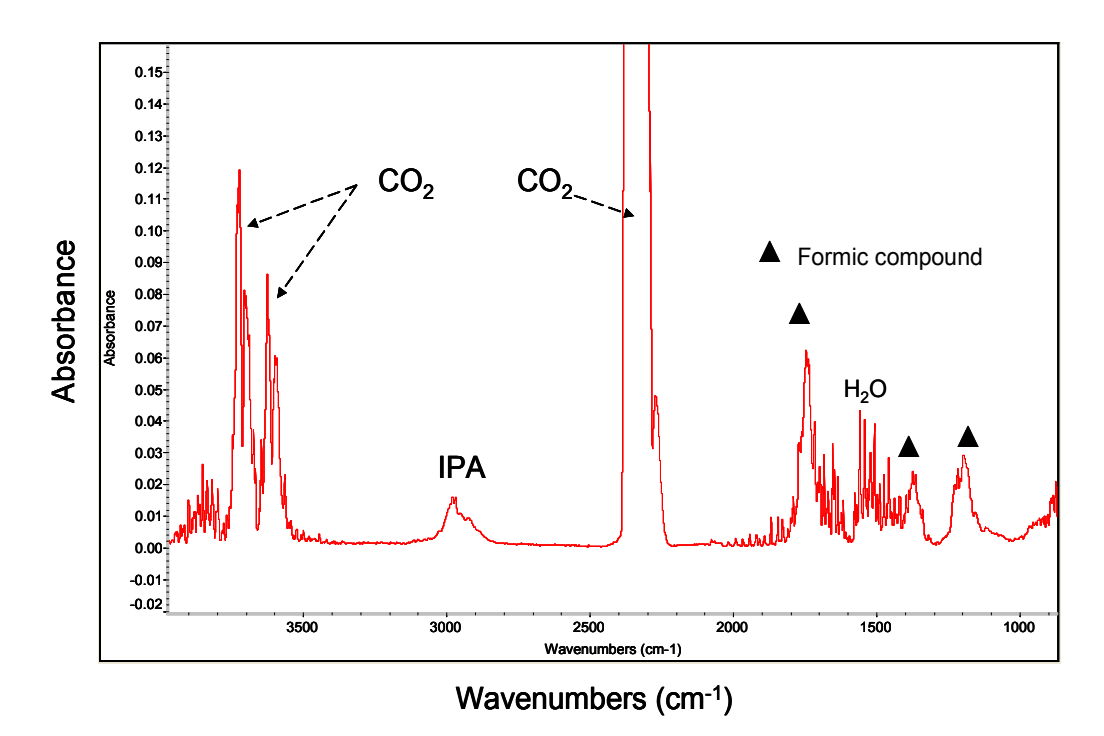
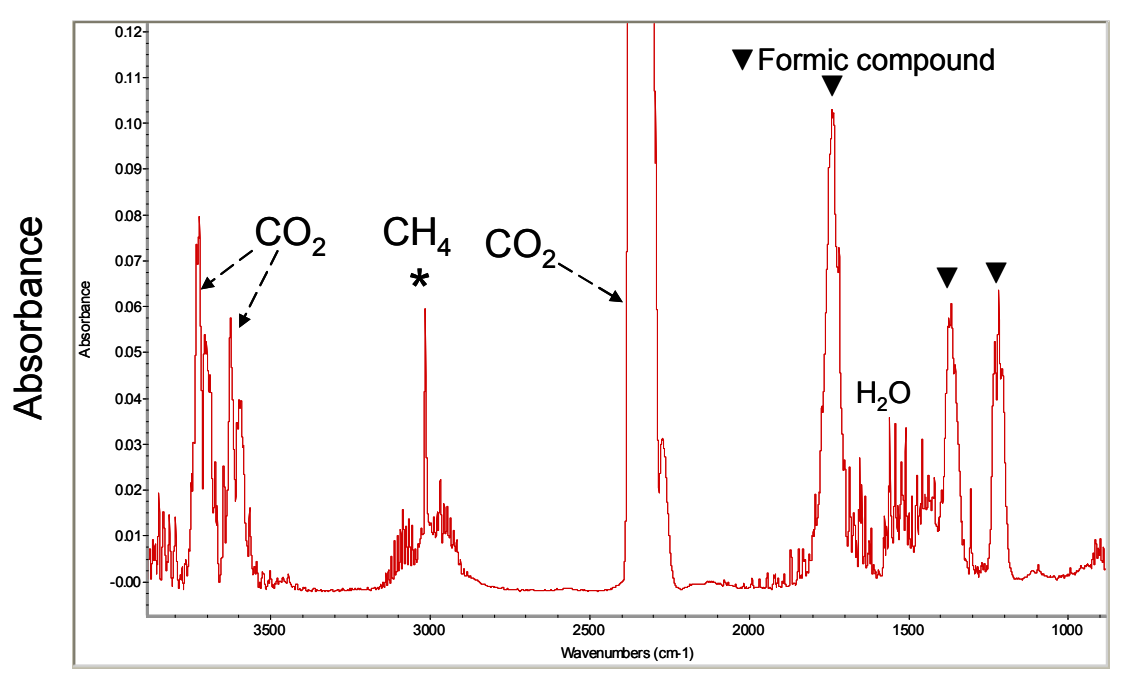


Figure 5 FTIR spectra of gas composition in the photocatalytic reactor with 0.0792 g porous titania film attached on titanium mesh (1.8õ7 inches) after 72 hours of UVA radiation from a 6W bulb.

During Q4 period, we also continued the development of the solution-based process for fabricating titania nanorod arrays on the surface of titanium mesh. We modified the former preparation method to improve the physical properties of the titania nanorods, such as improved mechanical stability and layer resistance to peeling. We employed 50 V bias for the anodization process instead of the previous 60 V, in order to decrease titania nanorod lengths and growth rates. Figure 7(a) shows a low (250X) magnification SEM image of the TiO₂-coated titanium mesh, while Figure 7(b) shows a higher (5,000X) magnification cross section image of that the titania nanorod array, with an average length of about 10 µm, about 40% shorter than those previously prepared by the 60 V anodization process. It was also found that the amount of methane produced through CO₂ reforming from this titania nanorod array system continuously increased during 168 hours (7 days) when samples were monitored daily. The amount of methane was found to be about 3330 ppmV after 168 hours of UV photocatalysis. The FTIR analysis also showed that formic acid was present in relatively high amounts, as shown in Figure 6.



Wavenumbers (cm⁻¹)

Figure 6 FTIR spectra of gas composition in the photocatalytic reactor with titania nanorod-titanium mesh system after UVA radiation of 168 hours (7 days) from a 6W bulb.

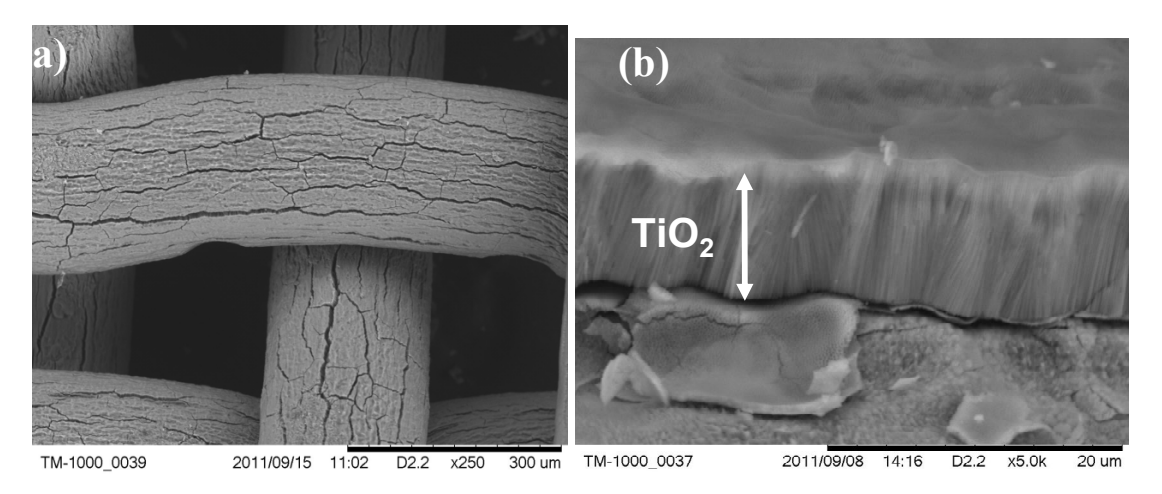


Figure 7 SEM images of titania nanorod-titanium substrate. (a) Low magnification and (b) high magnification

2.2 Evaluation of Commercial TiO₂

Several types of commercial TiO_2 nanocrystals were evaluated in various forms. Two were purchased as nano-sized powders: <25nm anatase Aldrich TiO_2 (200-220 m²/g) and ~20nm Degussa Aeroxide P-25 (35-65 m²/g). Another TiO_2 was purchased as an aerosol spray from Bioizer Technologies. The nano-powder materials were dispersed in an aqueous solution containing few percent of isopropyl alcohol (IPA) and were

continuously mixed using a magnetic stirrer. Thin layers of TiO₂ were then coated on different substrate materials such as 1) Copper (Cu), 2) Stainless steel (SS), 3) Bronzeplated Cu, 4) Silver-plated Cu mesh, and 5) Nickel-plated Cu. The TiO₂-coated substrates were then placed inside various forms (rectangular, cylindrical, large/small volumes) of glass or quartz mini-reactors purged and filled with 100% CO₂ gas from an Airgas cylinder. The reactors were then exposed to illumination from an un-filtered blacklight for periods ranging from 15 minutes to over a week in some cases. Gas samples were frequently taken from the reactors using a syringe through the rubber septa seal on the reactors. The gas samples were then analyzed inside a 10cm glass gas cell using a Fourrier Transform Infrared Spectroscopy (FTIR) system. The most effective reactor for yielding quick CO₂ reforming data by FTIR was the cylindrical glass or quartz tubing with volumes ranging from 30 to 100 ml. Furthermore, the CO₂ reforming to methane gas (CH₄) results varied significantly depending on the type of TiO₂ and substrate material used in the experiments, as illustrated by the FTIR results shown in Figure 8. No CH₄ activity was detected on TiO₂-coated stainless steel substrate. Both Cu and Ag-plated Cu substrates exhibited significant activity (>500 ppmV/hr of CH₄), while Nickel- and Bronze-plated substrates showed very little activity (~10 ppmV/hr of CH₄). While most experiments appeared to produce graphitic carbon residues on the substrates following light exposure, the production of high levels (hundreds of ppm) of CH₄ was more challenging and only occurred under very specific (yet repeatable) conditions. So far, these conditions are in good agreement with and appear to confirm the validity of our cynlindrical reactor design concept that was originally proposed to the DOE and is currently patent-pending.

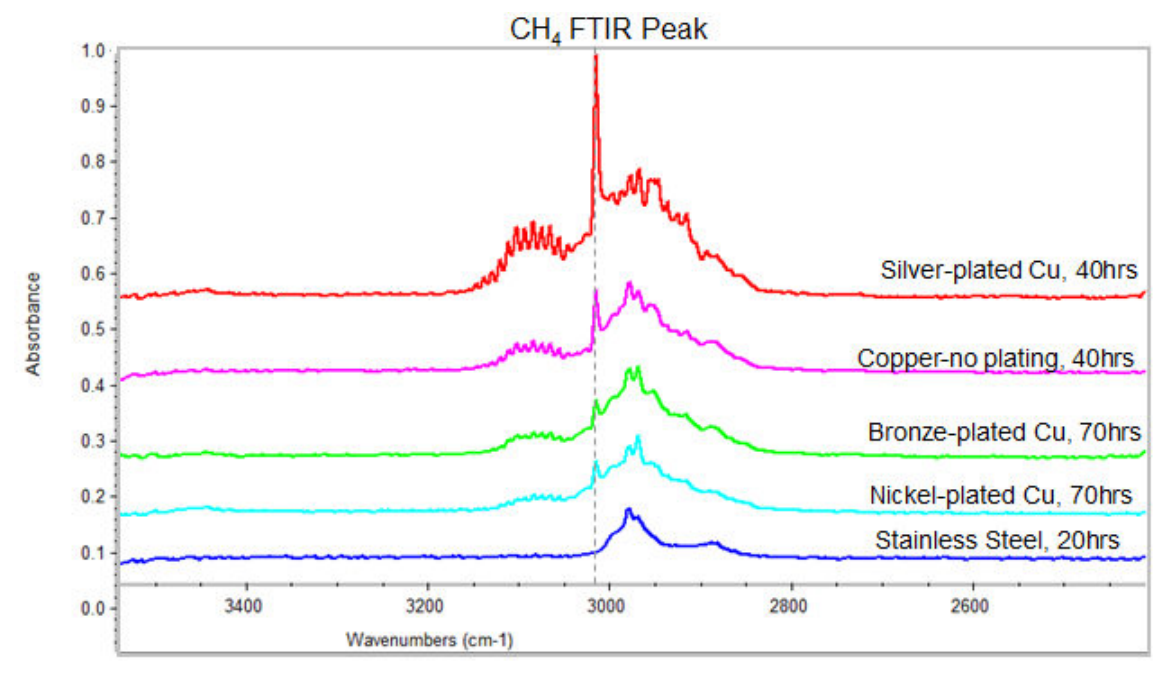


Figure 8. Comparison of CH₄ evolution from CO₂ using P25 Degussa TiO₂ on various types of substrate materials exposed to a 6W blacklight for the durations shown

After completing the evaluation of commercial TiO_2 (titania) nanocrystals, we studied Cu substrates, which exhibited some of highest reforming activity and selectivity to date. The photocatalytic CO_2 reforming activity of the different types of commercial titania were compared by measuring and analyzing fixed volumes of gas samples by FTIR taken from similar reactors (with different titania) following the same UVA exposure time and intensity. It was found that, among these commercial photocatalysts, Degussa P25 titania presented the best photocatalytic activity under UVA excitation. Our study showed that, using Degussa P25/copper system, the methane yield could reach 165 μ L/(g.h), which is among the highest reported CO_2 to CH_4 reforming yields 4,5,6,7 (this result had been presented at the 242nd ACS conference in September 2011. Therefore, Degussa P25/copper system has a high selectivity for the production of methane from CO_2 .

During the experiments, it was also noticed that methane yield decreased after a longer photocatalytic reaction time (i.e., after 167 hours). After UV photocatalysis, some zones on the copper substrate supporting Degussa P25 titania became dark, which seems to be induced by the formation of CuO and graphitic carbon formed from CO₂. Figure 9 and Table 1 show the results from the EDS analysis of Degussa P25 titania/copper substrate after UV photocatalysis. 50.1% (atomic) of carbon and 17.1% (atomic) of oxygen in the titania/copper can be observed. Such results support the above conclusion on the formation of copper oxide and carbon on the surface of the metal substrate, which may act as barriers to further photocatalytic reactions.

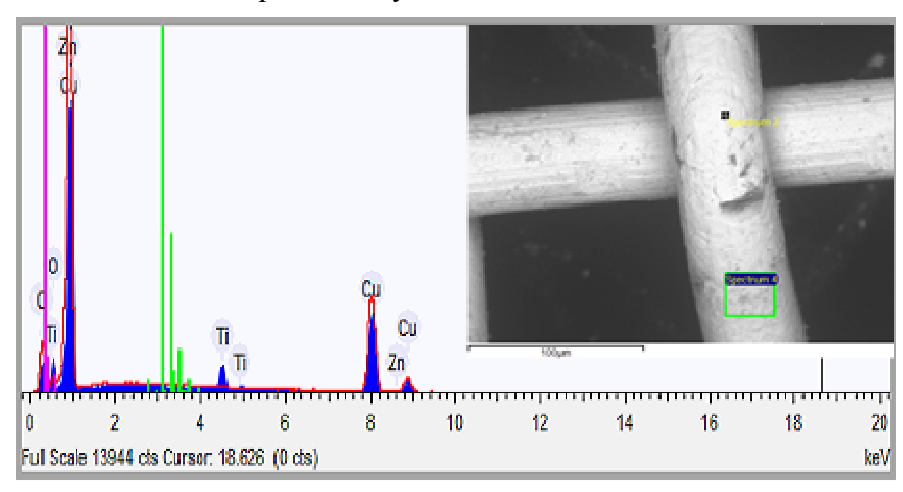


Figure 9. EDS spectra of Degussa P25 titania/copper substrate after photocatalytic reaction (inserted graph: SEM image of DegussaP25 coating attached on copper mesh)

Table 1. Summary	Results of I	EDS Analysis
------------------	--------------	--------------

Element	Weight %	Weight % σ	Atomic %
Carbon	20.641	0.386	50.108
Oxygen	9.400	0.235	17.132
Titanium	4.575	0.090	2.785
Copper	63.115	0.434	28.963
Zinc	2.268	0.377	1.012

2.2.1 Photocatalytic reduction of CO₂ into methane under sunlight radiation

Figure 10 demonstrates that, using batch reactor module, methane can be produced from CO₂ via photocatalysis with commercial degussa P25 on copper mesh under

sunlight radiation.

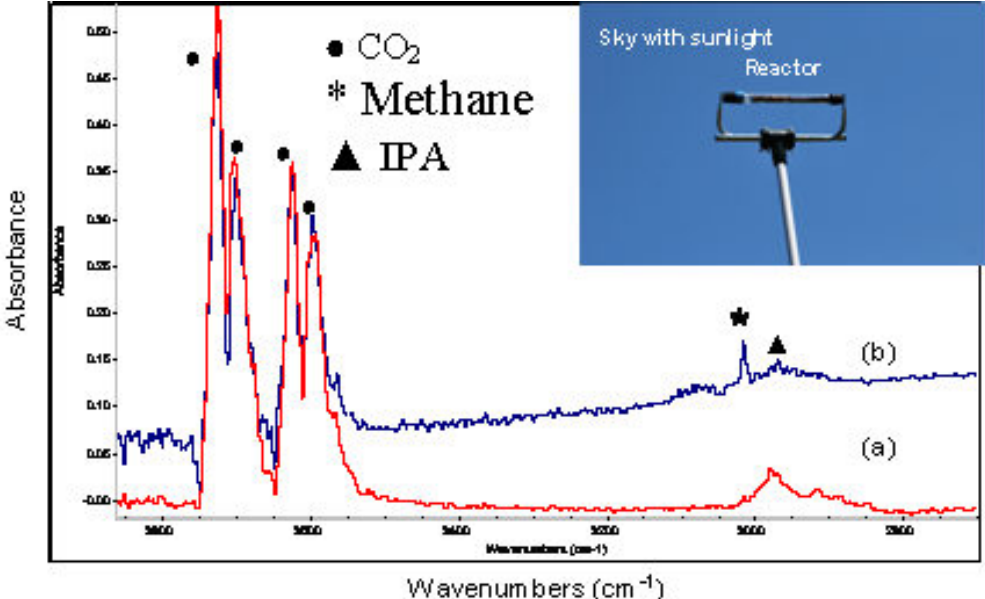


Figure 10. FTIR spectra of gas composition in the photocaytalytic reactor with 0.05 g Degussa P25 titania/copper mesh after sunlight exposure. (a) after 3.5 hours sunlight radiation, and (b) after 14 hours sunlight radiation under partly cloudy conditions

2.2.2 Employing titanium metal mesh as a substrate to support titania catalysts

In addition, we investigated photocatalytic activity of titania attached on titanium metal mesh as a support via dip coating operation and follow-up heat treatment procedure (500 °C). The primary disadvantage of such an approach is the relatively higher cost of titanium metal compared to more conventional metals such as copper.

Considering that titania nanotubes have many advantages over titania powders, such as higher BET surface area and less resistance for electron transfer due to decreased numbers of boundaries among titania particles, we've also explored an electrochemical method for the synthesis of titania nanotubes.9 Figure 11 shows SEM images of titanium metal after anodization and calcinations at 500 degree. Under high magnification (c), one can easily see the high porosity of the titania coating, while the nanorod length was established to be around 10 μm .

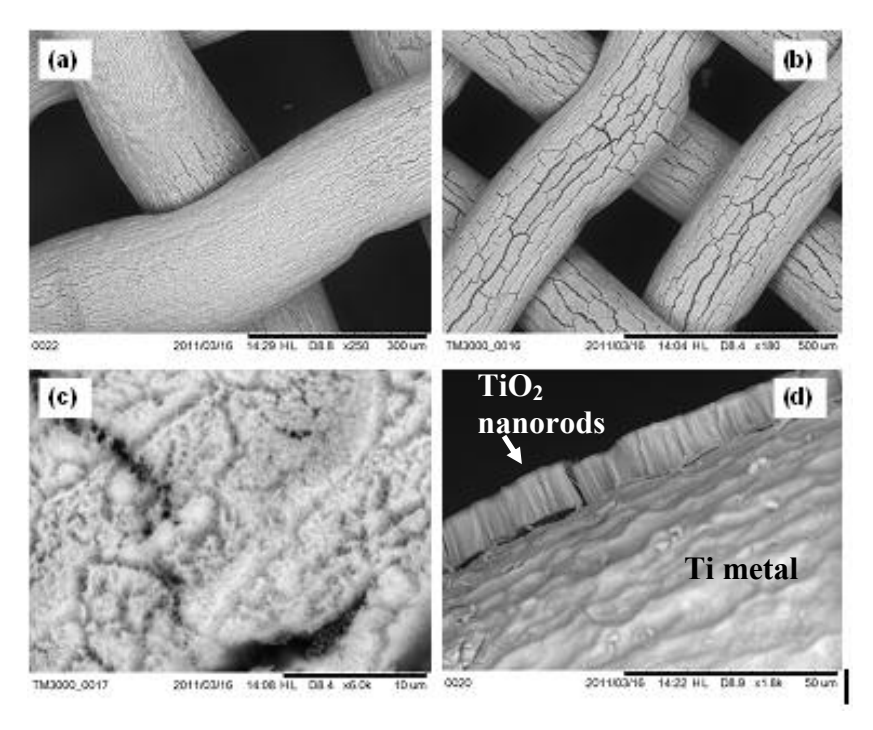


Figure 11. SEM images of titanium meshes after anodization and calcinations at 500 $^{\circ}$ C. (a) 2.5 inches anodization distance, (b) 1 inch anodization distance, low magnification, (c) 1 inch anodization distance, high magnification, and (d) cross-section SEM image showing 10 μ m long nanorods

Figure 12 and Table 2 show the results from the EDS analysis of an anodized titanium substrate after calcination at 500°C. The high levels of oxygen detected on the surface of the metal support the above conclusion on the formation of titanium dioxide.

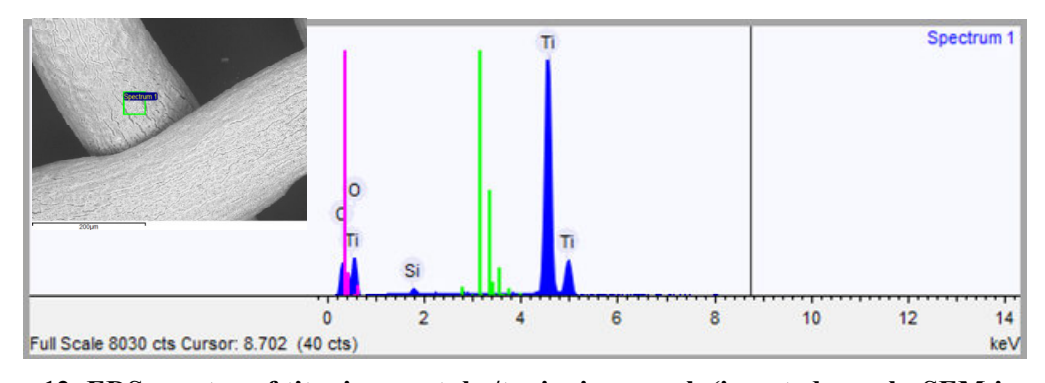


Figure 12. EDS spectra of titania nanotube/tanianium mesh (inserted graph: SEM image of titania nanotube/tanianium mesh).

Table 2. Summary Results of EDS Analysis

Element	Weight %	Weight % σ	Atomic %
Carbon	12.171	0.269	24.191
Oxygen	32.105	0.534	47.907
Silicon	0.369	0.032	0.314
Titanium	55.354	0.468	27.588

Figure 13 shows the experimental FTIR results from a reactor structure fabricated by depositing 0.045 g Degussa P25 titania on a fine titanium mesh for reforming CO₂ and water into methane. The absorbance value of the methane peak corresponds to 1977 ppmV of methane produced under sunlight radiation during a period of 10 hours. This corresponds to a methane production rate of 382 uL/h.g-catalyst, which exceeds (1.4X) the highest CO₂ to hydrocarbon production rate ever reported in the literature from TiO₂ photocatalysts. ^{10,11,12,13,14} We believe that such a high methane production rate is due to (1) the three dimensional network structure of semiconductor-metal system developed at PhosphorTech, and (2) the mixed crystalline phase (anatase and rutile) of Degussa P25 photocatalyst. It has also been reported that the addition of metal particles such as copper and platinum can work as co-catalysts with titania to further improve the photocatalytic activity on the titanium substrate. Therefore, we believe these results using this highly stable structure can be further improved in the future.

Moreover, we also fabricated titania nanotubes attached to the titanium mesh and tested their photocatalytic activity. The results are shown in Figure 14 and Figure 15. It can be seen that the as-prepared titania nanotubes do exhibit photocatalytic activity for reforming CO₂ and water into methane under both UVA and sunlight radiation.

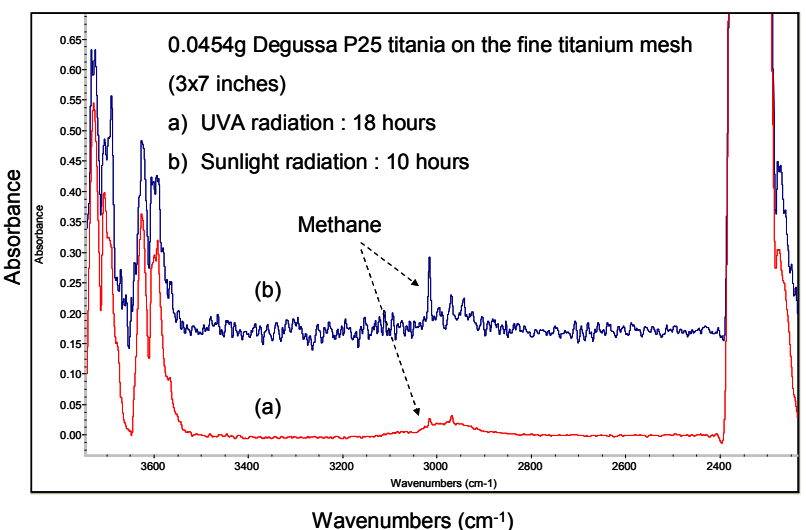


Figure 13. FTIR spectrum of gas composition in the photocaytalytic reactor with 0.045 g Degussa P25 titania photocatalyst attached to fine titanium mesh and exposed to (a) UVA radiation from 6W lamp for 18 hours and (b) sunlight radiation for 10 hours (power density ~100 mW/cm²).

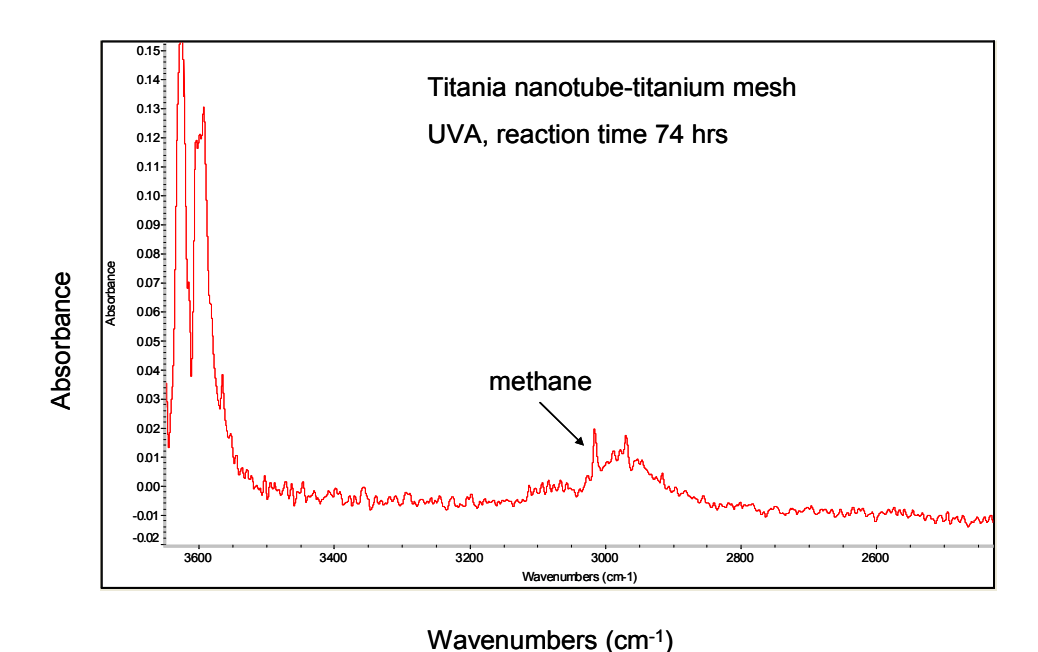


Figure 14. FTIR spectrum of gas composition in the photocaytalytic reactor with titania nanotubes gown on coarse titanium mesh. UVA radiation time: 74 hours

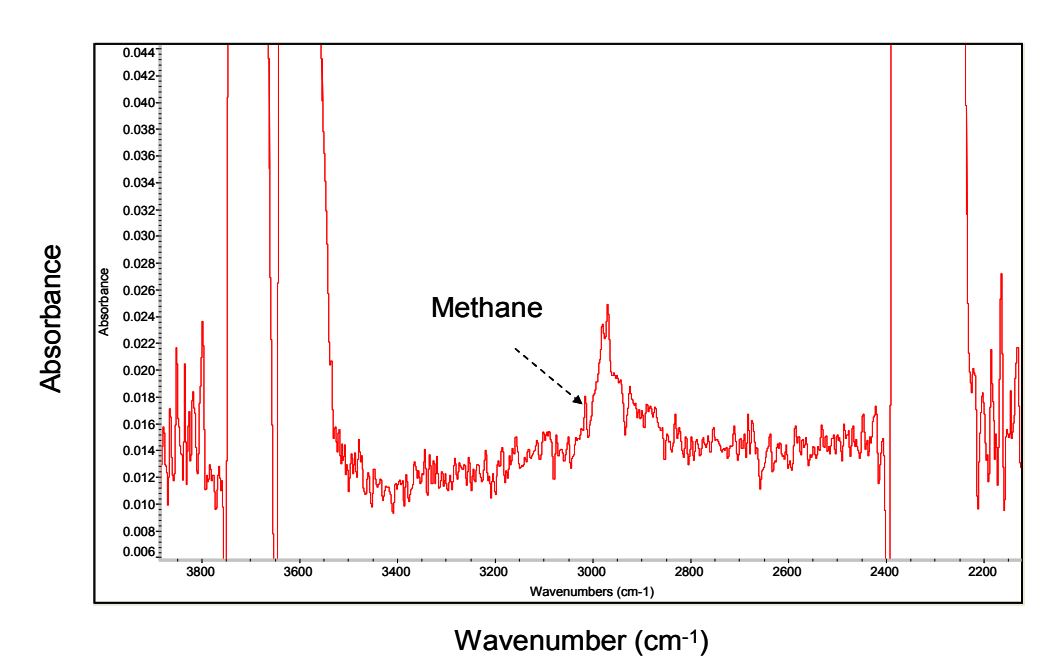


Figure 15. FTIR spectrum of gas composition in the photocaytalytic reactor with titania nanotubes attached on the coarse titanium mesh under sunlight radiation of 5.5 hours. (power density $\sim 96~\text{mW/cm}^2$)

We've also tested the photocatalytic activity of Degussa P25 titania attached to various copper-based alloys (i.e., brass, bronze). Our results demonstrated that some copper based alloys (i.e., brass) appear to be more stable alternatives for supporting titania photocatalysts for long-term methane production.

In order to further enhance the separation of photo-generated electron-hole pairs and improve visible light absorption, a PN junction structure was also formed between titania and Cu_2O , which is a narrow-bandgap semiconductor with energy gap around 2.1eV (~590nm). A PN-metal multi-junction structure was built by immobilizing Degussa P25 titania on Cu_2O film grown on copper mesh and the photocalytic activity of such structure was investigated. We utilized both a vacuum oven as well as a tube furnace to heat treat various copper substrates at about 180 $^{\circ}C$, so as to produce a very thin (<100nm) Cu_2O layer on the surface of the copper. Then, we coated Degussa P25 titania nanoparticles on the surface of the oxidized copper mesh and tested the photocatalytic activity using a quartz reactor under visible light radiation.

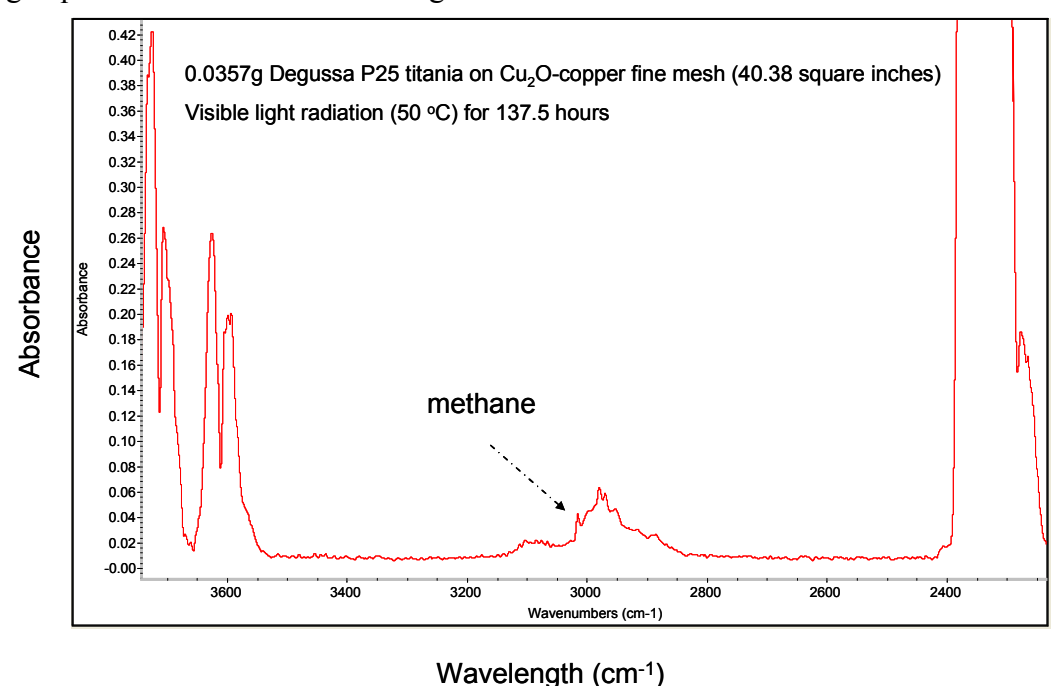


Figure 16. FTIR spectrum of gas composition in the photocaytalytic reactor with 0.0357 g Degussa P25 titania attached on oxidized copper mesh (200).

The result of the P25/Cu₂O experiments is shown in Figure 16, where an obvious methane peak can be observed after 137.5 hours of visible light radiation. This may be the first report on visible light photocatalysis for the conversion of CO₂ and water into methane using a PN junction structure formed with n-type titania on top of p-type Cu₂O system. Since visible light accounts for 43% energy of sunlight, such a breakthrough is important in developing highly efficient semiconductor-based system for CO₂ reforming into hydrocarbon under sunlight radiation. As previously mentioned, it has been well established that Cu₂O is a p-type semiconductor with a narrow band-gap (2.1eV). It has also been reported that Cu₂O is an effective photocatalyst for decomposing water into H₂ and O₂ under visible light radiation. Therefore, we explored the possibility of employing Cu₂O as a visible light photocatalyst for CO₂ conversion into hydrocarbons. Two types of copper meshes (a fine 150 mesh and a coarse 50 mesh) were employed and Cu₂O films (red color) were grown on the surface of the copper inside an oven at about 180 °C. The photocatalytic activity of the structures was then tested under visible light radiation. We

found that the oxidized fine copper mesh (150 mesh) did not present photocatalytic activity. However, as the oxidized coarse copper mesh (50 mesh) was employed as a supported photocatalyst substrate, the amount of CO₂ in the reactor decreased and a significant amount of methane was produced, suggesting a strong catalytic activity of such system in converting CO₂ and water into hydrocarbon fuels (see Figure 17). The reason for such dependence on mesh size is not yet clear. Since it is possible that both Cu₂O and CuO films are formed when copper is heated at 180 °C, the relative ratios of the two copper oxides may be an important factor in the overall photocatalytic activity of the structures. From Figure 17, it is interesting to note that, for the oxidized coarse copper mesh, there is a strong methane peak produced after 16 hours of visible light radiation. Using the FTIR calibration data, we estimated that the methane production rate for these structures reached a whopping 1823 uL/h.g-oxidized copper film, which is over 6X higher than anything ever reported from a solar-based photocatalyst.¹⁴

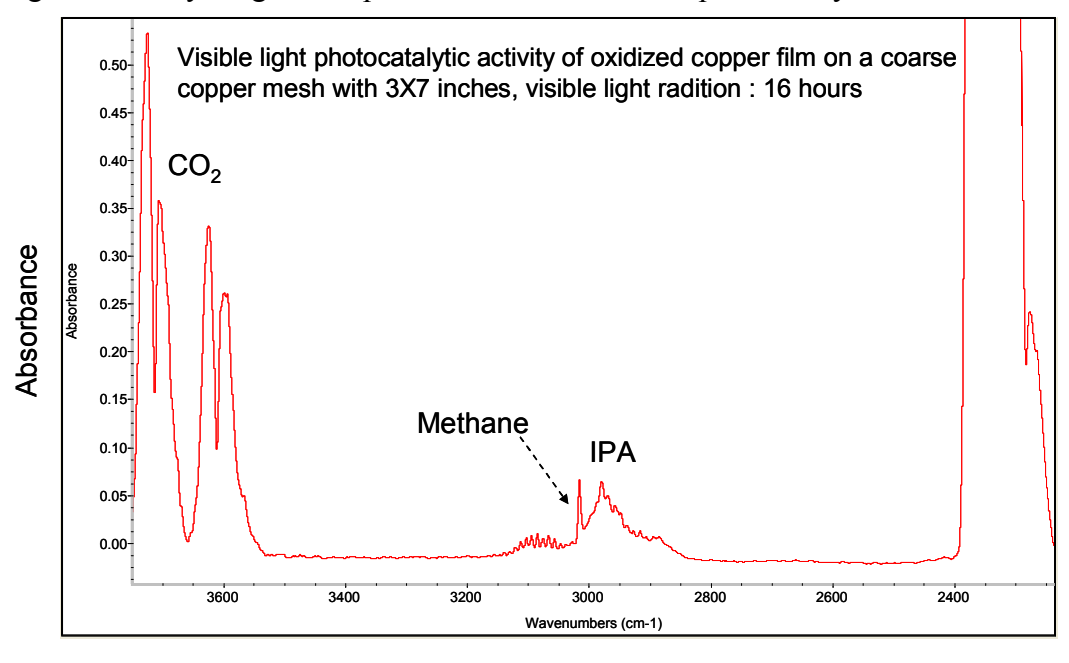


Figure 17. FTIR spectrum of gas composition in the photocaytalytic reactor with 0.0010g oxidized copper film attached on a coarse copper mesh (3×7) after 16 hours of visible light radiation at 50° C

Wavenumber (cm⁻¹)

During all experiments involving Cu2O/CuO/Cu substrates, it was again noticed that the methane yield decreased as the photocatalytic reaction progressed, with some zones on the substrate becoming dark. This is believed to be the result of the formation of a thick layer of CuO and graphitic carbon from CO₂ and oxidation reactions, which were confirmed earlier by EDS analysis.

2.3 Development of Solution-deposition Techniques

Samples of the ZnSe nanocrystals were dispersed in a solvent solution containing both toluene and chloroform. A hybrid ZnSe/TiO₂ system was then attempted by mixing different amounts of each solution and then heat drying the mixture in an oven to obtain

TiO₂ nano-powders coated with ZnSe. The optical properties of these nano-powders were then analyzed using an Ocean Optics absorption/reflectance unit and a broadband UV/Vis light source. The results are shown in Figure 18 and show clearly that the hybrid ZnSe/TiO₂ system exhibits higher absorption of visible light in the blue region of the spectrum.

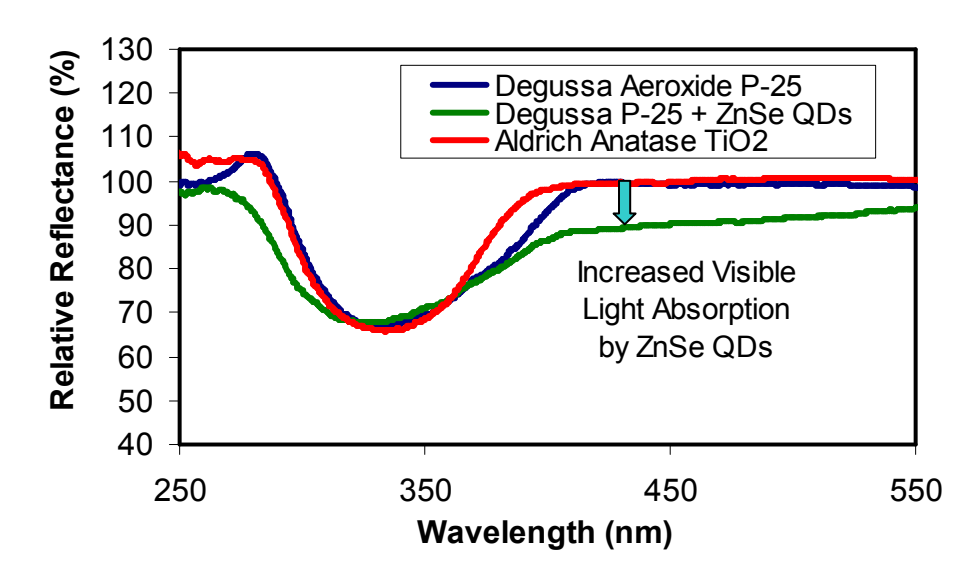


Figure 18. Reflectance spectra comparing light absorption by commercial and QD-modified TiO₂

Low-cost techniques such as dip-coating, brush painting and electrophoretic deposition (EP) were also investigated for the deposition of TiO₂ layers and nanoparticles on various substrates. Electroplating was also used to coat various types of metals (Ag, Au, Ni, etc.) on copper substrates for the purpose of evaluating their impact on the photo catalytic reaction and long-term stability and performance of the reactor.

Dip coating was also attempted on borosilicate glass substrates that were cleaned with ethanol. The clean substrates were dried at 110 °C for 24 h. After dip coating was completed, the substrates were dried at room temperature and then placed into a programmable high temperature furnace for heat treatment. The furnace temperature was incremented at a ramp rate of 5.0 °C/min until 500 °C; this temperature was held for 30 min and then cooled down naturally.

2.4 Post-deposition Heat Treatment

The TiO₂-metal structures that were produced so far were baked in either air or vacuum over a temperature range from 80-200°C for 15-30 minutes. Electroplated substrates were also dried in vacuum to remove excess water and solvents prior to coating with the photocatalyst. The coated borosilicate glass substrates were annealed at 500°C, as previously described. Higher temperature treatment (in inert atmosphere or vacuum) will be attempted in future experiments to "fuse" the p-n junctions and improve its crystalline structure as well as achieve higher adhesion properties of catalyst particles to the substrate material.

2.5 Evaluation of Thin-film Quality

The CO₂ photocatalytic and reforming activity of the various photocatalyst structures was evaluated using Fourier Transform Infrared Spectroscopy (FTIR) using calibrated 10 cm gas cells containing known volume of CO₂ (from an Airgas cylinder) along with photocatalyst structures on various substrate materials. Using known and published FTIR signature spectra for



CO₂ and various hydrocarbons (Figure 19), this technique provides quick feedback on CO₂ degradation as well as hydrocarbon evolution as a function of time and incident light. This data is being used to optimize the various properties of the photocatalyst structure and substrate material and determine the ideal parameters for maximizing CO₂ reforming activity.

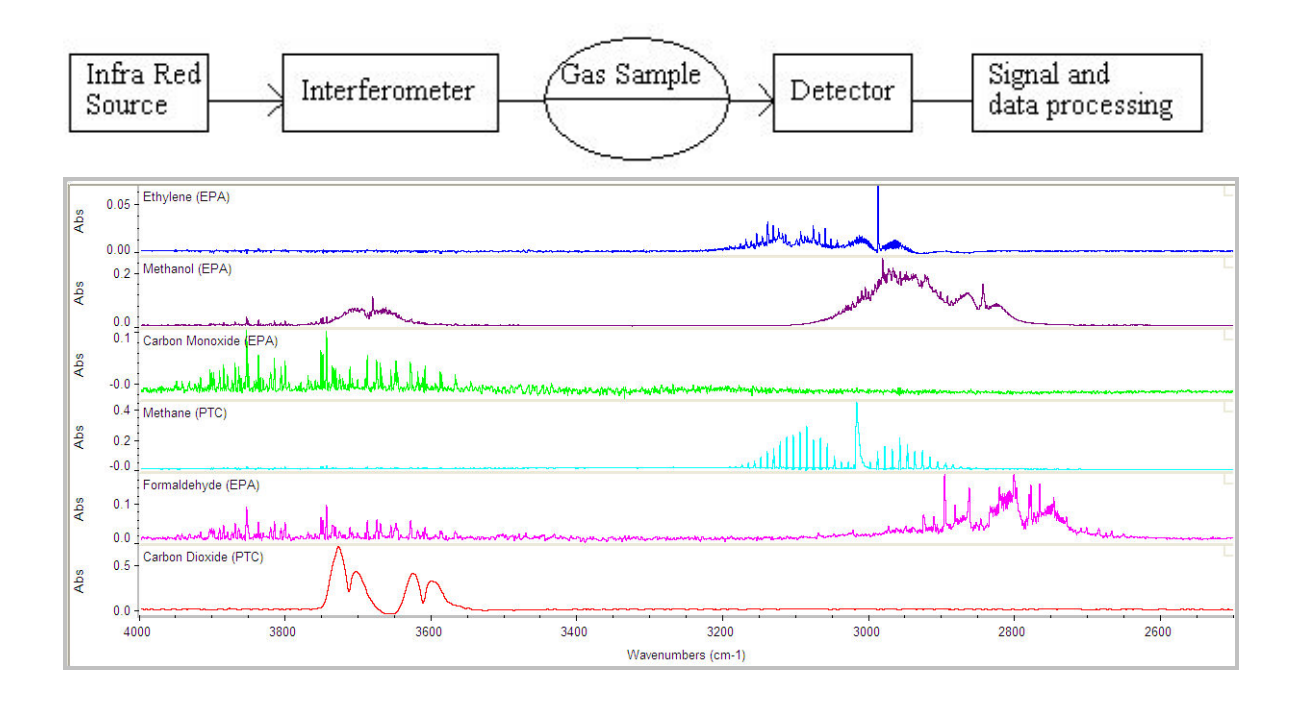


Figure 19. Top: FTIR system and gas analysis process at PTC. Bottom: FTIR absorption spectra of CO₂ and various hydrocarbons.

Task 3.0 Development & Fabrication of PN Structure for CO₂ reduction

3.1 Simulation and Optimization of p-n Structures

In this project, efforts were initiated to develop models to evaluate various charge separating semiconductor junctions. These junctions, such as p-n junctions and Schottky Barrier junctions were proposed to separate electron-hole pairs generated optically. This

separation decreases the likelihood of recombination and also reversal of desired reforming reactions. In addition, the use of such a structure, particularly the heterostructure p-n junction, enables a greater utilization of the sunlight spectrum rather than relying solely on the UV portion of the spectrum.

To evaluate these properties, a one-dimensional semiconductor device simulation software package, PC-1D, was used to model these junctions. It should be pointed out that as these structures may employ less common materials, some electrical parameters might have to be estimated or extrapolated from similar materials.

Values of electron affinity and work functions were tabulated (Table 3) for some of these materials to estimate band offset and barrier heights. However, there exists a great range of reported work functions due to the sensitivity of such a quantity to the state of the material surface. Figure 20 below shows modeled band structures for three devices: two p-n heterojunction devices and one barrier device. The two p-n junctions on the left are comprised of an n-type TiO₂ and p-type materials with nominal bandgaps of 1.5 and 2.3eV, corresponding to values obtainable with ZCS quantum dots. The barrier device on the other hand, was simulated using a Cu coating of TiO₂.

As discussed above, we would lie to take advantage of a broader range of the light frequencies than are available to simple TiO_2 photocatalysts. Figure 21 shows a simulation of the quantum efficiency of these devices in Figure 20 base upon exposure to an AM1.5 level of light. As is seen, junctions with the smaller bandgap provides much broader range of absorption leading to greater efficiency. This can also be seen in Figure 22, a representation of the I-V under illumination. Again, the smaller bandgap material $(E_g=1.5)$ provides the larger current for the same excitation levels.

Table 3. Work functions for various materials.

Element	eV	Element	еV	Element	еV	Element	еV	Element	еV
Ag:	4.52-4.74	<u>Al:</u>	4.06-4.26	As:	3.75	<u>Au:</u>	5.1-5.47	<u>B:</u>	~4.45
<u>Ba:</u>	2.52-2.7	<u>Be:</u>	4.98	<u>Bi:</u>	4.34	<u>C :</u>	~5	<u>C a:</u>	2.87
<u>C d:</u>	4.08	<u>C e:</u>	2.9	<u>C o:</u>	5	<u>C r:</u>	4.5	<u>Cs:</u>	2.14
<u>C u:</u>	4.53-5.10	<u>E u:</u>	2.5	<u>Fe:</u>	4.67-4.81	<u>Ga:</u>	4.32	<u>Gd:</u>	2.9
Hf:	3.9	Hg:	4.475	<u>ln:</u>	4.09	<u>lr:</u>	5.00-5.67	<u>K:</u>	2.29
<u>La:</u>	4	<u>Li:</u>	2.93	<u>Lu:</u>	~3.3	Mg:	3.66	Mn:	4.1
Mo:	4.36-4.95	<u>Na:</u>	2.36	<u>Nb:</u>	3.95-4.87	<u>Nd:</u>	3.2	<u>Ni:</u>	5.04-5.35
<u>Os:</u>	5.93	<u>P b:</u>	4.25	<u>P d:</u>	5.22-5.6	<u>P t:</u>	5.12-5.93	<u>R b:</u>	2.261
<u>R e:</u>	4.72	<u>R h:</u>	4.98	<u>R u:</u>	4.71	<u>S b:</u>	4.55-4.7	<u>S c:</u>	3.5
<u>S e:</u>	5.9	<u>S i:</u>	4.60-4.85	<u>S m :</u>	2.7	<u>S n:</u>	4.42	<u>S r:</u>	~2.59
<u>Ta:</u>	4.00-4.80	<u>Tb:</u>	3	<u>Te:</u>	4.95	<u>Th:</u>	3.4	<u>T i:</u>	4.33
<u>T1:</u>	~3.84	<u>U:</u>	3.63-3.90	<u>V:</u>	4.3	<u>W:</u>	4.32-5.22	<u>Y:</u>	3.1
<u>Y b:</u>	2.60 [2]	Zn:	3.63-4.9	Zr:	4.05				

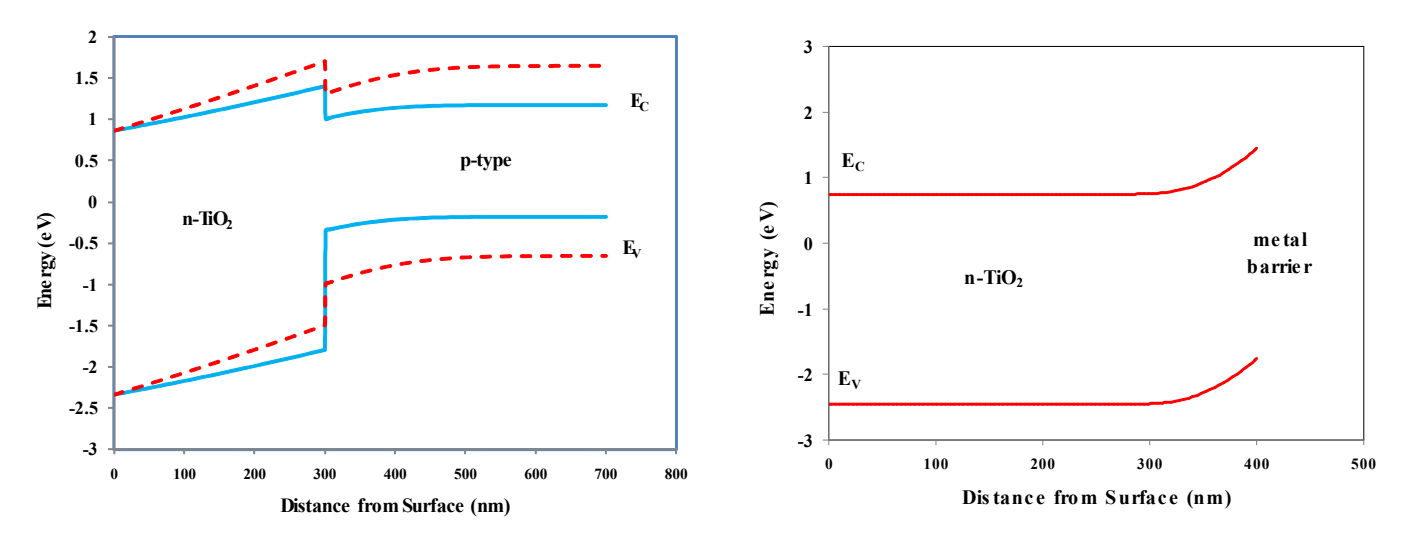


Figure 20. Simulated band structure for (left): two p-n heterojunctions and (right): a Schottky barrier devices. (see text for details)

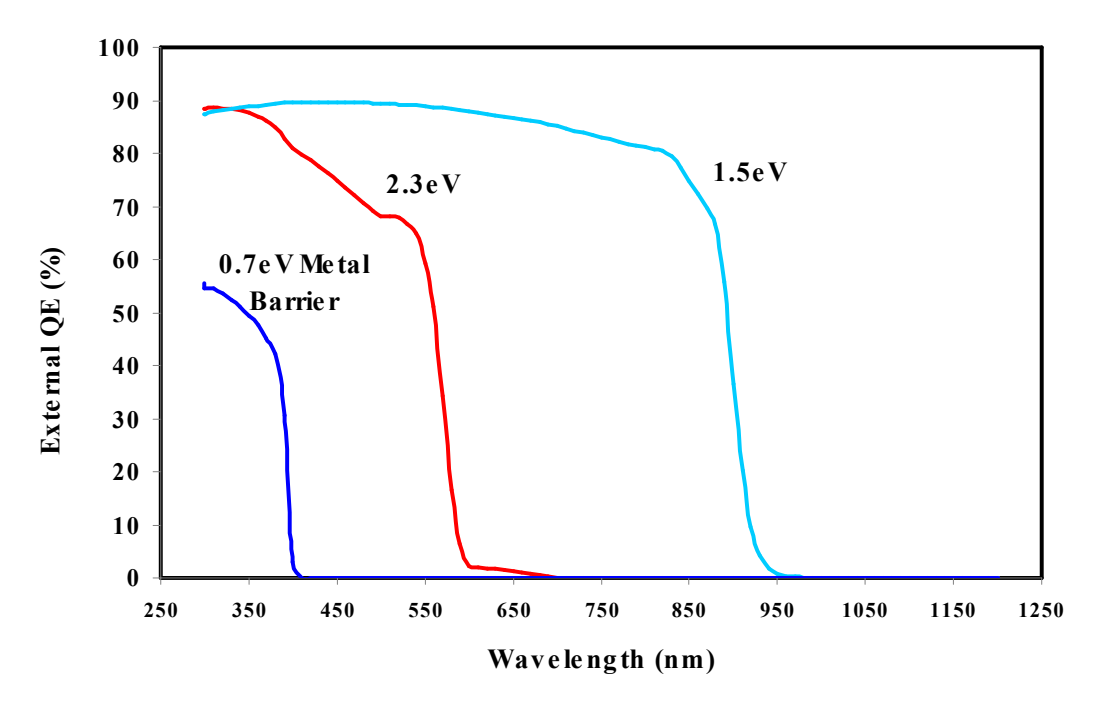


Figure 21. Simulated quantum efficiency of the structures depicted in Figure 20 indicating that the smaller bandgap material increases the use of the solar spectrum.

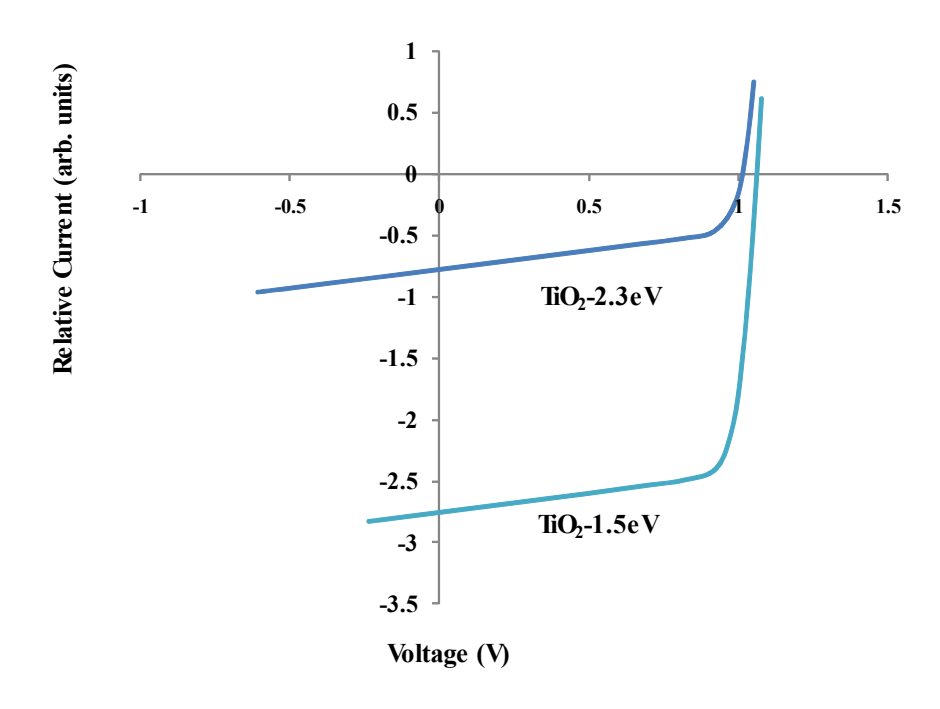


Figure 22. Simluated I-V curves for devices under AM1.5 excitation

In addition, energy band gap models were developed to help explain the observed experimental differences in photocatalytic and CO_2 reforming behavior of various semiconductor structures deposited on copper substrates. These heterostructures consisted of the conventional Cu/TiO_2 structure (Figure 23), a stacked structure of $Cu/ZnO/TiO_2$ (Figure 24), and a $Cu/CeO_2/TiO_2$ structure (Figure 25).

In the conventional Cu/TiO_2 structure (Figure 23), UVA light energy exceeding TiO_2 anatese bandgap (>3.2 eV or <390nm) is absorbed generating electron-hole pairs, which can then diffuse to either side of the junction under zero potential. Therefore, both oxidation and reduction reactions can take place on either side of TiO_2 with more electrons trapped at the Cu side. Since holes are also capable of diffusing towards the Cu side, there is a high probability of H_2O oxidation resulting in H^+ ions, which then can react with reduced CO_2 to form CH_4 , as shown by the FTIR spectrum in Figure 34 (middle).

In the case of Cu/ZnO/TiO₂ structure (Figure 24), UVA light energy exceeding both TiO₂ anatese bandgap (>3.2 eV or <390nm) and ZnO bandgap (>3.37 or <368nm) is absorbed generating electron-hole pairs. However, most of the high energy photons will be absorbed first by the TiO₂ layer and, depending on the thickness, only limited energy remains for electron-hole generation in ZnO. Furthermore, because of the band alignment between ZnO/TiO₂ (Figure 24), ZnO acts as a hole blocker resulting in increased water oxidation (high H⁺) at the TiO₂ surface and reduced oxidation at the Cu/ZnO side. The result is a reduction of CH₄ formation but an increase in CO₂ hydrogenation with the production of formic acid or CH₂O₂, as illustrated in Figure 34 (middle).

In the case of Cu/CeO₂/TiO₂ structure (Figure 24), UVA light energy can only be

absorbed in TiO₂ due to the large CeO₂ bandgap (5.5 eV or 225nm) and, therefore, electron-hole pairs can only be generated within TiO₂. Again, due to the band alignment between CeO₂/TiO₂ (Figure 24), CeO₂ acts as a hole blocker resulting in increased water oxidation (high H⁺) at the TiO₂ surface and negligible oxidation at the Cu/CeO₂ side. The result is primarily the production of formic acid or CH₂O₂, as illustrated in Figure 34 (top).

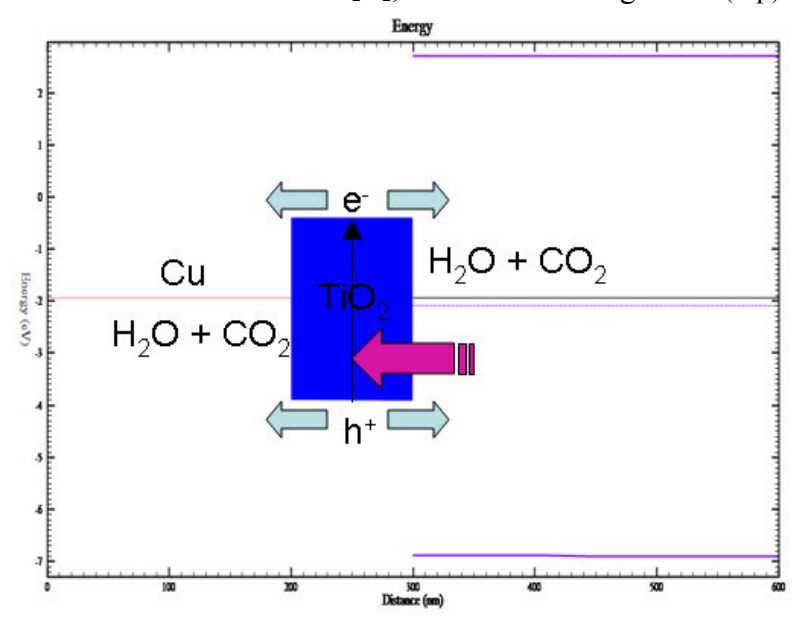


Figure 23. Simulated band diagram (zero potential) for a Cu/TiO2 photocatalytic structure illustrating electron-hole generation in TiO2 and ability to diffuse to either side of TiO2 layer

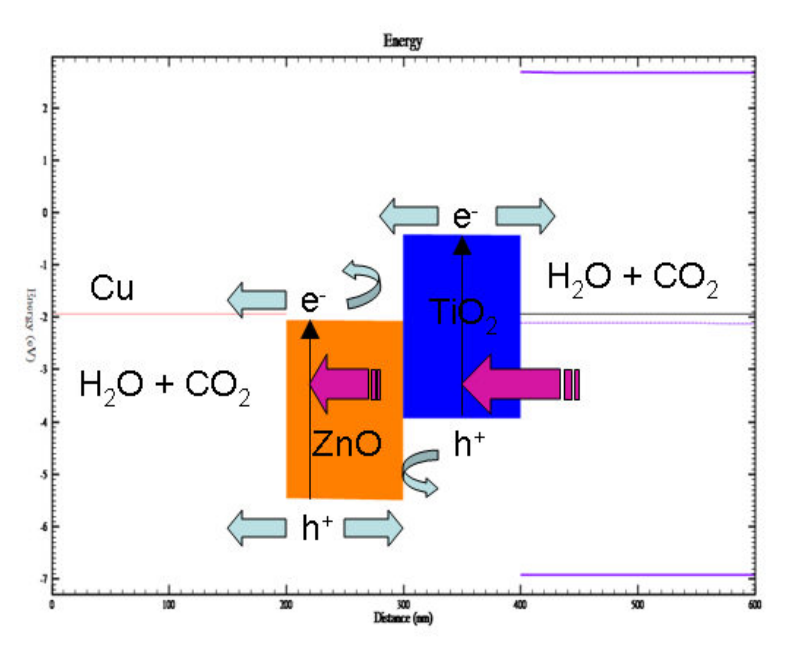


Figure 24. Simulated band diagram (zero potential) for a $Cu/ZnO/TiO_2$ photocatalytic structure illustrating electron-hole generation in both TiO_2 and ZnO and ZnO's ability to block holes (but not electrons) generated in TiO_2 layer

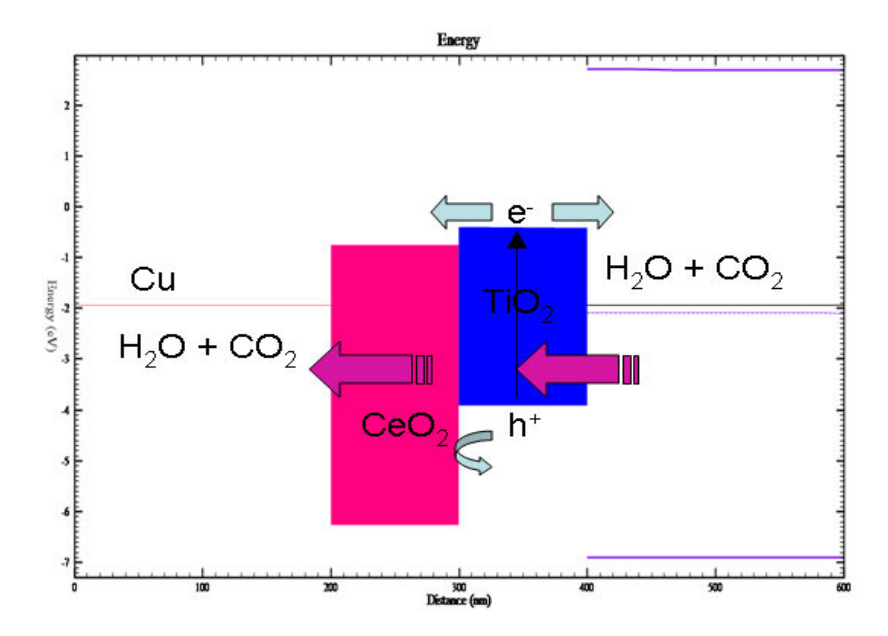


Figure 25. Simulated band diagram (zero potential) for a Cu/CeO₂/TiO₂ photocatalytic structure illustrating electron-hole generation in TiO₂ and CeO₂'s ability to block holes (but not electrons) generated in TiO₂ layer

We continued energy band gap modeling in order to help explain the observed experimental differences in photocatalytic and CO₂ reforming behavior of various semiconductor structures deposited on copper substrates. The heterostructures investigated also consisted of a Cu₂O/TiO₂ structure, a stacked structure of ZnO/TiO₂, and an evaluation of the potential quantum efficiency of CuO and Cu₂O material systems.

These simulations were performed using PC-1D and they confirmed those obtained in our study. In the case of n-ZnO/n-TiO₂ structure (Figure 26), the absorption is limited to the UVA range (<390nm) since only the energy exceeding TiO₂ bandgap (>3.2 eV) and ZnO bandgap (>3.37) will be absorbed by the structure. However, due to the band offset between ZnO/TiO₂ (Figure 26), ZnO acts as a hole blocker but only of those holes generated within the TiO₂. Since the bandgap of ZnO is close to that of TiO₂, some of the UVA light having energy higher than 3.37eVwill also be absorbed by the ZnO. Therefore, some holes can still diffuse into the Cu substrate and result in metal oxidation.

In the case of $\text{Cu}_2\text{O/TiO}_2$ structure (Figure 27), UVA light energy will be absorbed in TiO_2 while a significant amount of visible light (up to around 600nm) will be absorbed in the narrow-bandgap Cu_2O semiconductor. Therefore, when exposed to solar radiation, electron-hole pairs can be generated within both the TiO_2 (<390nm) and the Cu_2O (<600 nm) layers. The calculated quantum efficiency (QE) of such a structure compared to the more conventional Cu/TiO_2 and Cu/ZnO/TiO_2 systems is shown in Figure 28. In addition, if copper oxide (CuO) can be effectively utilized within a photocatalyst structure, the absorption of such system can be extended significantly further into the near-IR since the bandgap of CuO can vary from 1.21-1.51 eV, which corresponds to the range of wavelengths from 821-1025nm.

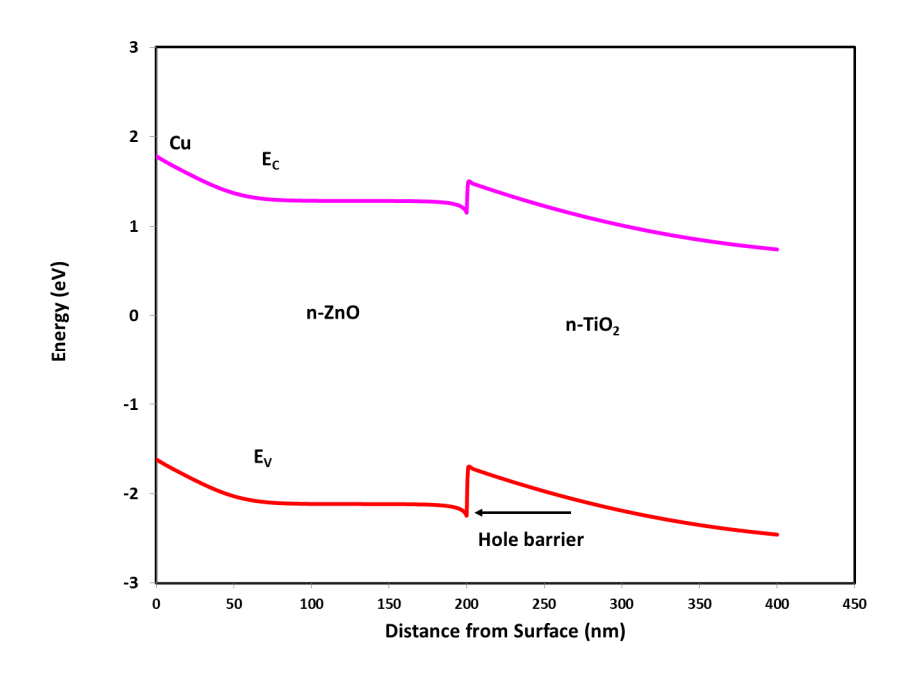


Figure 26. Simulated band diagram of a n-type ZnO and n-type TiO_2 photocatalytic structure illustrating interface hole barrier of the two oxide semiconductors with comparable bandgap.

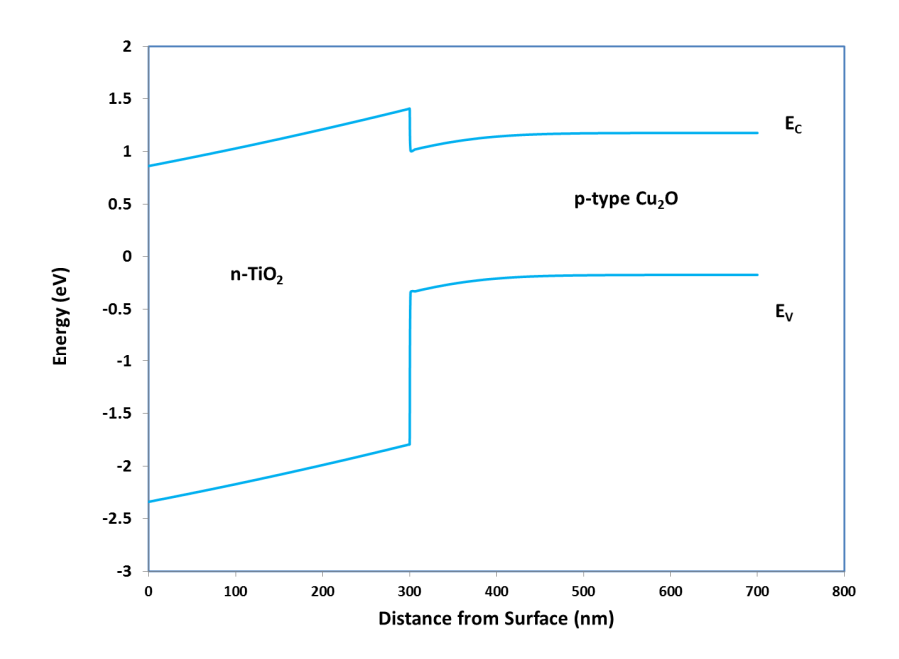


Figure 27. Simulated band diagram for a Cu₂O/TiO₂ photocatalytic structure illustrating relative energy bandgaps of the two photocatalyst semiconductors

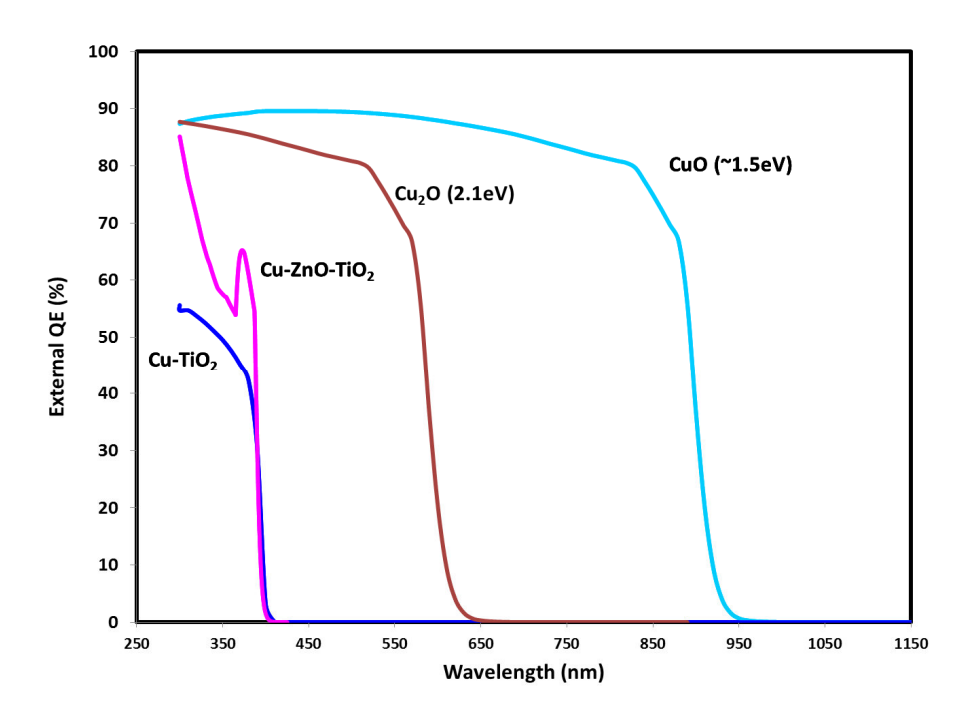


Figure 28. Simulated external quantum efficiency charts for various structures illustrating expected performance throughout various parts of the spectrum.

In addition, the investigations were also performed on the promising Cu₂O/CuO/Cu photo-catalytic structure, and an evaluation of its bandgap alignment parameters and quantum efficiency as a function of wavelength. These simulations were performed using 200nm of cuprous oxide deposited on copper followed by 200nm of cupric oxide, as shown in Figure 31. Both these materials have energy bandgaps small enough to allow the absorption of visible light from the solar spectrum, as had been discussed in the report and is evident by the quantum efficiency calculations presented in Figure 32. However, while the conduction band offset between Cu₂O/CuO will result in blocking some photogenerated electrons in the CuO layer, most of the electrons generated within the layer will be carried by the built-in electric field into the Cu substrate where they can help with the reduction of CO₂. In addition, the only valence band holes that could cause oxidation of copper under light exposure are the ones photo-generated within few tens of nanometers from the Cu₂O/Cu interface.

In terms of quantum efficiency, the Cu₂O/CuO structure is very effective at absorbing visible and near-infrared sunlight, as shown in Figure 32, where the range of wavelengths possible is from 400-1100nm.

After we have completed our first Year 2 milestone regarding the development and optimization of the computer modeling for the PN structure, we continued to perform the investigations on the promising CeO₂/CuO/TiO₂/Cu photo-catalytic structure, and an evaluation of its bandgap alignment parameters. These simulations were performed using 100nm of CuO, 50nm of CeO₂, and 100 nm of TiO₂. As was previously reported for the conventional CuO/TiO₂ structure, UVA and visible light energies exceeding CuO (>1.5 eV) or TiO₂ anatese bandgap (>3.2 eV) is absorbed generating electron-hole pairs, which

can then diffuse to either side of the junction under zero potential. Therefore, both oxidation and reduction reactions can take place on either side of with more electrons trapped at the Cu side. Since holes are also capable of diffusing towards the Cu side, there is a high probability of Cu oxidation resulting in the formation of CuO and Cu₂O which act as additional barriers for electron flow towards the copper metal. Therefore, in order to prevent further oxidation of the copper a large bandgap material such as CeO₂ is needed to act as a barrier for holes but not for electrons. There are two possible placement configurations for the CeO₂ layer, as illustrated by the bandgap simulations shown in Figure 29 and Figure 30.

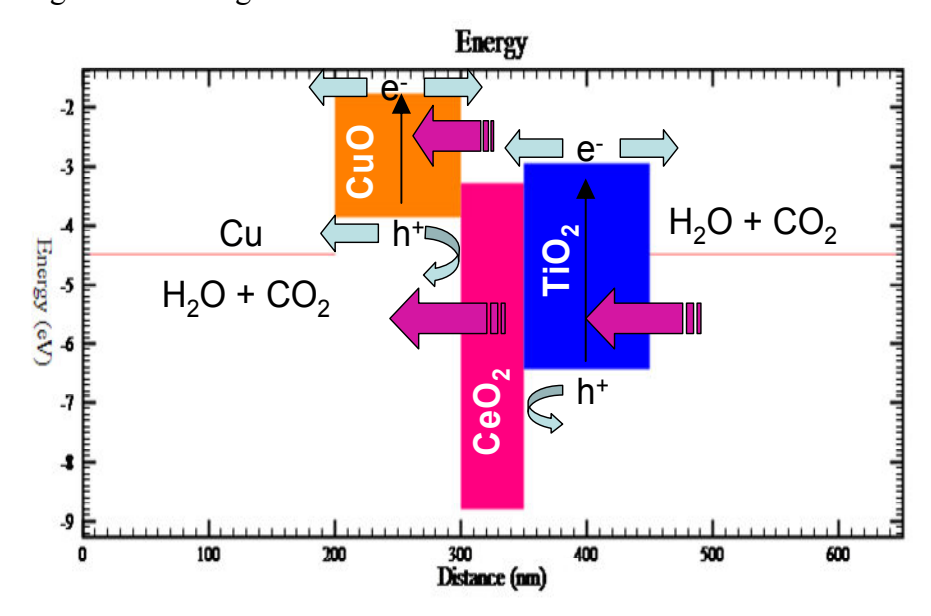


Figure 29. Simulated band diagram for a CuO/CeO₂/TiO₂ photocatalytic structure illustrating relative conduction and valence energy band alignment of the different semiconductors on a Cu substrate

In the case where the CeO₂ layer is placed between CuO and TiO₂ (Figure 29), the large CeO₂ bandgap act to block any holes (but not electrons) generated within the TiO₂ layer from reaching the Cu substrate. However, holes generated within the CuO layer under visible light will still reach and oxidize the copper substrate. Therefore, the optimal placement of the CeO₂ layer is between the Cu substrate and the CuO layer, as illustrated by Figure 30. In such a case, the CeO₂ layer helps to block holes generated in both CuO and TiO₂ for the most protection of the Cu substrate against light-induced oxidation.

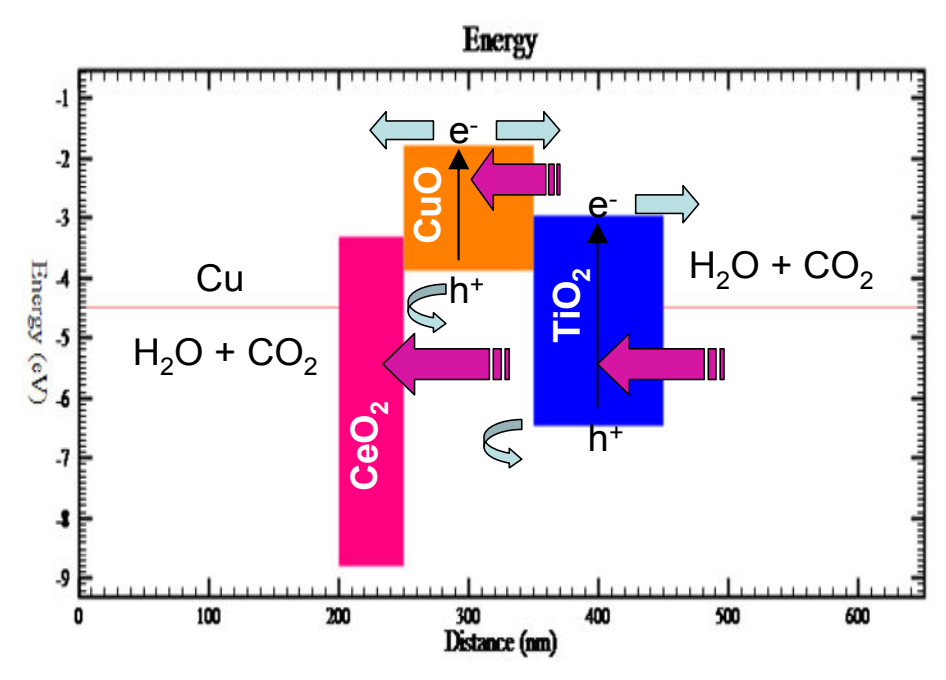


Figure 30. Simulated band diagram for a CeO₂/CuO/TiO₂ photocatalytic structure illustrating relative conduction and valence energy band alignment of the different semiconductors on a Cu substrate

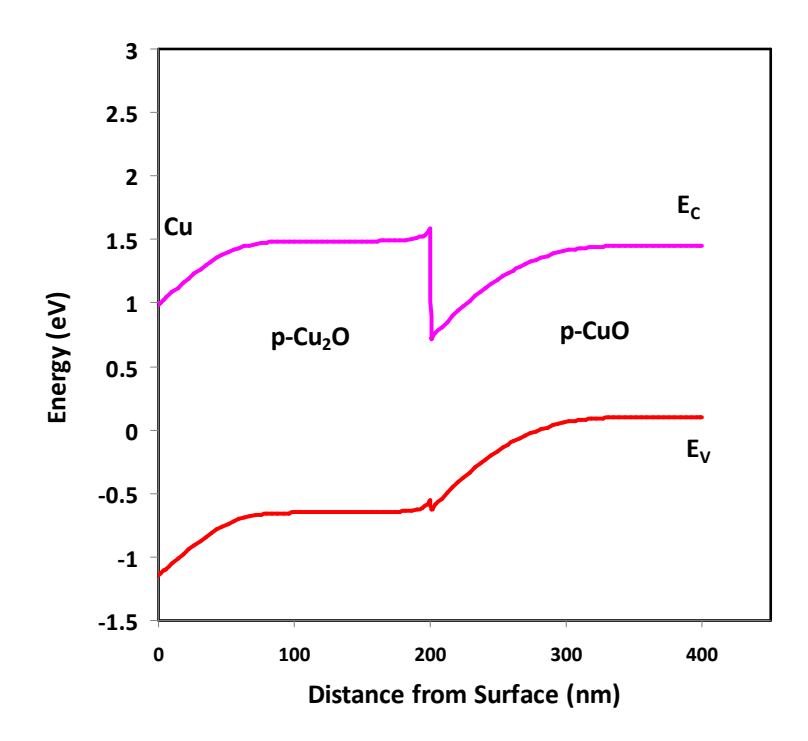


Figure 31. Simulated band diagram for a Cu₂O/CuO/Cu photocatalytic structure illustrating relative conduction and valence energy bandgaps of the two semiconductors on a Cu substrate

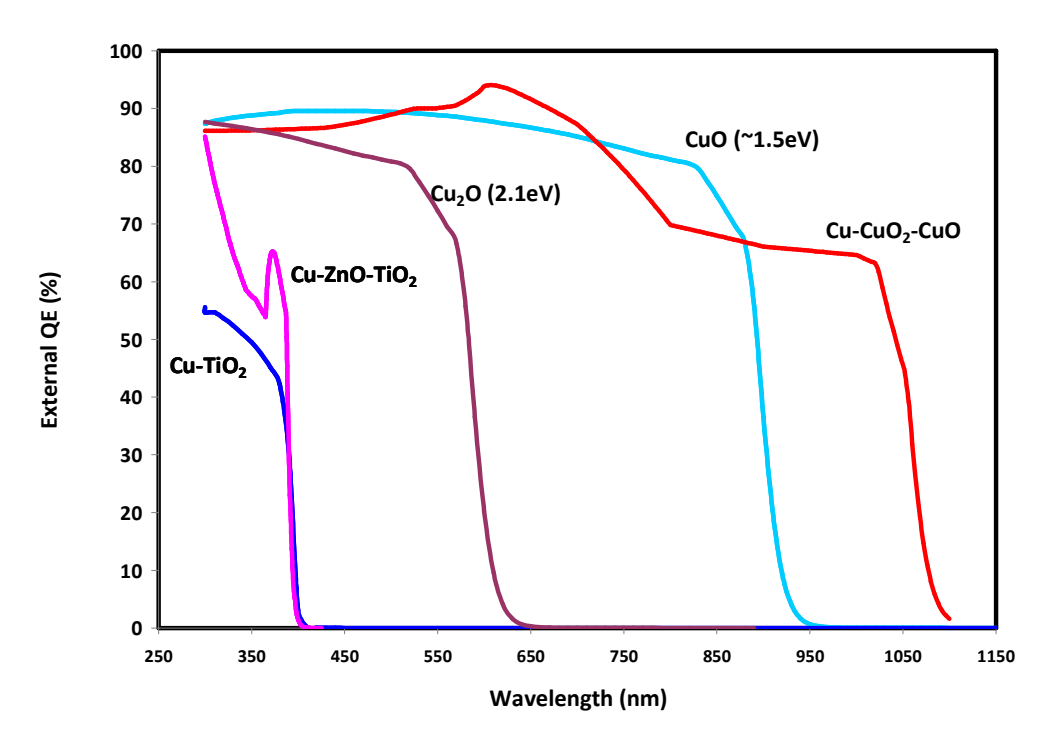


Figure 32. Simulated external quantum efficiency charts for various structures and extended to a multilayer junction formed with Cu-Cu₂O-CuO throughout Q4.

3.2 Comparison of p-n Structure with Conventional Photocatalysts

The performance of the various fabricated structures was compared using conventional P25 nano-TiO₂ photocatalysts, while being illuminated by a 6W fluorescent blacklight placed external to glass mini reactors similar to the one shown in Figure 33.

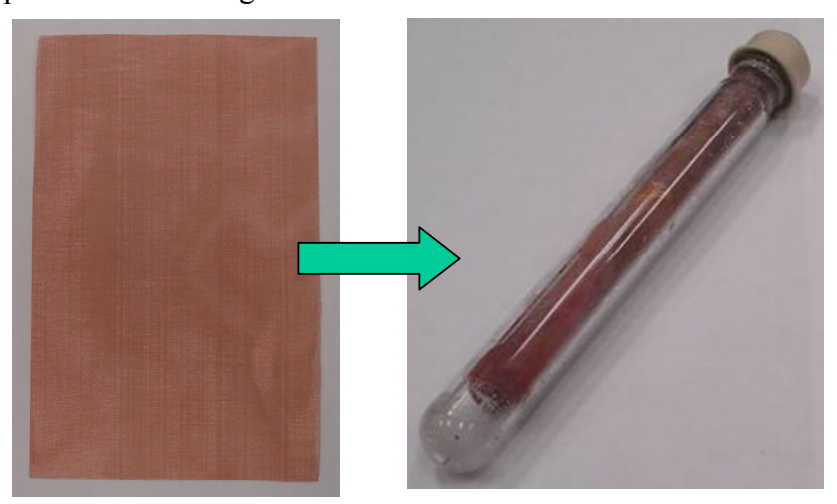


Figure 33. Small (8 inch) glass reactor used for evaluating CO₂ reforming potential of various photocatalyst structures and substrate materials

The effectiveness and selectivity of each structure for CO₂ reforming were measured against FTIR signatures of known (references) gases and vapors, as shown in Figure 34.

The below FTIR data demonstrates that, by choosing a specific structure, we are able to exercise some degree of control over the hydrocarbon product selectivity resulting from CO_2 photocatalytic reforming activity. In the particular examples shown in Figure 34, the reforming activities from several metal-semiconductor structures composed of 1) TiO_2/Cu , 2) $TiO_2/CeO_2/Cu$, and 3) $TiO_2/ZnO/Cu$ are compared. In the case of the simple TiO_2/Cu structure, only methane was detected as a result of reforming CO_2 and H_2O by light. However, when a H_2O layer is introduced between H_2O and H_2O by the H_2O interpretable H_2O . Formic acid, also known as methanoic acid, is an important intermediate in a variety of chemical synthesis processes and is also used as a fuel in some proton exchange membrane fuel cells (PEMFC). Furthermore, when a H_2O layer is introduced between H_2O and H_2O and H_2O layer is introduced between H_2O and H_2O and H_2O layer is introduced between H_2O and H_2O and H_2O layer is introduced between H_2O and H_2O and H_2O layer is introduced between H_2O and H_2O and H_2O layer is introduced between H_2O and H_2O and H_2O by the H_2O layer is introduced between H_2O and H_2O and H_2O by the H_2O layer is introduced between H_2O and H_2O and H_2O by the H_2O layer is introduced between H_2O and H_2O by the H_2O layer is introduced between H_2O and H_2O by the H_2O layer is introduced between H_2O and H_2O layer is introduced between H_2O and H_2O by the H_2O layer is introduced between H_2O and H_2O by the H_2O layer is introduced between H_2O la

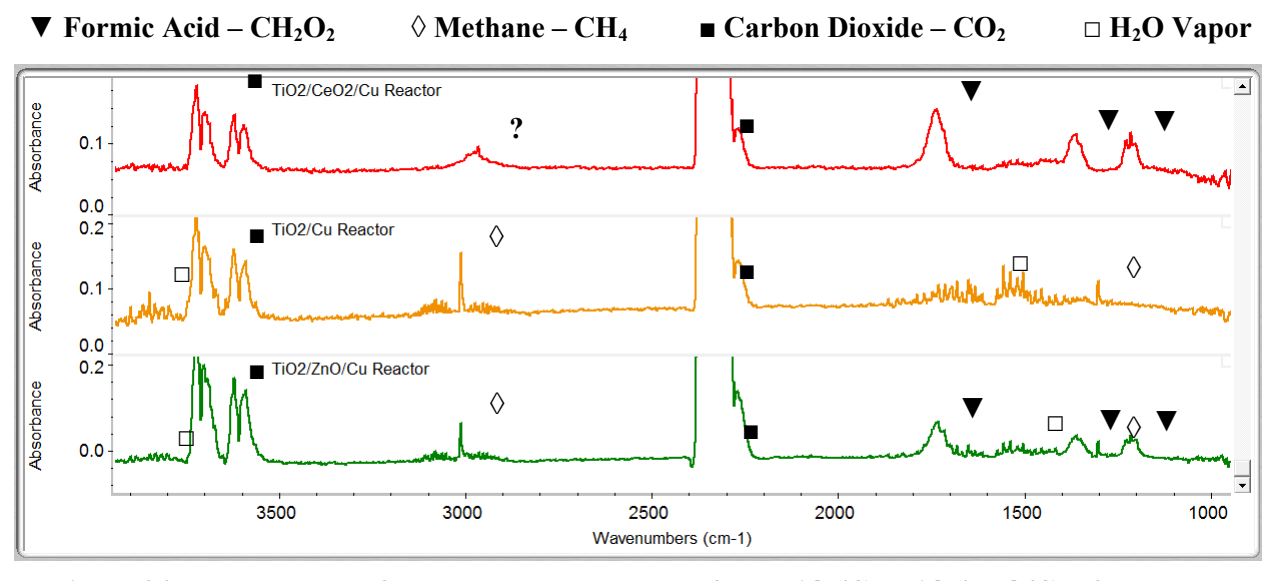


Figure 34. FTIR spectra of detectable hydrocarbons from TiO_2/Cu , $TiO_2/ZnO/Cu$, & $TiO_2/CeO_2/Cu$ structures illustrating ability to selectively enhance the production of CH_4 or CH_2O_2 (formic acid)

In addition, the Cu₂O/CuO pn structures were evaluated using a thin-film measurement system by Filmetrics, which measures film reflectance and use such data to estimate film thickness and refractive indices. Figure 35 illustrates the reflectance data obtained from such a pn heterojunction on Cu foil before (left) and after (right) heat treatment in air at 180°C. The data in Figure 35(left) demonstrate that the original untreated Cu foil had extremely thin natural oxide layers consisting of about 2 nm of CuO and 7nm of Cu₂O. Following 20 minutes of heat treatment at 180°C in air, the Cu₂O layer has grown to about 45nm, while the CuO layer changed very little to about 3nm (right). This confirms the presence of a thin-film PN junction between CuO (n-type) and Cu₂O (p-type) materials, with more dominant presence of Cu₂O at the outer surface. This

contributes to enhanced visible light absorption by Cu_2O , as illustrated by the reflectance data below since the bandgap of Cu_2O is around 2.1 eV, which corresponds to 590 nm. On the other hand, the enhanced absorption in the near-IR region seen in the reflectance data below is attributed to CuO, which has a bandgap that varies between 1.21-1.51 eV (821-1025nm). Therefore, this is one of the few ideal systems for solar energy harvesting since it is capable of absorbing a significant portion of the visible and near-IR energy from the sun, while exhibiting high photo catalytic activity.

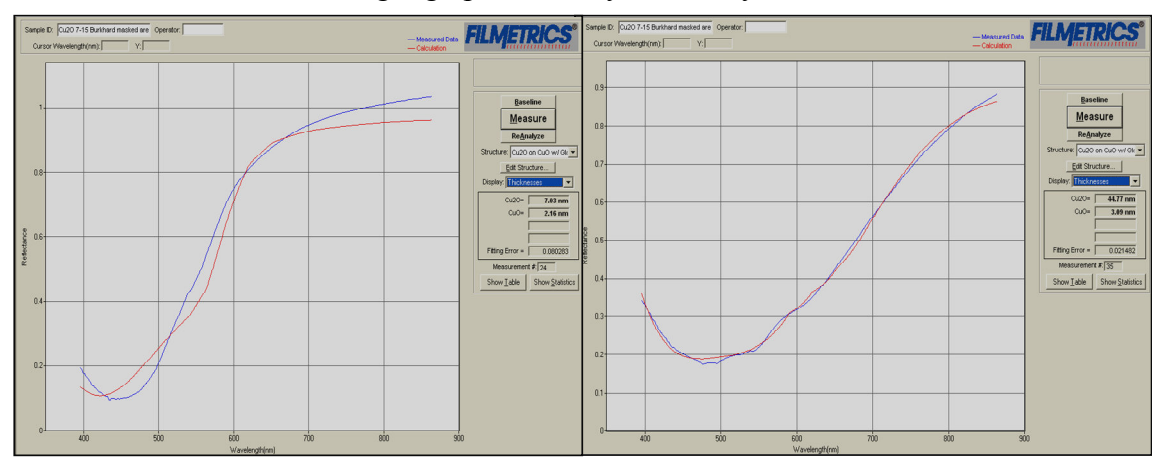


Figure 35. Measured (blue line) and calculated (red line) reflectance data for Cu₂O/CuO heterojunction before (left) and after (right) heat treatment in air at around 180°C

Moreover, three different types of p-n semiconductor/metal structures were fabricated and evaluated for their photocatalytic activity and CO₂ reforming behavior under light radiation. These consisted of 1) P25 TiO₂ on stainless steel substrate; 2) WO₃ on stainless steel substrate; and 3) WO₃ on copper substrate.

Due to its narrow semiconductor band gap of 2.7 eV, it was not surprising that the WO₃ system showed reforming activity under visible light since it is capable of absorbing into the blue spectral region up to around 460nm. However, the results for P25 TiO₂ on stainless steel substrates under visible light were somewhat unexpected since TiO₂ only absorbs in the UV part of the spectrum. Our previous work had confirmed that, under either UV or solar light radiation, the Degussa P25 titania-stainless steel system exhibited very good photocatalytic activity in converting CO₂ and water into methane and/or formic acid. In order to determine whether or not such system can better utilize solar energy, we investigated in more details its visible-light driven photocatalytic activity during the past quarter. We discovered that when Degussa P25 titania powders were immobilized on a used (oxidized) stainless steel mesh, it showed an enhanced visible-light driven photocatalytic activity in converting CO₂ and water into formic acid, as illustrated in Figure 36.

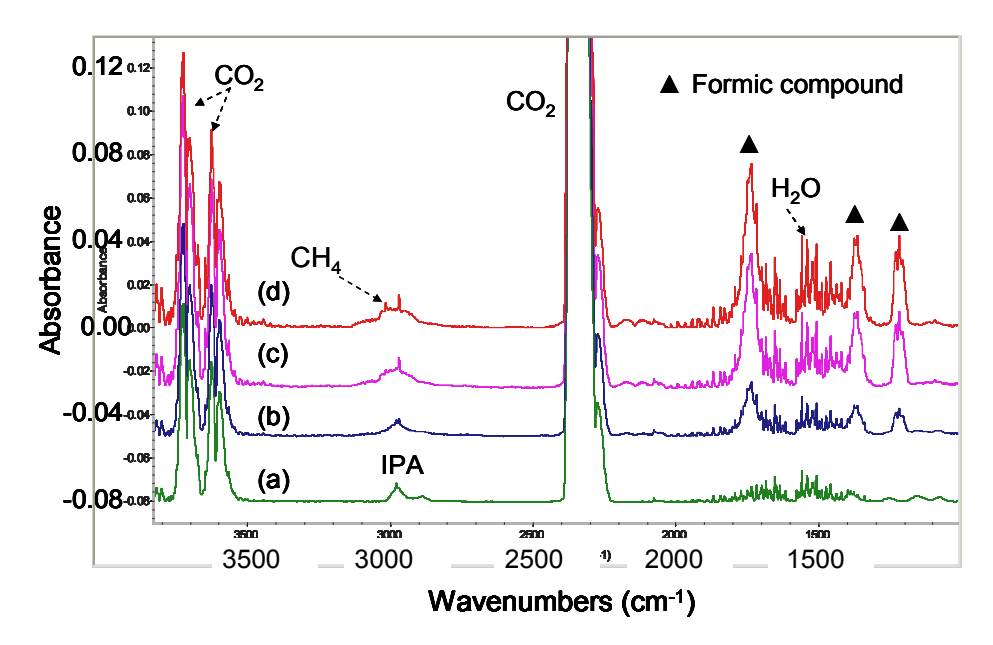


Figure 36. FTIR spectra of gas phase composition in the photocatalytic reactor with 0.183 g Degussa P25 titania powders immobilized on a used stainless steel (3×7 inches) under visible light radiation. (a) initial, (b) 17.5hours, (c) 25.5 hours, and (d) 72 hours.

In order to better understand the reasons why the oxidized stainless steel mesh showed higher visible-light activity when used with the large bandgap P25, we performed EDS/SEM analysis of the mesh to verify its composition, as shown in Figure 37. The EDS X-ray analysis found that this particular stainless steel substrate is an alloy that contains not only Fe, but also relatively high amounts of Ni and Cr elements.

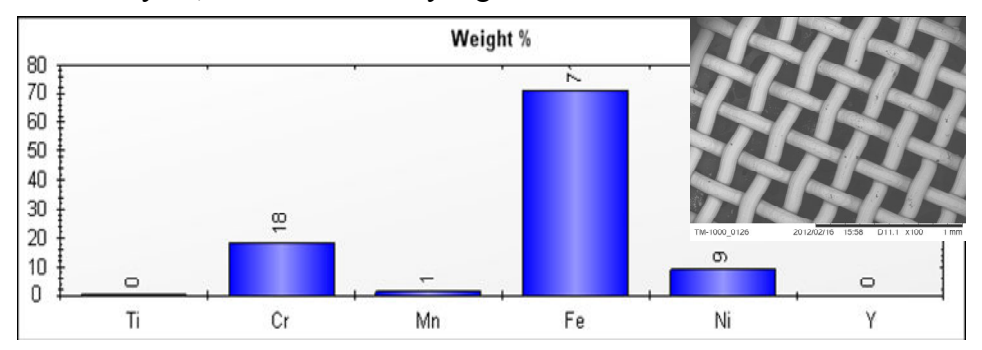


Figure 37. EDS/SEM analysis of stainless steel mesh.

Further research indicated the substrates being used are made from type 316 stainless steel alloy with detailed chemical composition shown in Table 4. The Ni and Cr levels from the datasheet agree very well with those determined using our EDS measurements and that helps explain the visible light catalytic activity. Considering the fact that the green-colored nickel oxide (NiO_x) is a p-type semiconductor known to present photocatalytic activity under visible light radiation and that iron oxide (α -Fe₂O₃) has a suitable band gap of 2-2.2eV that enables 40% sunlight absorption, these two factors could explain the high visible light activity of the oxidized steel 316 alloy, as shown below.

Table 4. Chemical composition of type 316 stainless steel alloy, as per datasheet

COMPOSITION

	Type 316 %
Carbon	0.08 max.
Manganese	2.00 max.
Phosphorus	0.045 max.
Sulfur	0.030 max.
Silicon	0.75 max.
Chromium	16.00 - 18.00
Nickel	10.00 - 14.00
Molybdenum	2.00 - 3.00
Nitrogen	0.10 max.
Iron	Balance

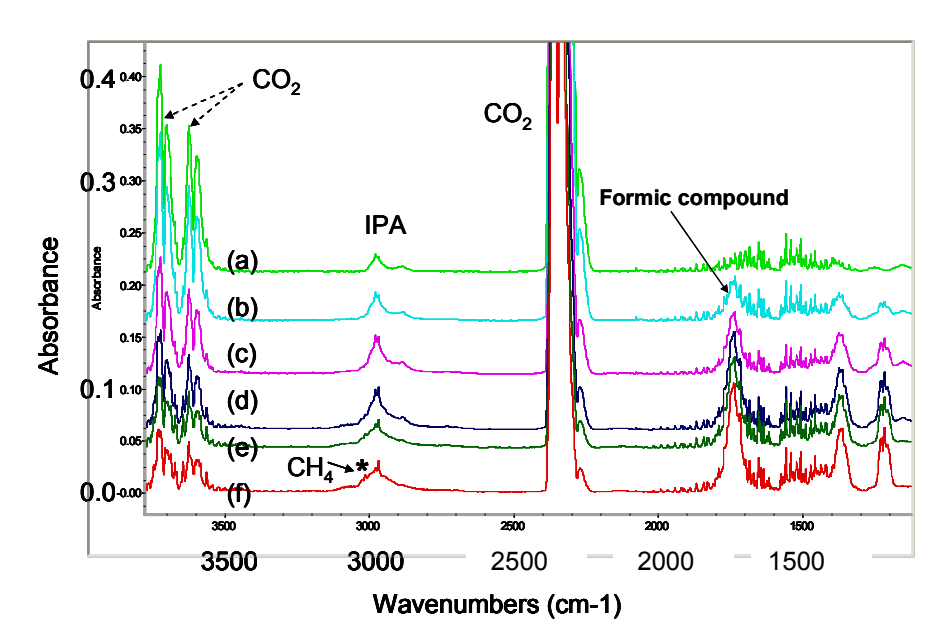


Figure 38. FTIR spectra of gas phase composition in the photocatalytic reactor containing 0.20 g Degussa titania powders immobilized on a stainless steel mesh with the dimensions of 5.5×7 inches under solar simulator radiation, light intensity at the wavelength of 400 nm is 300-400 mW/cm². (a) initial FTIR spectrum, (b) after 1 hour, (c) after 2 hours, (d) after 3 hours, (e) after 4 hours and (f) after 5 hours.

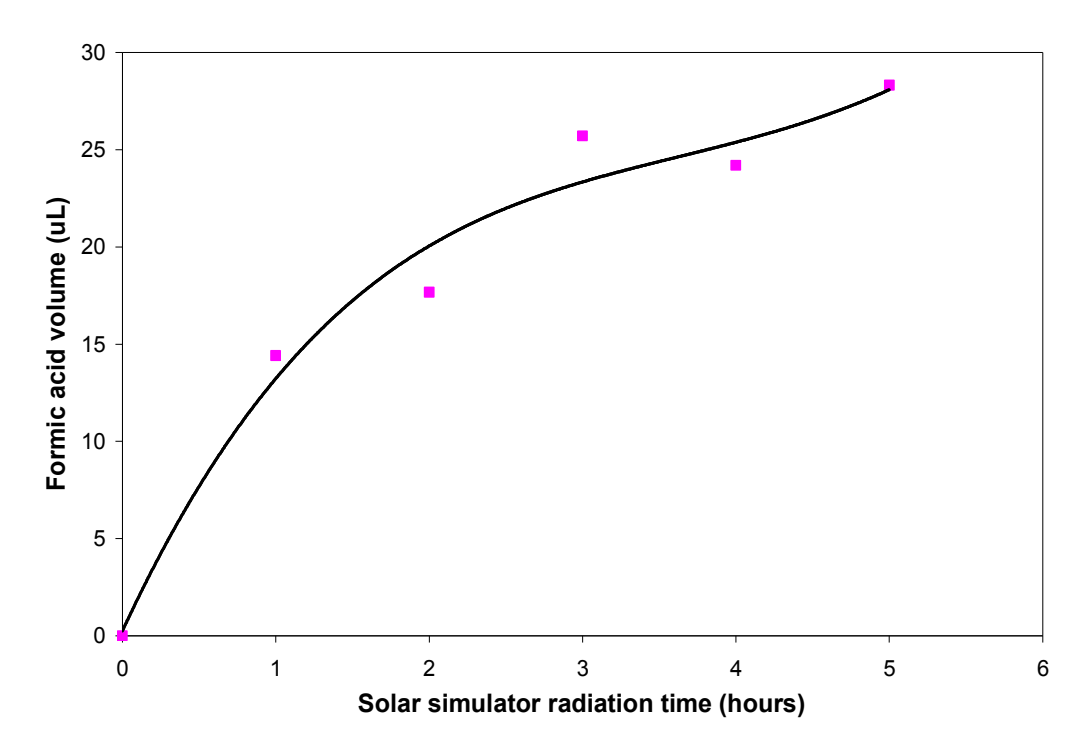


Figure 39. Photocatalytic conversion of CO₂ and water into formic acid using titaniastainless steel mesh system under solar simulator radiation.

Figure 38 and Figure 39 show the results of photocatalytic activity from the titania-stainless steel mesh system under visible radiation from the Oriel solar simulator. It can be observed that the peak intensity of formic compound gradually increases, while the peak intensity of CO₂ gradually decreases with illumination or reaction time. Using the formic acid calibration data we had obtained during the previous reporting period, it was determined that the amount of formic acid have reached 0.1 µL after 5 hours of solar simulator radiation. From these results, it can be concluded that the stainless steel 316 alloy system seems to be a very promising metal substrate for supporting various p-n photocatalyst structures that can be used for the photocatalytic conversion of CO₂ and water into formic acid under sunlight radiation.

From previous results, we've shown that under UV and/or visible light radiation, Degussa P25 titania-stainless steel based photocatalytic system can produce formic acid from CO₂ and water. Since formic acid is an important and transportable chemical, which is also used in some fuel cells (i.e., direct-formic acid fuel cells), we have continued to optimize the titania-stainless system in order to enhance its energy efficiency and formic acid yield.

To build a photocatalytic system suitable for testing in our conventional reactors, 0.065g of P25 titania was immobilized on a 95in² stainless steel mesh, which was then installed in a 45 ml glass reactor. The photocatalytic activity of the system was evaluated under visible radiation and results were obtained after 66 hours of irradiation, as presented in Figure 40. The formic acid yield reached about 2.6 times that of previously

reported levels obtained using a similar titania-stainless steel system with 0.183g of P25 titania immobilized on a stainless steel mesh with an area of 21in^2 . The greater yield can be explained by a better dispersion of the photocatalyst particles on the metal mesh, which resulted in better utilization of light and enhanced photocatalytic activity in converting CO₂ and water into formic acid.

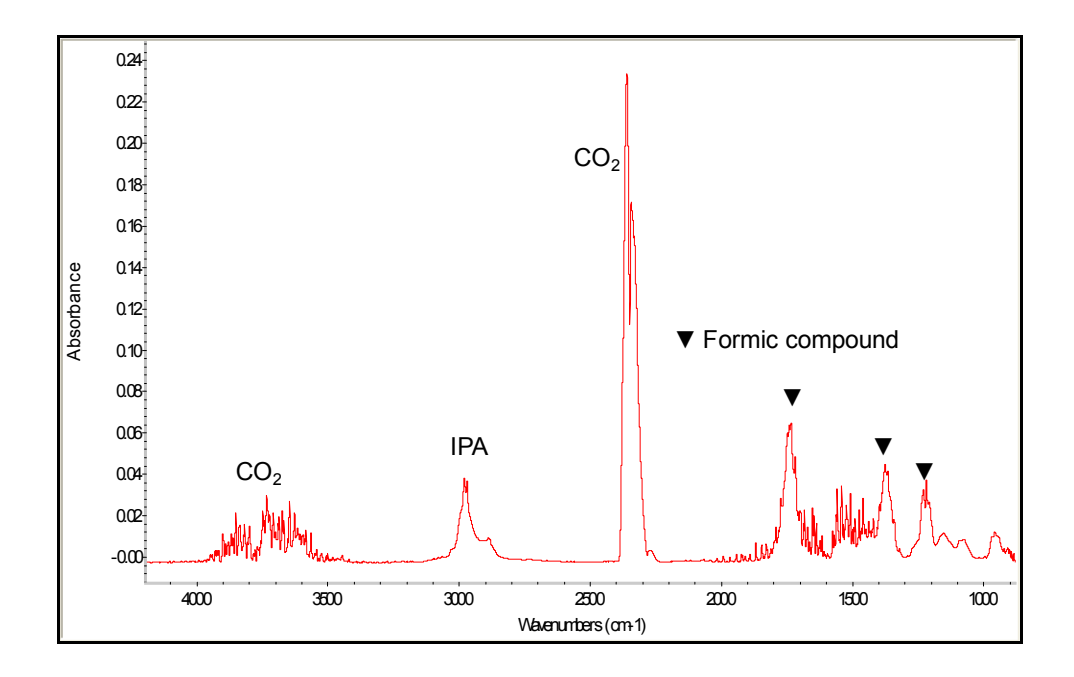


Figure 40. FTIR spectrum of gas phase composition in the photocatalytic reactor containing 0.065g Degussa P25 titania powders immobilized on stainless steel meshes with total 95 sq inches, following 66 hours of visible light radiation.

In addition to using stainless steel as a stable substrate material, nickel was tested with titania for use in photocatalysis. The result is shown in Figure 41. It was found that, although formic acid can be produced, the energy efficiency of Degussa P25 titanianickel mesh based system is only 0.006%, which is much lower than that of the Degussa P25 titania-stainless steel mesh based system. Formation of NiO nanorods on the surface of nickel substrate may enhance the energy efficiency of the titania-nickel mesh system, due to an enhanced surface area and better dispersion of the titania phostocatalyst.

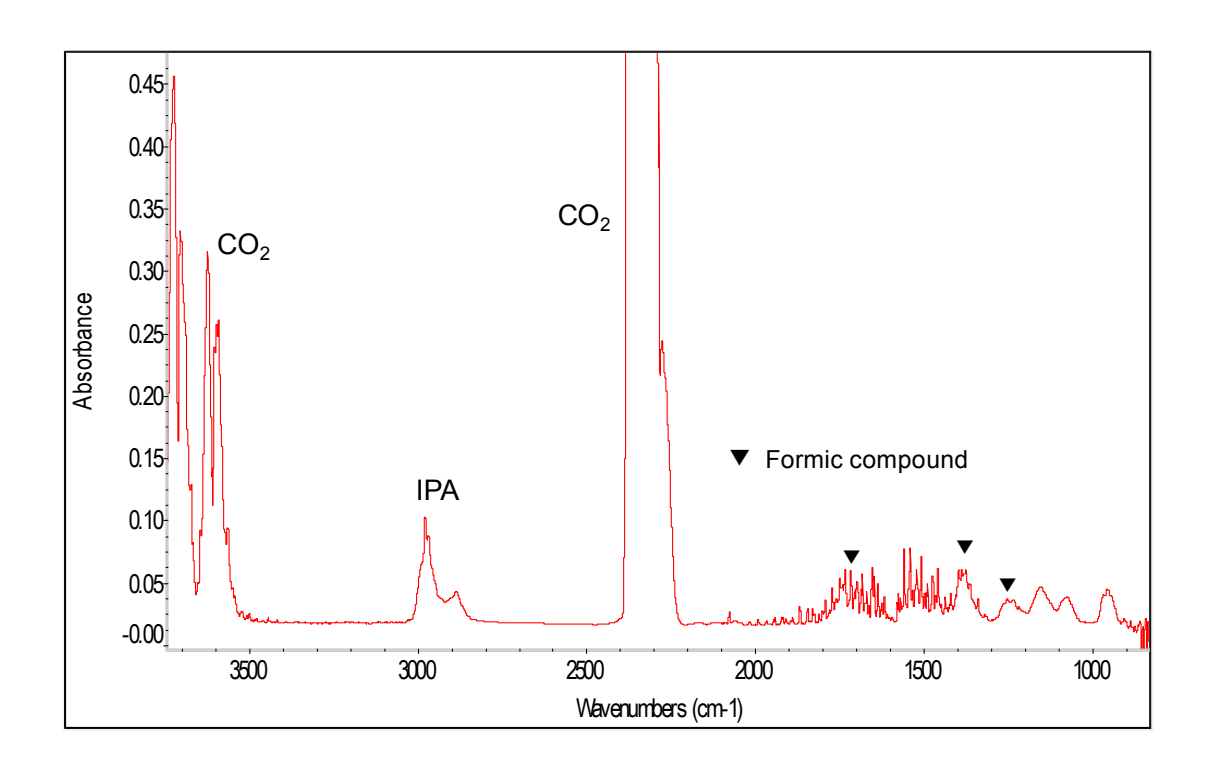


Figure 41. FTIR spectrum of gas phase composition in the photocatalytic reactor containing 0.038g Degussa P25 titania powders attached on a nickel mesh with dimension of 38.5 square inches, after 3 hours of solar simulator radiation with average intensity of 200 mW/cm².

From previous results and simulation work, we've shown that the introduction of a hole-blocking layer can help improve the stability and reduce oxidation of copper-based photocatalytic systems. With the help of the ion-assisted deposition (IAD) system at the Georgia Tech Research Institute, we had fabricated various titania-CeO₂-copper structures based on the optimized model and found that the CeO₂ layer, as a hole barrier, can indeed protect copper from oxidation as predicted by the model (refer to Figure 42).

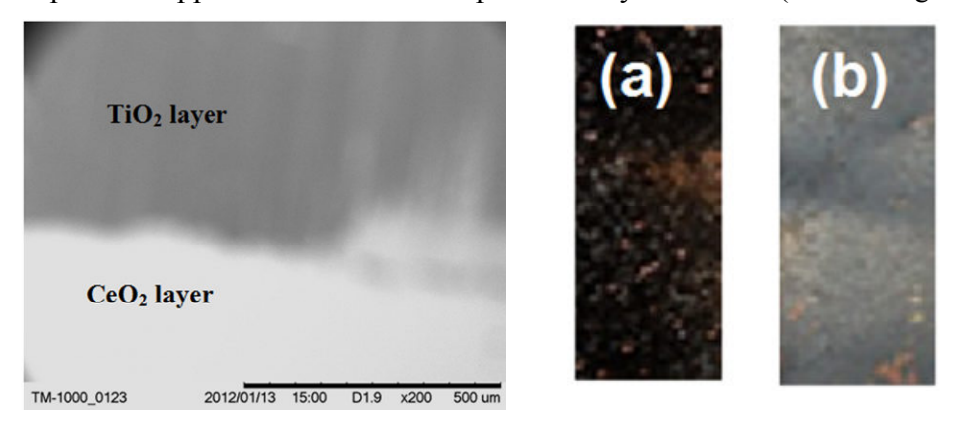


Figure 42. (Left) SEM image showing different areas on Cu foil with CeO₂ and CeO₂+TiO₂ layers deposited by electron-beam evaporation. (Right) Photographs of Cu metal foil after 500 °C calcination. (a) un-coated copper foil and (b) CeO₂-coated copper foil

Testing the photocatalytic activity of the titania-CeO₂-copper system revealed a combination of methane and formic acid compounds, as a result of CO₂ reforming, which is illustrated in Figure 43.

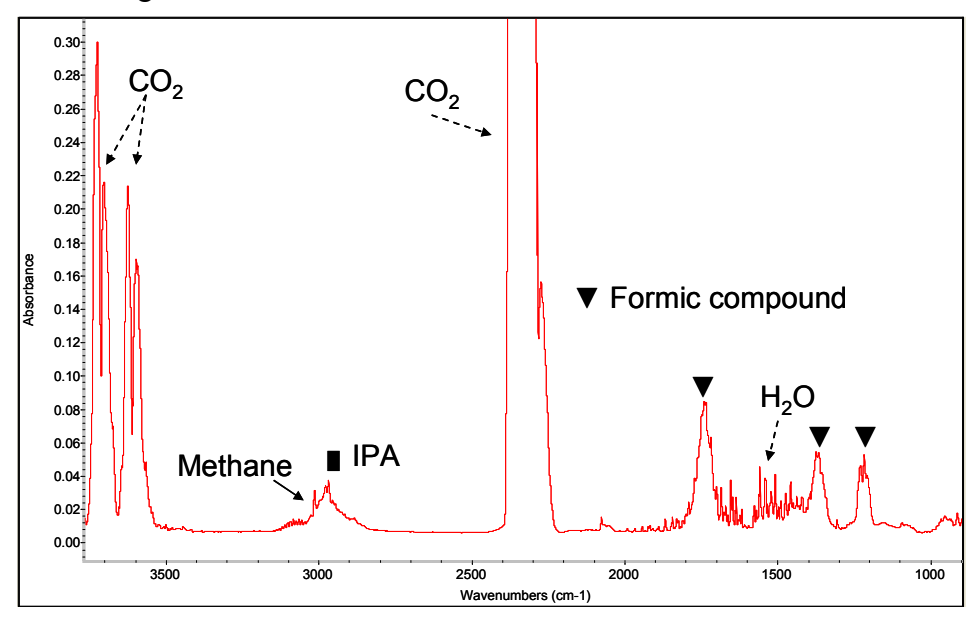


Figure 43. FTIR spectra of gas composition in the photocatalytic reactor with 0.097g Degussa P25 titania -CeO₂-copper system (3.5×5.1 inches), following 115.5 hours of UVA radiation with average intensity of ~ 8 mW/cm²

While the Degussa P25 titania-CeO₂-copper structure have shown stable long-term photocatalytic activity in converting CO₂ and water into hydrocarbons, the initial activity or yield was nevertheless lower than that of the simpler P25 titania-copper systems. Based on the original model predictions, this was to be expected since the introduction of the additional CeO₂ layer tends to absorb and scatter light away from the TiO₂ and CuO semiconductors.

In addition, we've also modified the copper substrate by the deposition of 100-200nm Ni and Cr (NiCr) metal alloy on the surface, also by IAD. The experimental results also show that both methane and formic acid can be produced simultaneously within the NiCr modified titania-copper structure under UV radiation.

We have also modified stainless steel substrates by the deposition of NiCr surface metal nanowires using the IAD's Glancing Angle Deposition (GLAD) method at Ga Tech. The as-prepared titania-NiCr-stainless structure has shown advantages over the previously reported titania-stainless system because (i) NiCr nanowires provide larger surface area for supporting the nanosized titania photocatalyst, (ii) such a semiconductor-composite metal system seems to exhibit further enhancement in the reforming activity once the NiCr nanowires are oxidized by holes produced via photocatalysis. Such an enhancement in the photocatalytic activity is believed to be the result of the formation of NiO and Cr₂O₃ surface layers, which serve to both protect the iron in the stainless steel from oxidation and to provide a narrow-bandgap PN semiconducting junction layer for

increased sunlight absorption and reduced electron-hole recombination rate. The increased sunlight absorption was confirmed by UV-visible spectroscopy of oxidized stainless steel substrates, as shown in Figure 44 where the absorbance extends all the way into the near-infrared. Experiments using these structures showed that formic acid is produced from CO₂ and water in less than 2.5 hours of exposure to solar simulator radiation, as illustrated in Figure 45.

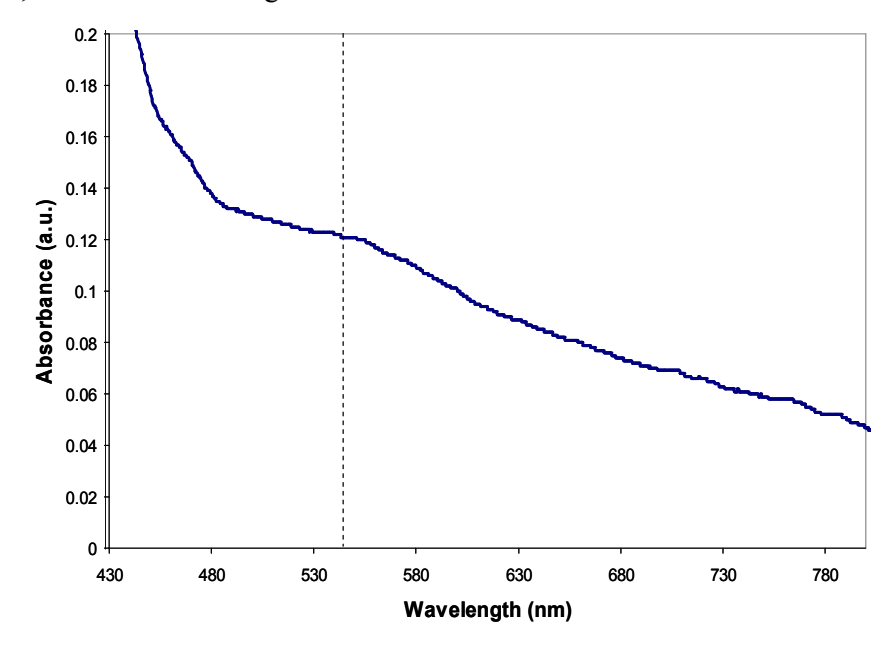


Figure 44. UV-visible spectrum of oxidized stainless steel (500 °C, 15min)

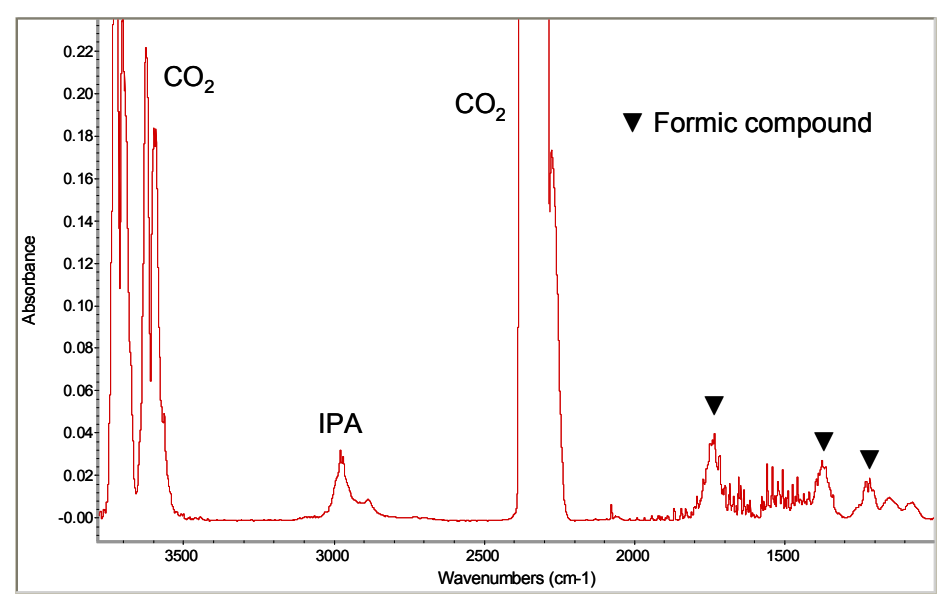


Figure 45. FTIR spectrum of gas composition in the photocatalytic reactor with 0.088g Degussa P25 titania –stainless steel mesh (3x7 inches) modified by NiCr nanowires. After 2.5hrs of solar simulator radiation with average intensity of \sim 200 mW/cm²

Moreover, we continued refining the stainless-based photocatalytic reactor system for the formation of formic acid from CO₂ gas under sunlight. With the help of the ion-

assisted deposition (IAD) system at the Georgia Tech Research Institute, several stainless substrates were surface-modified using Ni/Cr nanostructures. Some of the modified structures were then oxidized in an oven at 500°C, in order to form a p-n junction of TiO₂-NiO/Cr₂O₃ and improve solar light absorbance with reduced electron-hole recombination.

Figure 46 shows photos comparing the body colors of the Ni/Cr modified stainless surface area (a) with that of the unmodified surface (b) following oxidation. The color of the modified surface is yellow-green, while that of the original surface turned brown due to the formation of iron oxide. Therefore, the Ni/Cr nanostructures clearly protect the stainless substrate from rusting/oxidation, which is beneficial for maintaining long-term stability of the substrate.

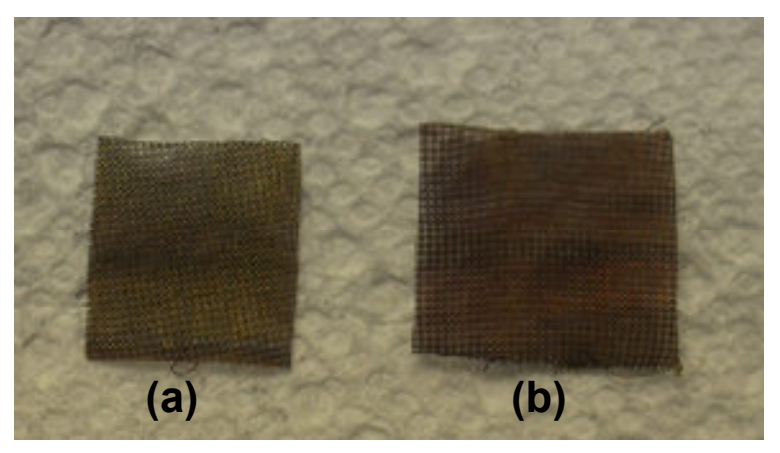


Figure 46. Photographs comparing oxidized stainless steel mesh surfaces with and without modification by Ni and Cr nanostructures (following 500°C oven heat treatment for 1 hour in air). (a) stainless steel mesh surface modified with Ni/Cr nanostructures, (b) Non-modified stainless steel mesh surface.

In order to confirm that the GLAD deposition technique did indeed enhance the Ni/Cr levels on the surface of the stainless alloy, SEM/EDS analysis of the modified substrates was performed and compared to the results from the non-modified surface. The results are shown in Figure 47, which further confirms that the nickel surface concentrations doubled, while that of chromium increased by about 33%.

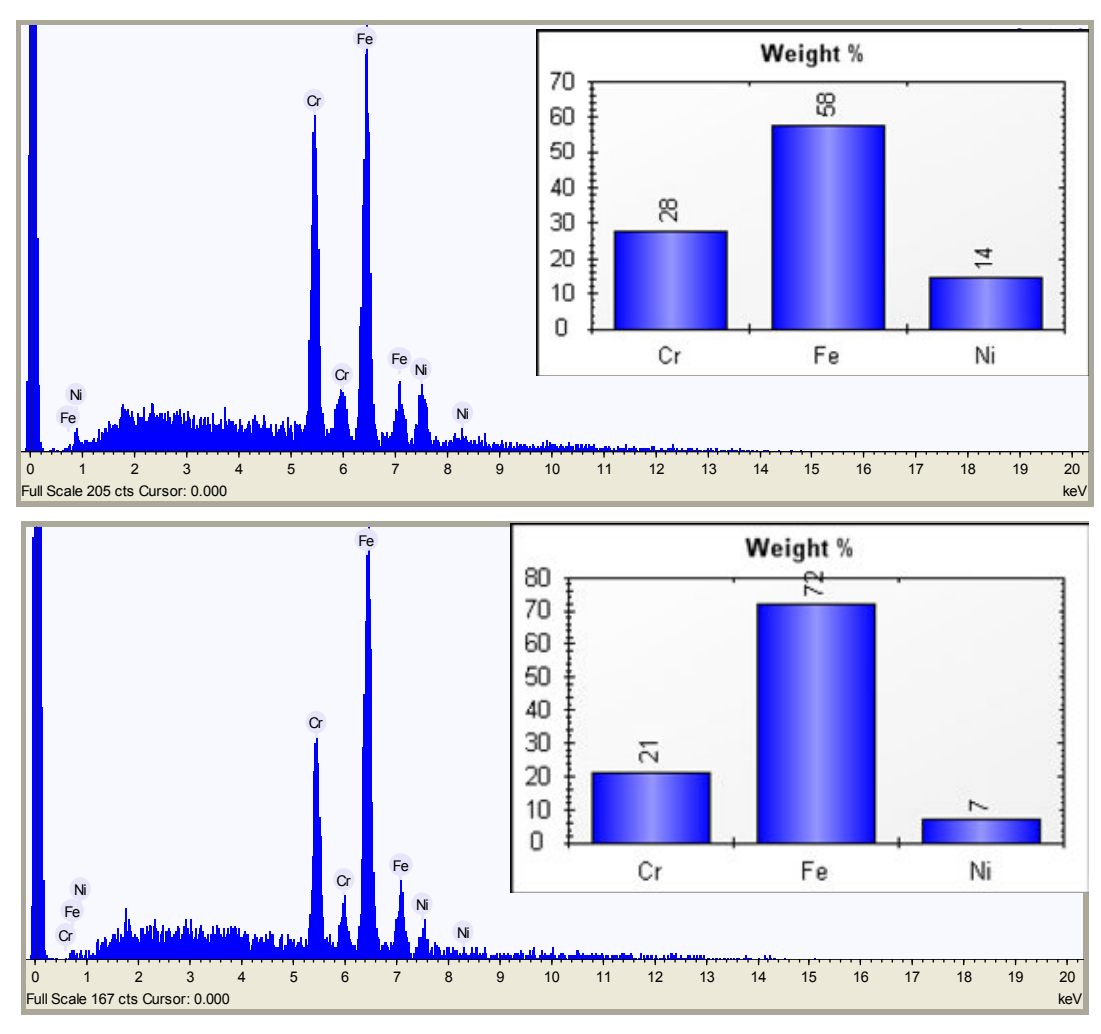


Figure 47. Top: EDS analysis of the stainless steel surface modified by Ni/Cr using GLAD deposition. Bottom: EDS analysis of non-modified stainless steel mesh showing original concentrations of Ni and Cr in the stainless alloy.

Figure 48 shows the result on photocatalytic activity of the titania-stainless steel mesh modified by Ni/Cr metal nanostructures, which had been oxidized in an oven in air at 500°C for 1 hour. A continuous mode photocatalytic reactor system was employed for such an experiment. Although neither the metal compositional ratio nor the heat treatment conditions are fully optimized, a formic acid peak was observed after 2.5 hours of visible light exposure from the Oriel solar simulator.

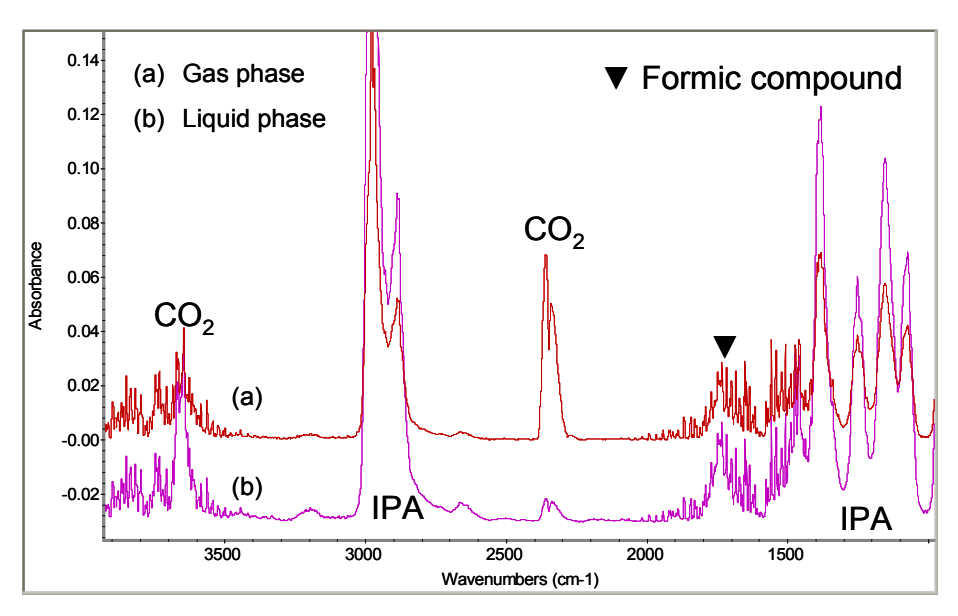


Figure 48. FTIR spectra of gas phase composition in a continuous photocatalytic reactor system with oxidized titania-stainless steel modified by Ni/Cr metal nanostructures followed by oxidation at 500°C, 1 hour. Reaction time: 2.5 hours of solar simulator radiation with light intensity of ~150 mW/cm².

Task 4.0 Refinement of CO₂ reactor

This task aims at refining p-n photocatalyst structures using more complex vacuum deposition technologies that promote polycrystalline or columnar structures in order to compare performance with the low-cost solution-deposition techniques that have been discussed and tested so far.

4.1 Development of Thin-film Deposition Process

One method of yielding nano-scale structures that is capable of process control such that three dimensional geometries of the structures are easily created using glancing angle deposition (GLAD). Glancing angle deposition is a physical vapor deposition method that was developed and optimized to yield highly porous microstructures. The processes are characterized by a symmetrical, oblique flux incident on the substrate surface, which is gained by employing multiple evaporation sources or substrate movement. The GLAD technique employs substrate tilt angles greater than 70° with respect to normal incidence, this angle can be altered during the deposition process if the substrate mount is equipped with a controllable motor. The processes utilize the oblique angle of the incident flux to generate atomic shadowing on the substrate, which is responsible for the unique growth mechanisms characteristic of this technique. Substrate movement during glancing angle deposition (GLAD) processes can be implemented to control the morphology of the nano- or microstructures created by the deposition.

Figure 49 shows an e-beam evaporation system and substrate control setup we used for GLAD of nanoporous TiO_2 structure at Georgia Tech Research Institute (GTRI). The substrate is oriented so that flux arrives at substrate at highly oblique angles of incidence, determined by α and α_{tilt} . Typically α is $\sim 70^{\circ}$ or higher. The substrate can be rotated

about axis, ϕ , to create various nanostructure geometries. The chamber is maintained at high vacuum during deposition because the atoms must travel in a linear trajectory and create shadow effect.

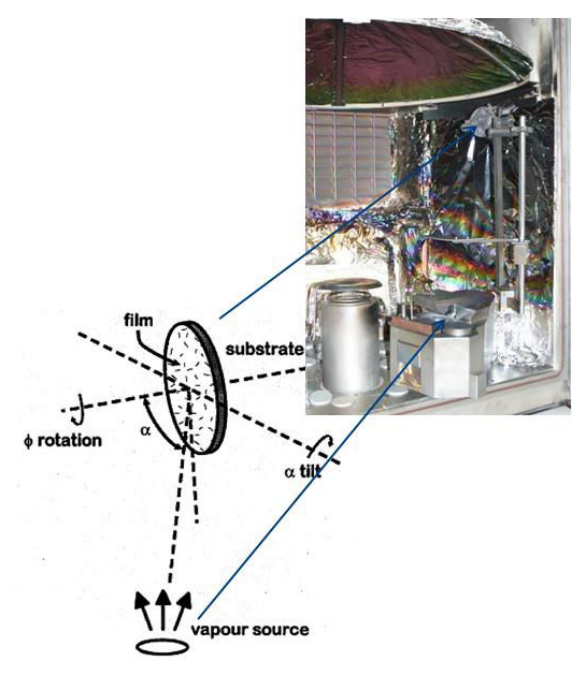
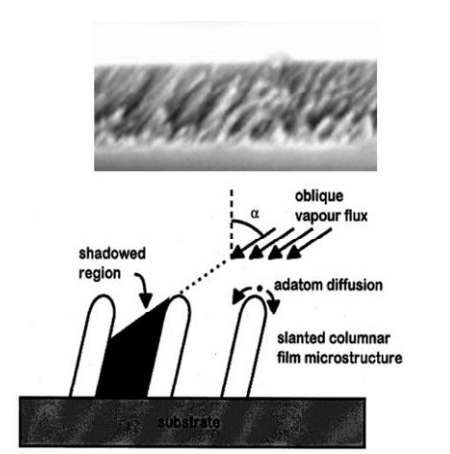


Figure 49. E-beam evaporation system and GLAD substrate control setup used for TiO₂ nanostructure growth at Georgia Tech Research Institute

The thin films produced by this method of fabrication have been reported to have densities as low as 15% of that of bulk material density and the microstructure of the films are significantly altered from conventional means of deposition, which is without the use of oblique angles, such as the conventional electron beam evaporation method. The porosity of GLAD thin films arises from the unique columnar/nanorod structures that are created by this method of fabrication as shown in Figure 50(left). The angle at which the columns incline can be controlled, as it correlates to the angle of incidence to which the flux reaches the surface of the tilted substrate. The nanorod columns are inclined towards vapor source, however do not grow parallel to vapor source, are more vertical. When direction of vapor flux varies, the growth of individual nanorods follows the position of the source. Therefore, the morphology of the structures can be controlled by rotating the substrate during the deposition to yield helical, chevronic or zig-zag structures, among others. Various substrates, including Ti foil, Cu mesh, Si wafer and Cu foil were used to grow TiO₂ nanoporous thin film samples as shown in Figure 50 (right). Different glancing angle $\alpha = 75^{\circ}$ and 85° were used to control the porosity. The film growth rate of ~ 0.1 nm/s was used and the film thicknesses were ~ 200 nm.



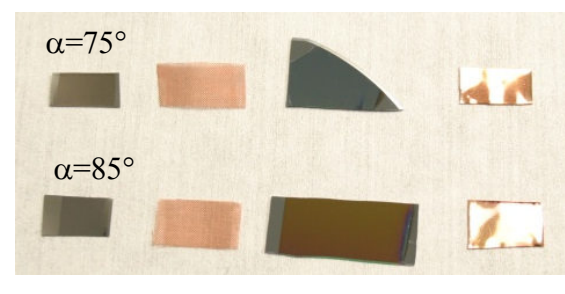


Figure 50. (left) Unique columnar/nanorod structures created by GLAD due to shadow effect. The top image shows the TiO_2 nanorod structure prepared at GTRI. (right) GLAD thin films prepared on various substrates with glancing angle $\alpha = 75^{\circ}$ and 85° .

Depending on the process parameters, the type of material being deposited and the desired thickness, GLAD thin films can be fabricated in as little time as half an hour. As the GLAD method utilizes E-beam or thermal evaporation to create the gas-phase reactant, there is almost no limit to the materials that can be implemented to create thin films for a vast array of devices. The nanostructured films can be fabricated from semiconductors, metals, insulators for this project. The combination of a near-limitless suitable material and substrate possibilites, formation of microstructures with many easily-creatable geometric forms and the fact that GLAD is a single-step process makes this fabrication technique extremely appealing for the creation of nanoporous devices for this project.

Glancing angle deposition of nano-porous TiO₂ structure will greatly increase the surface area. The porosity can be controlled by the glancing angle as shown in the SEM (Figure 51). For a smaller glancing angle of 75°, the porosity is much less than the film prepared with a larger glancing angle of 85° as indicated by the surface and cross section images. Island formation is the most common growth mode used in glancing angle deposition. At oblique angles of flux incidence, formation of islands leads to the type of microscopic topology that makes ballistic shadowing possible. The first islands to be formed will block, or shadow, the area directly behind it from receiving any flux. As the glancing incident vapor flux is nearly parallel to the substrate, the shadow areas become more extreme as the structure gains height, causing formation of the highly porous nanorods that usually incline toward the vapor flux. Creation of nanostructured films rather than planar films results in the deposition of a layer of material characterized as having an extremely high surface area to volume ratio. This property of the film is especially appealing for catalyst application, which requires large amounts of surface area to optimize process efficiency to a much higher rate than found in conventional devices. The amount of surface area that can be produced by this technique can be controlled to some extent.

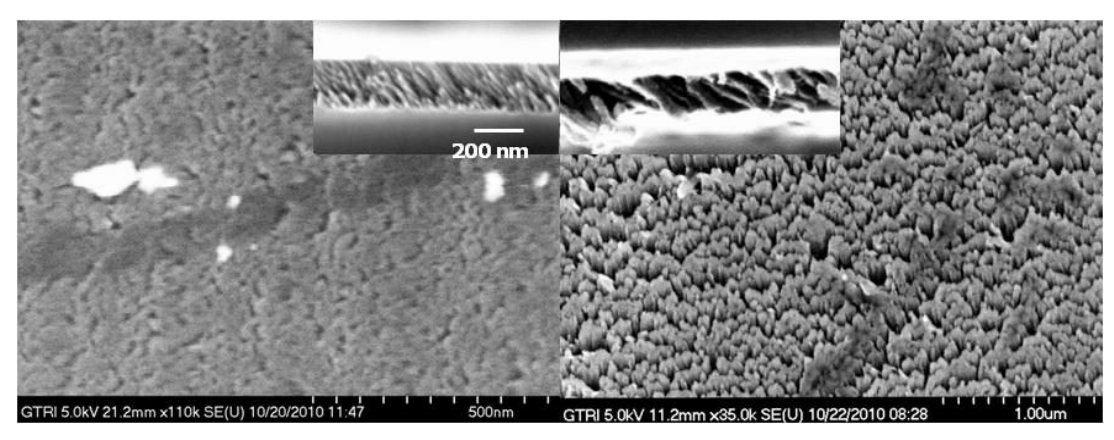


Figure 51. Surface and cross section SEM images for TiO_2 GLAD thin films deposited on Si wafers. (left) $\alpha = 75^{\circ}$; (right) $\alpha = 85^{\circ}$.

The reflectance spectra of these films were measured and shown in Figure 52 with a comparison to the normally deposited dense films. It can be observed that for a smaller glancing angle 75°, the secular reflectance spectrum is similar to the normally deposited film (0°) with some changes in the reflectance peak positions; while with the increase of α to 85°, the spectrum profile changed significantly and a more uniformly diffused reflection was observed at difference wavelengths due to the increased porosity. The thin film interference effect was also diminished with an overall decreased reflectivity, which is a benefit for light induced catalytic applications.

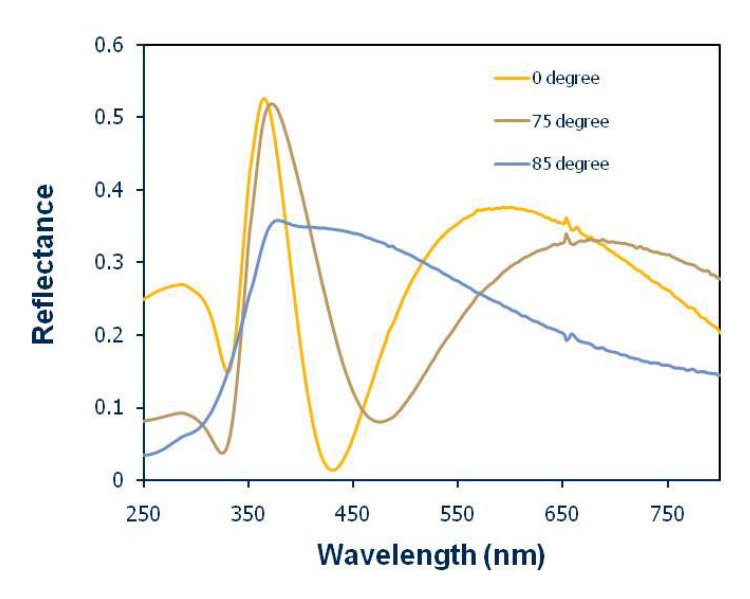


Figure 52. Reflectance of TiO_2 film prepare by GLAD with glancing angle a = 75° and 85°, with a comparison to normal deposition

Glancing Angle Deposition (GLAD) is a technique developed to allow for fabrication of large area nanostructured thin films. The combination of a near-limitless suitable material and substrate possibilites, formation of microstructures with many easily-creatable geometric forms and the fact that GLAD is a single-step process makes

this fabrication technique extremely appealing for the creation of nanoporous devices for this project. A basic GLAD setup resembles e-beam PVD operated under Volmer-Weber growth conditions. Source material is placed in a crucible inside a vacuum chamber and vaporized via an electron beam. Unlike in e-beam PVD, the substrate in a GLAD apparatus is mounted so that the source flux is incident upon the substrate surface at a glancing angle on the order of 65°-95° from the normal. Atoms from the vapor are adsorbed onto the surface of a smooth substrate also mounted inside the vacuum chamber, and the resulting adatoms diffuse across the substrate surface. Under Volmer-Weber growth conditions, the adatoms form into localized islands known as nuclei. The three-region structure zone model (SZM) proposed by Movchan and Demchisin describe three different morphology types for these nuclei. The first type, and the one most important one for GLAD growth, occurs at the low temperature regime in which adatom diffusion is low enough to allow formation of packed vertical nuclei.

As material accumulates, taller nuclei begin to shadow surrounding areas of lesser height from the incident flux. These nuclei continue to collect material, growing taller and further increasing the local shadowing effect. Such preferential deposition of material on the tops of the highest regions of growth leads to the formation of parallel columnar nanostructures, schematically illustrated in Figure 53. Low adatom mobility on the surface of these columns is necessary to prevent them from "melting" back onto the surface or swapping material with other columns. Thus, deposition must occur at low enough temperatures to promote proper nucleation and prevent this bulk diffusion.

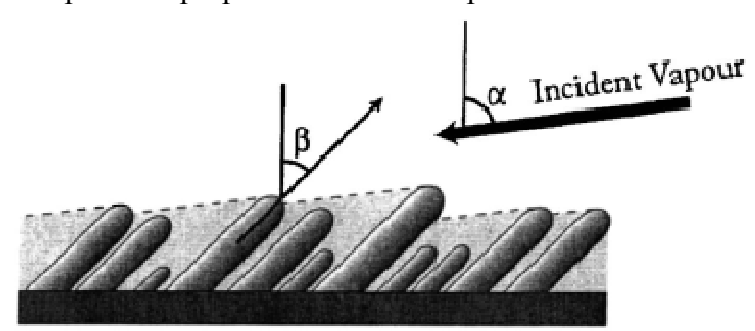


Figure 53. Schematic of GLAD column growth via shadowing for TiO_2 nanostructure growth at Georgia Tech Research Institute

Much work has been done in the last 15 years since the introduction of the GLAD process by Robbie and Brett in 1995. One of the greatest features of GLAD is the control on surface morphology and porosity by the deposition angle. Illustrated schematically in

Figure 54 (left), the deposition angle affects not only column angle β , but also the inter-column shadowing. The porosity of TiO_2 films can be controlled by the glancing angle as shown in the SEM

Figure 54 (right). For a smaller glancing angle of 75°, the porosity is much less than the film prepared with a larger glancing angle of 85° as indicated by the surface and cross section images. Island formation is the most common growth mode used in glancing angle deposition. At oblique angles of flux incidence, formation of islands leads to the type of microscopic topology that makes ballistic shadowing possible. The first islands to

be formed will block, or shadow, the area directly behind it from receiving any flux. As the glancing incident vapor flux is nearly parallel to the substrate, the shadow areas become more extreme as the structure gains height, causing formation of the highly porous nanorods that usually incline toward the vapor flux. Creation of nanostructured films rather than planar films results in the deposition of a layer of material characterized as having an extremely high surface area to volume ratio. This property of the film is especially appealing for catalyst application, which requires large amounts of surface area to optimize process efficiency to a much higher rate than found in conventional devices.

The nanostructured GLAD films can be fabricated from semiconductors, metals, or insulators for this project. Depending on the process parameters, the type of material being deposited and the desired thickness, GLAD thin films can be fabricated in as little time as half an hour. For TiO₂ films deposited with glancing angle $\alpha = 95^{\circ}$, the growth rate was about 0.14 nm/s and films with thicknesses of ~2 μ m were grown on various substrate. Figure 55 and Figure 56 show the SEM images of this film on a flat Si wafer substrate. Various substrates, including Cu mesh, Al mesh, Si wafer and ITO glass were used to grow TiO₂ nanoporous thin film samples as shown in Figure 57. Different glancing angle $\alpha = 75^{\circ}$, 85° and 95° were used to control the porosity. Arrays of nanorods could be observed from both of the surface morphology with a tilted observing angle and the cross section image of TiO₂ on Si. The diameter of these rods/columns is less than 100nm. But the columns and other structures are found to become broader as the deposition process continues. This competitive broadening phenomenon limits the height to which the columns may be grown and disrupts the uniformity of the film, as the columns eventually merge.

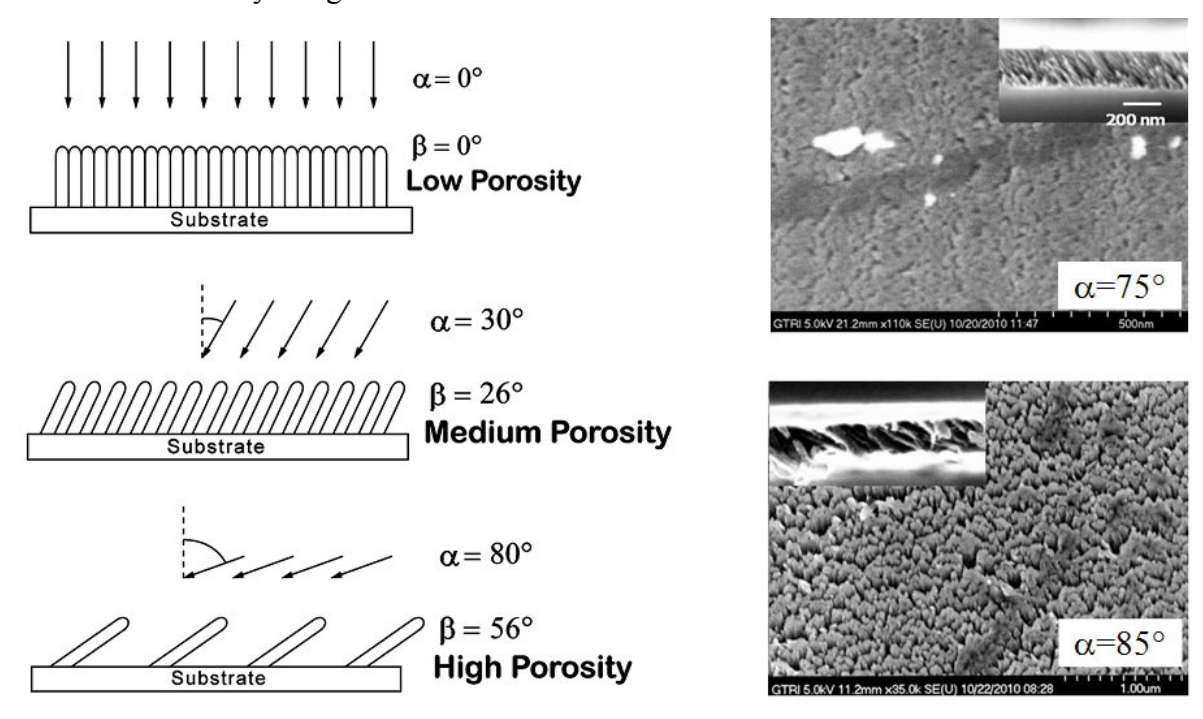


Figure 54. (left) Deposition angle dependence of porosity; (right) Surface and cross section SEM images for TiO_2 GLAD thin films deposited on Si wafers with $\alpha = 75^{\circ}$ and 85° .

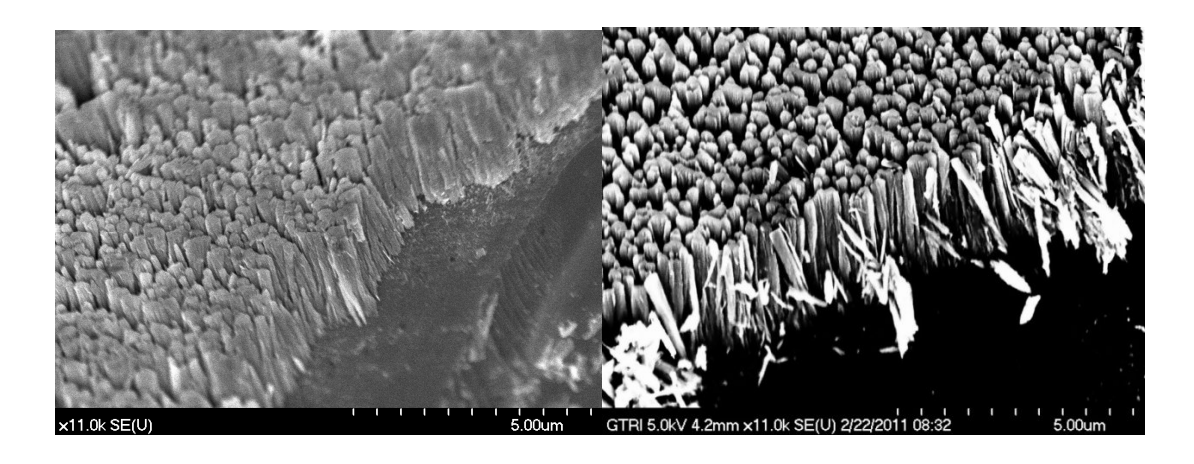


Figure 55. Surface morphology of TiO_2 nanoporous film grown with glancing angle $\alpha = 95^{\circ}$ and observed from a tilted angle.

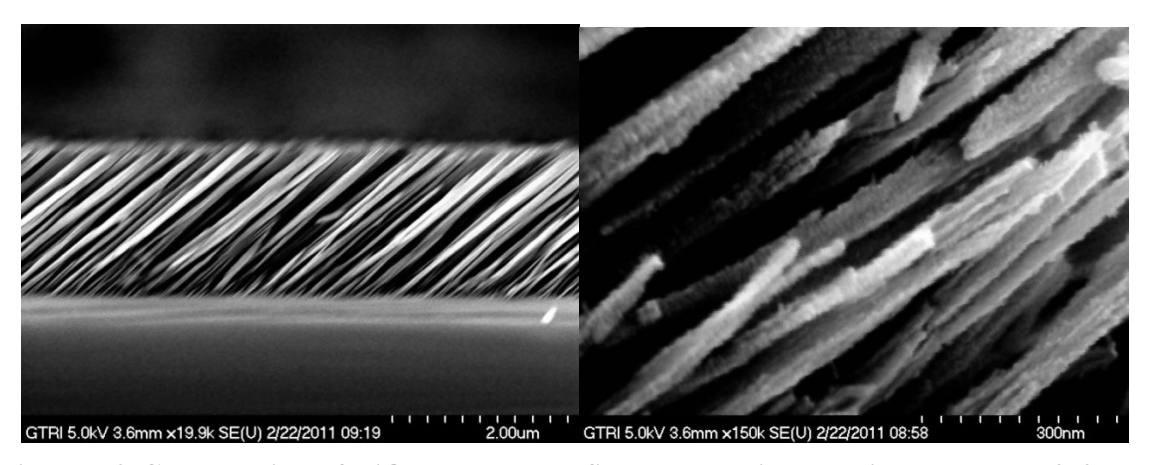


Figure 56. Cross section of TiO_2 nanoporous film grown with glancing angle α = 95° and thickness of ~2 μ m.

It has been reported that a number of different growth methods have been developed for GLAD in which rotation of the substrate along can be used to reduce or even eliminate this broadening effect, allowing for finer control of the morphologies produced. When direction of vapor flux varies, the growth of individual nanorods follows the position of the source. Therefore, the morphology of the structures can be controlled by rotating the substrate during the deposition to yield helical, chevronic or zig-zag structures, among others.

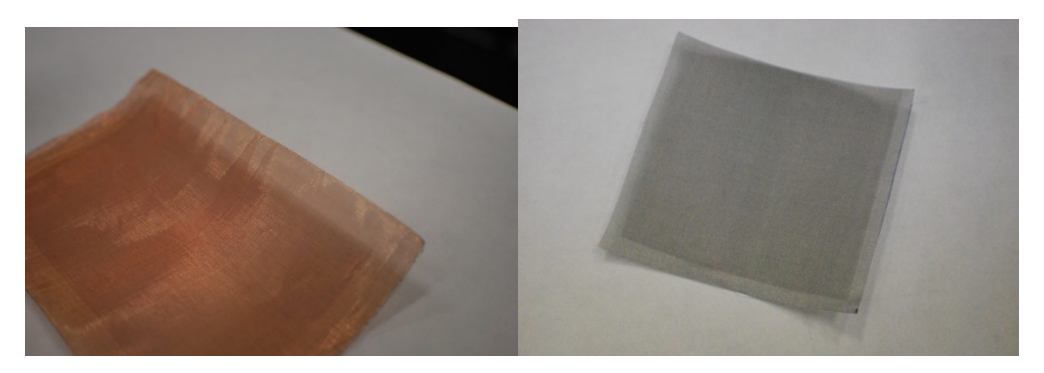


Figure 57. Photos of TiO₂ nanoporous films grown by GT on Cu (left) and Al (right) meshes.

Glancing Angle Deposition (GLAD) was used to grow TiO_2 nanostructures on large-sized substrates at Georgia Tech. Cu mesh and foils provided by PhosphorTech were used as substrates to grow porous TiO_2 film samples. Different glancing angle $\alpha = 65^{\circ}$, 75° and 85° were used to control the porosity. For TiO_2 films deposited with glancing angle $\alpha = 85^{\circ}$, the growth rate was about 0.14 nm/s and films with thicknesses of $\sim 2~\mu m$ were grown on various substrates. Typically arrays of nano columns could be observed from both of the surface morphology and the cross section SEM images of TiO_2 on flat Si substrate as discussed in the previous reports. The diameter of these columns is less than 100nm.

However, when a Cu mesh was used as the deposition substrate as shown in Figure 58, the mesh rods exhibited a round surface with changing deposition angle ranging between -180° < α < 180°, which is also affected by the rod orientation. Thus, the deposited film structure varied across the mesh rod surface. As shown in Figure 59(a), on a horizontally-oriented mesh rods, the deposition angle is equal to the glancing angle on the rod surface, thus porous structures were obtained. While on a vertically-oriented mesh rod as shown in Figure 59(b), with the change of deposition angle related to the vapor evaporation direction on the rod surface, layered structures were developed and observed.

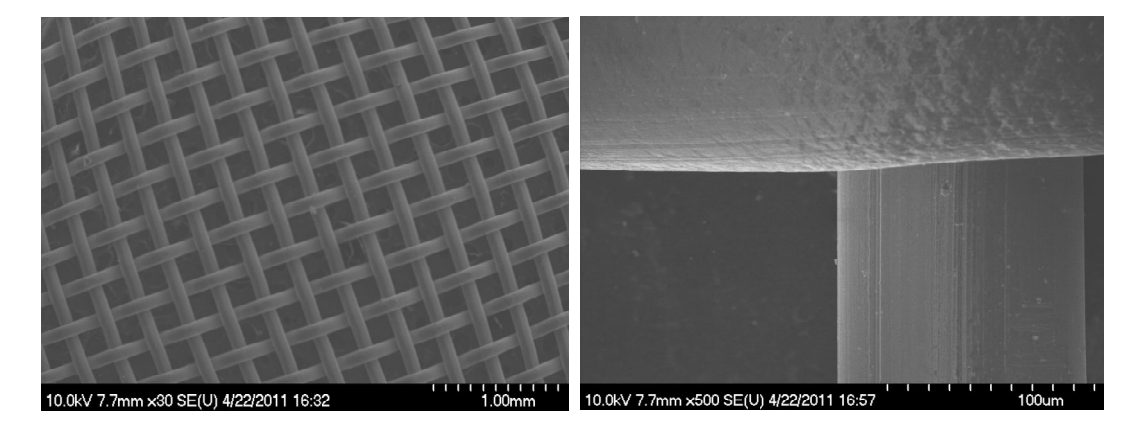
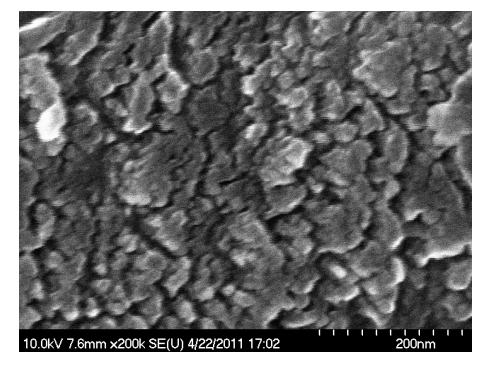


Figure 58. (a) SEM image of TiO₂ on a Cu mesh; (b) Effect of mesh rod orientation on TiO₂ structures.



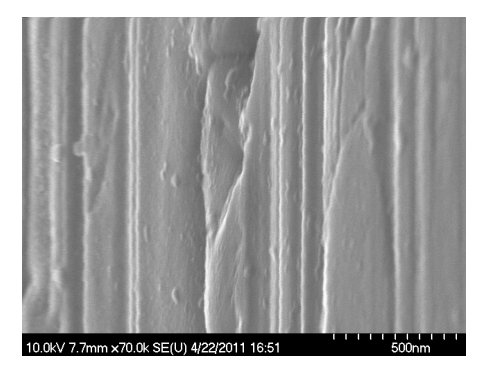


Figure 59. SEM images of TiO₂ structure on horizontally oriented (a) and vertically oriented (b) mesh rods

Flat Cu foil substrate was also used to grow large area TiO_2 nanostructure. As shown in Figure 60(a), a 6x6 inch sample with ~2 µm porous TiO_2 on the Cu surface was obtained using a glancing angle $\alpha = 85^{\circ}$. The sample looks a little frosty from only one viewing direction as indicated in Figure 60 (b) probably because light is more preferably reflected from the nano-columns in this direction.

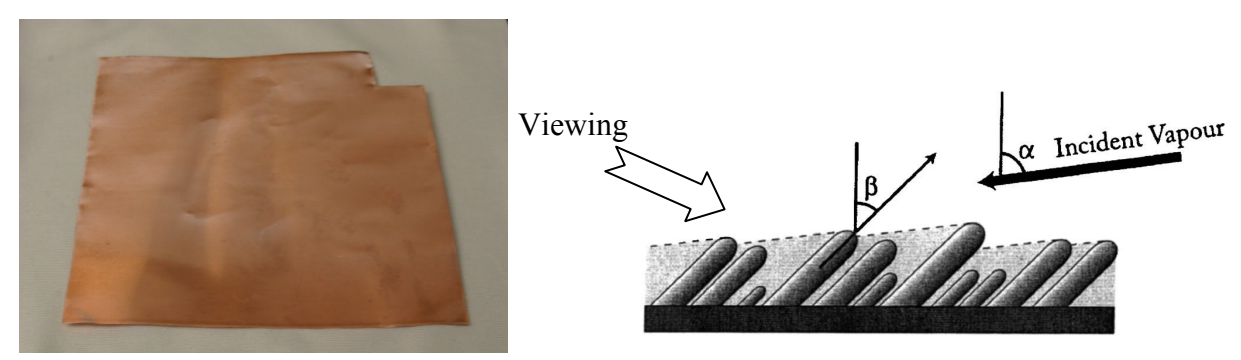


Figure 60. (a) Photo of a TiO₂ nanoporous film grown on a 6x6 inch Cu foil; (b) Viewing direction of frosty appearance from the TiO₂ nano-columns.

To prevent Cu oxidation during the photo activated electrochemical reaction between TiO₂ and CO₂ in water, ZnO or CeO₂ thin films were grown on the Cu surface before the incorporation of TiO₂. Ion assisted deposition was used to deposit these thin films on the front and back sides of Cu meshes. As shown in Figure 61, (a) is a 3x8 inch Cu mesh with 100nm ZnO coated on both sides. The deposition rate is 0.1nm/s and substrate temperature is 100°C during deposition. It can be observed that most regions of the Cu mesh looks dark, probably due to oxygen deficiency in ZnO. Figure 61(b) shows a 7x7 inch Cu mesh with CeO₂ coated on both sides. The deposition rate is 0.1nm/s and substrate temperature is 100°C.



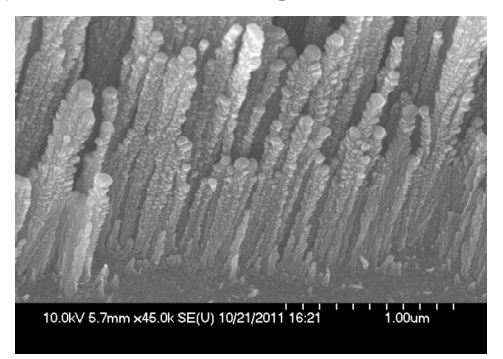
Figure 61. (a) A 3x8 inch Cu mesh coated with 100 nm ZnO film on both sides; (b) A 7x7 inch Cu mesh with 50 nm CeO₂ coated on the front side and 95 nm CeO₂ on the back.

In addition, CeO₂ coated Cu foils were used as substrates to grow porous TiO₂ film samples. Ion assisted deposition was used to deposit CeO₂ thin films on the front and back sides of the Cu foils. The photo in Figure 62 (Left) shows a 7x7 inch Cu foil with 200nm CeO₂ coated on both sides. The deposition rate was 0.1nm/s and the substrate temperature was maintained at 100°C throughout the deposition. The photo in Figure 62 (Right) shows a porous TiO₂ nanostructure thin film grown on a 3x7 inch CeO₂-coated Cu foil also prepared by GLAD. Glancing angle $\alpha = 85^{\circ}$ were used to control the porosity. The growth rate was about 0.15 nm/s and the film thicknesses is ~2.5 μ m on top of the CeO₂-coated Cu substrate.





Figure 62. (Left) A 7x7 inch Cu foil with 200 nm CeO₂ coated on the front and back sides; (Right) TiO₂ nano-columns grown on a 3x7 inch CeO₂ coated Cu foil by GLAD.



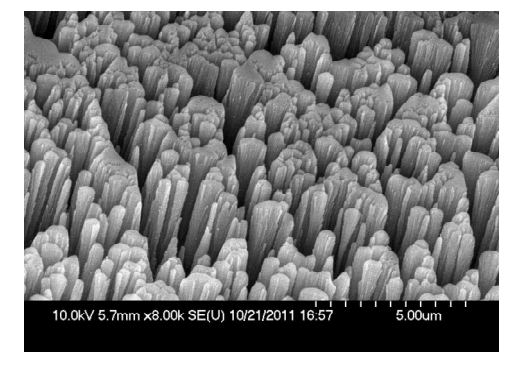


Figure 63. (Left) TiO_2 nano-columnar structure grown on CeO_2 -coated Cu foil with glancing angle α =85° and observed from a tilted angle. (b) Surface morphology of TiO_2 nano-columnar structures

Figure 63 (Left) and (Right) show SEM images of the porous TiO₂ nano-columnar structures grown on a flat CeO₂ coated Cu foil substrate. Arrays of nanorods could be observed from both of the edge of the substrate with a tilted observing angle and the surface morphology of TiO₂ on Cu foil. The diameters of these rods/columns are less than 100nm when they are close to the substrate. But the columns and other structures are found to become broader as the deposition process continues. This competitive broadening phenomenon limits the height to which the columns may be grown and disrupts the uniformity of the film, as the columns eventually merge as shown in Figure 63 (Right). The TiO₂ films on CeO₂ coated Cu foil were annealed at 450°C for 2 hours to fully crystallize the TiO₂ and obtain anatase phase structure. The morphology was not changed after annealing.

In addition, the optimized thin-films of Cu₂O/CuO grown on Cu foils during the last

reporting period were further analyzed using the Oriel Solar Simulator system. The absorption spectrum of a 50nm thin-film was measured throughout the visible and near-infrared (VIS/NIR) from 400nm to about 900nm and the results are shown in Figure 64. The peak absorption is in the blue-green part of the spectrum at around 470nm and drops gradually towards the red and infrared. The average absorption value in the below spectral range is around 27%, which is almost at the 30% target value planned for the end of Q1/BP2.

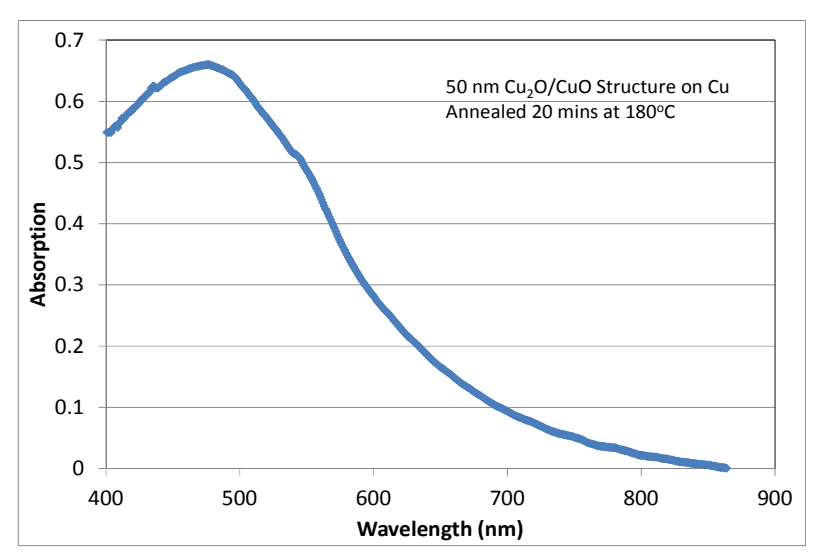


Figure 64. VIS/NIR absorption spectrum of 50nm Cu₂O/CuO thin-film grown on Cu at 180°C

Throughout the project, Glancing Angle Deposition (GLAD) was continually used to grow various nanostructures on both Cu foil and Cu mesh at the Georgia Tech Research Institute. First, electron-beam evaporation was used to coat a thin-film of CeO₂ on both sides of various Cu foils and meshes, as shown in Figure 65. TiO₂ nanorods were then grown by GLAD on one of the Cu foils (Top Left) in order to create a thin-film heterostructure composed of both CeO₂ and TiO₂. The remaining CeO₂-coated Cu substrates (both mesh and foil) were used for various experiments involving P25 TiO₂ deposited by solution techniques.

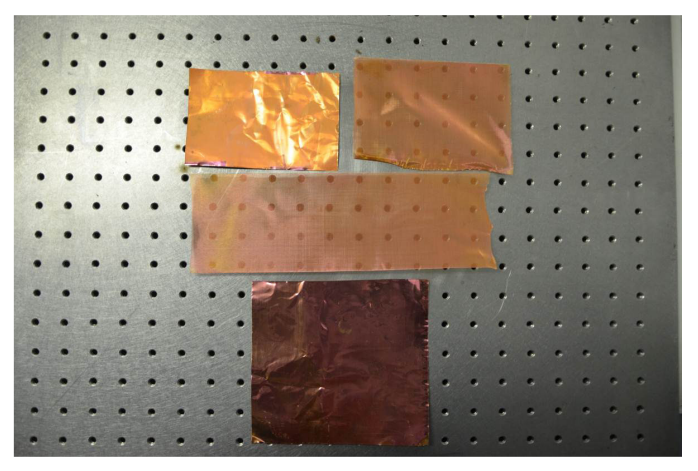


Figure 65. (Top Left) A 3x5 inch Cu foil with 200 nm CeO₂ coated followed by TiO₂ nano-columns; (Top Right & Middle) 100 nm CeO₂ film coated on front- and back-side of Cu mesh; (Bottom) 100 nm CeO₂ film coated on Cu foil. All samples were coated by GLAD.

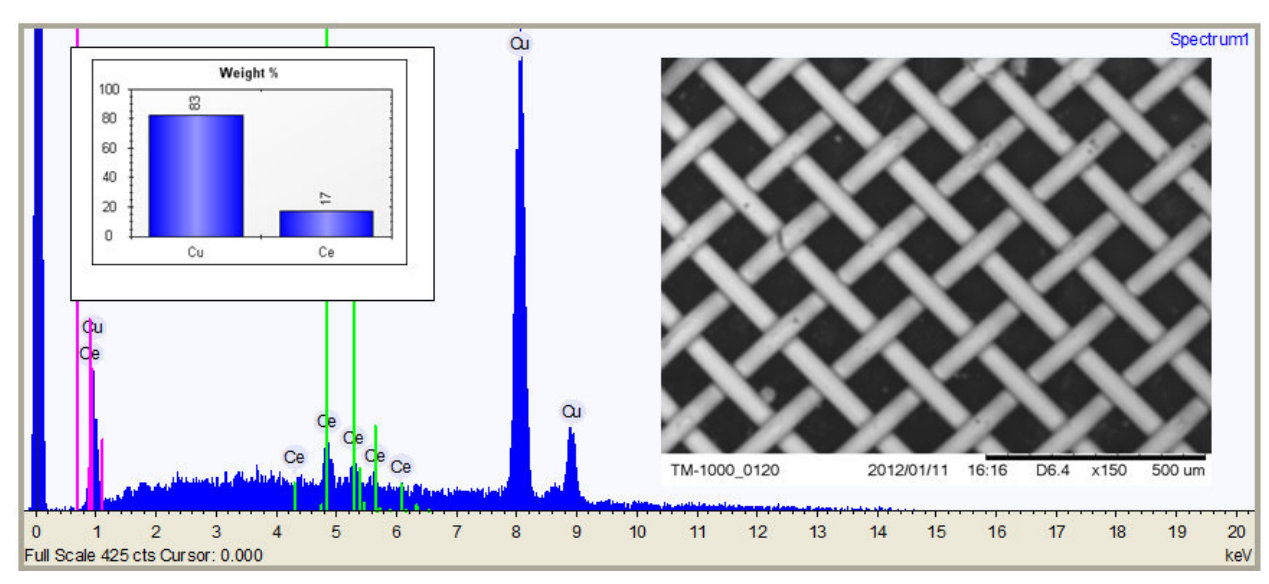


Figure 66. (Left) EDS data of CeO₂-coated Cu mesh using electron-beam evaporation. (Right) SEM image of coated mesh

Figure 66 (Left) and (Right) show Energy-dispersive X-ray Spectroscopy (EDS) data and Scanning Electron Microscope (SEM) images of the CeO₂ coated Cu mesh substrate. The presence of Ce could easily be confirmed by the EDS data. Figure 67 shows similar EDS data and an SEM image for a CeO₂-coated Cu foil.

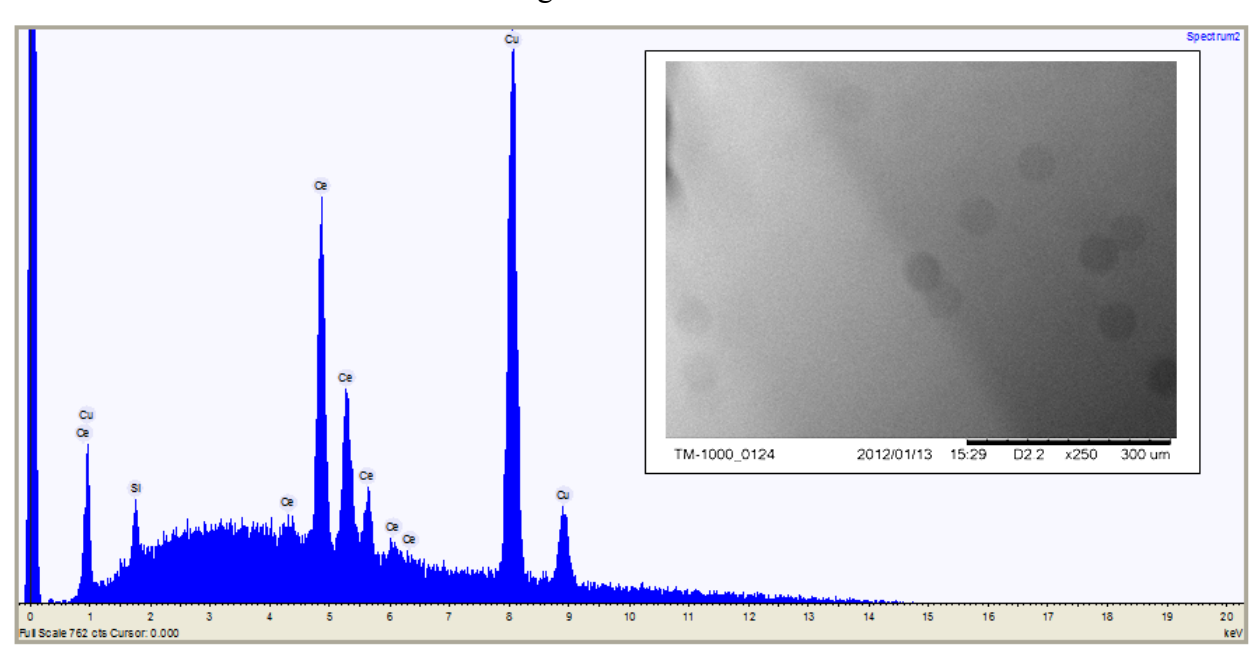


Figure 67, EDS data of CeO₂-coated Cu foil using electron-beam evaporation. (Right) SEM image of the coated foil showing the interface between the un-coated and coated areas.

Figure 68 shows EDS data and SEM image (bottom right) of a Cu foil coated with an initial thin-film layer of CeO₂ followed by a layer of TiO₂ nanorods deposited by GLAD. The EDS data confirm the presence of both Ti and Ce and the SEM image shows the quality of the film and the absence of cracks and pinholes in the film.

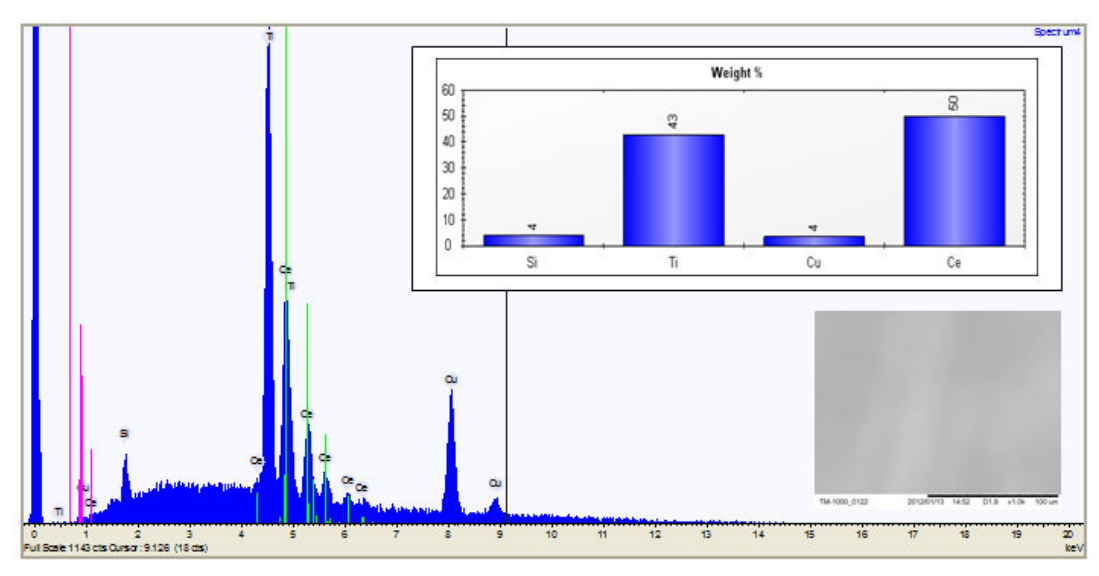
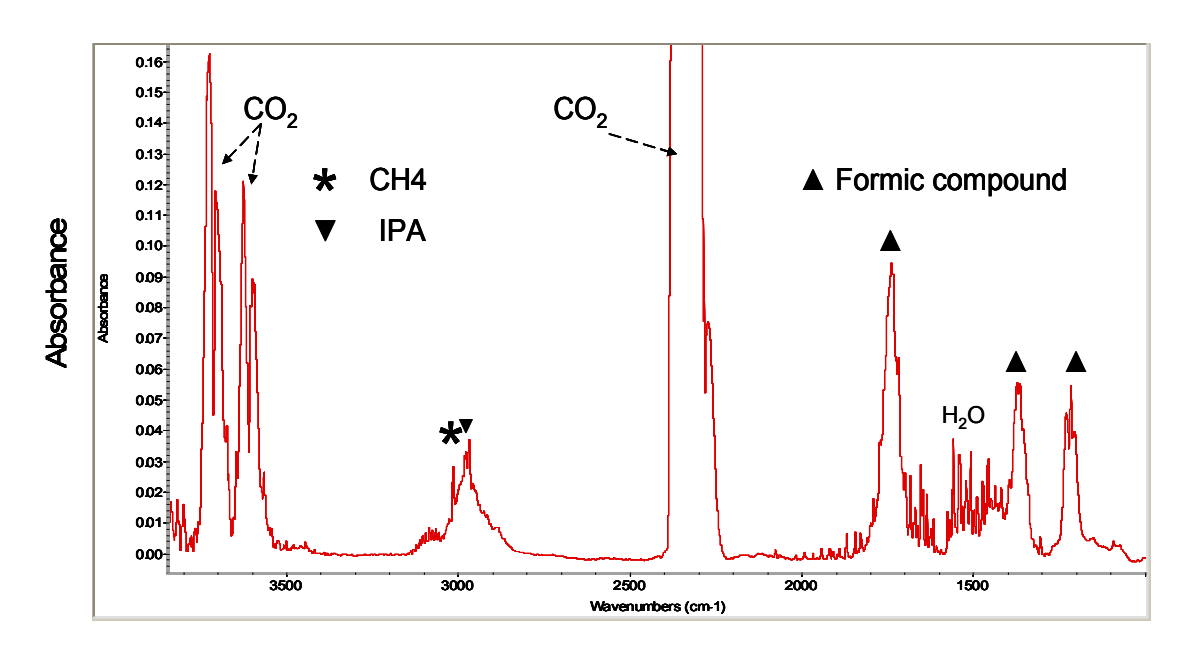


Figure 68. EDS data of CeO₂-TiO₂-coated Cu foil using electron-beam evaporation and GLAD. (Bottom Right) SEM image of the coated foil showing no cracks or pinholes in the thin-film layer.

These results together with Figure 42 present experimental confirmation on the validity of the modeling results shown earlier and offer evidence that the stability against oxidation of the CeO₂-coated copper substrates (b) is significantly enhanced compared to the uncoated copper (a).

4.2 Investigation of Alternative Structures

We've also evaluated the potential of new structures for reforming CO₂ into other hydrocarbons and found that formic acid can also produce in the Al/TiO₂ system. FTIR analysis of the gas composition following 17.5 hours of UV radiation showed some new activity between 1200-1800 cm⁻¹, corresponding to formic acid. In order to further improve the photocatalytic reduction reaction of CO₂, we injected 25 µL IPA hole scavenger into the reactor containing Al/TiO₂ mesh system. From Figure 69, it can be found that, following additional 68.5 hours of UV radiation, the peak of formic compounds is significantly enhanced, which suggested that the amount of formic acid produced continues to increase under UV radiation. At the same time, a small amount of methane is also produced (at about 3000 cm⁻¹), which suggests that the pathway of CO₂ to CH₄ reforming reaction in water may first involve the formation of formic acid, parts of which is then converted into methane.



Wavenumbers (cm⁻¹)

Figure 69 FTIR spectrum of gas composition in the photocatalytic reactor with 1.25g anatase titania on aluminum mesh (7×6.8 inches) following 68.5 hours of UVA irradiation from a 6W bulb.

We found that the aluminum mesh as a substrate to support titania seems to have a low photocatalytic activity for converting CO₂ and water into formic acid. Although the titania-aluminum structure could be further optimized to improve its photocatalytic activity, the development of alternative photocatalyst-metal structures continued to be investigated in order to determine the most efficient and robust structure that can be produced at the lowest-cost. Therefore, we also investigated another type of metal structures, specifically a stainless steel mesh, as a low-cost substrate to support titania photocatalysts for CO₂ reforming applications. Figure 70 shows the results of two types of titania powders attached on stainless steel cloth. After 17 or 18 hours of photocatalysis under UVA radiation, a sizable amount (~40 µl) of formic acid was produced inside the reactor. In addition, as shown in Figure 71, following the injecting of 25 µL of holeharvesting IPA into photocatalytic reactor, the concentration of CO₂ continues to decrease, while the concentration of formic acid is simultaneously enhanced to about 50 ul. Moreover, following the IPA injection, a small amount of methane can be observed after 27 hours of UVA radiation. Therefore, increasing the amount of hole scavengers inside the reactor enhances the production of both formic acid and methane from CO2 by photocatalysis.

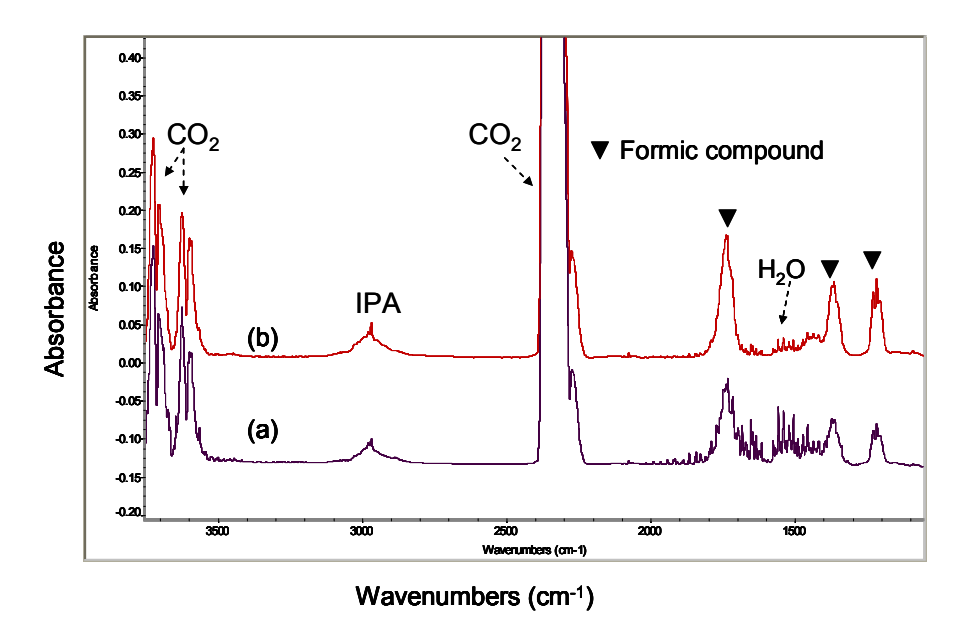


Figure 70. FTIR spectra of gas phase composition in the photocatalytic reactor with (a) 0.337g anatase titania on stainless steel via 17 hours of UVA radiation and (b) 0.352 g Degussa P25 titania on stainless steel via 18 hours of UVA radiation.

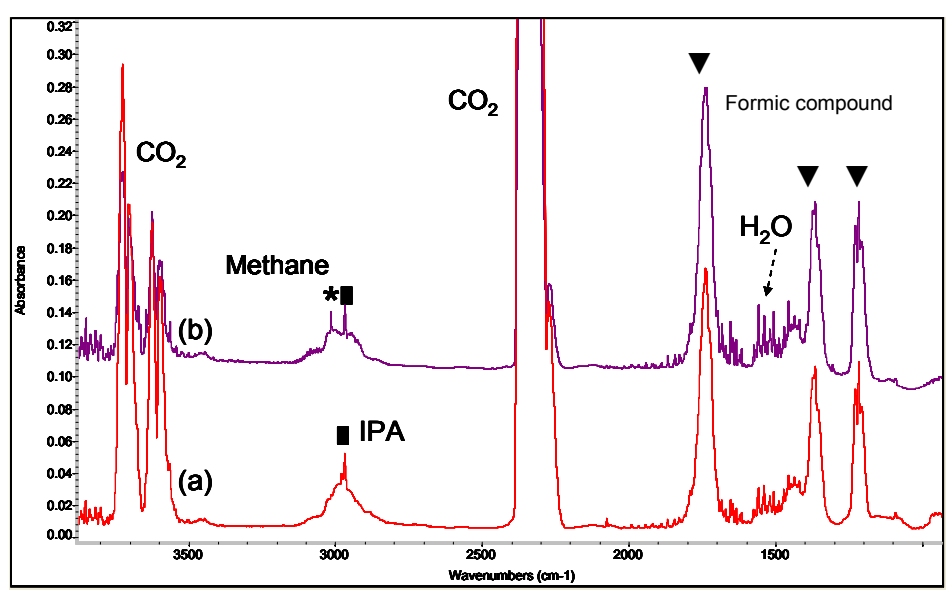


Figure 71. FTIR spectra of gas phase composition in the photocatalytic reactor with 0.352 g Degussa P25 titania attached on stainless steel ($2\times2.8\times5.8$ inches). (a) after 18 hours of UVA radiation and (b) after injecting 25 μ L IPA (99.5%) and continuing the reaction for another 27 hours under UVA radiation.

Moreover, we also investigated the photocatalytic reforming of CO_2 under sunlight radiation using the titania/stainless steel structure. The results were very promising and are shown in Figure 72 where formic acid peaks can be clearly seen after 6 hours of sunlight radiation.

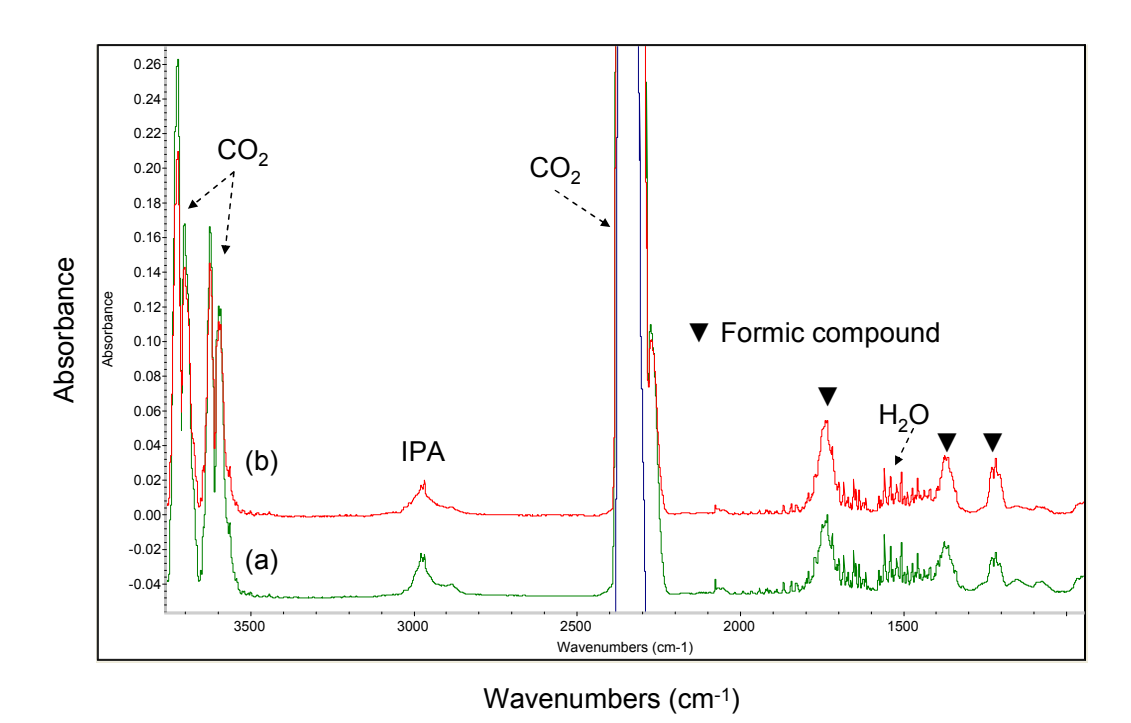


Figure 72. FTIR spectra of gas phase composition in the photocatalytic reactor containing 0.35 g Degussa P25 titania attached on stainless steel (2×2.8×5.8 inches). (a) after 6 hours of sunlight radiation and (b) after 12.5 hours of sunlight radiation. Average sunlight intensity at the wavelength of 400 nm: \sim 140 μ w/cm².

The above results combined with the low costs and high chemical stability of the various materials used in these experiment indicate that the titania/stainless steel structure has a great commercial potential for the development of large-scale photocatalytic reactor systems for the conversion of CO₂ and water into formic acid under sunlight conditions.

Since the photocatalytic process can produce holes and hydroxyl radicals, which can oxidize the metal substrate, we also investigated the photocatalytic activity of the titania-stainless steel system after oxidation.

Figure 73 shows the result of a reactor containing P25 titania-stainless steel alloy after calcination in air at 500° C in an oven. It was found that photocatalytic activity of this system, via oxidation processing, was similar to an identical system but without calcination. This result further confirms that the oxidation of the stainless steel type 316 alloy does not have a negative effect on the photocatalytic activity of a titania-stainless steel system. In fact, we believe that the formation of narrow-bandgap metal oxides such as NiO and Cr_2O_3 , as a result of stainless steel alloy oxidation, is beneficial for improving the visible-light driven photocatalytic activity.

_

¹ Type 316 stainless alloy contains 10-14% Ni and 16-18% Cr

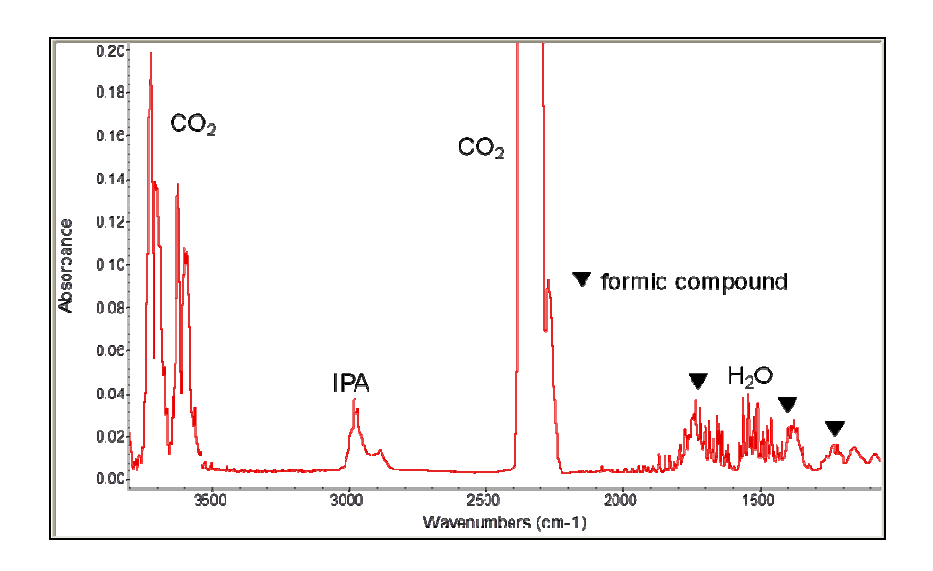


Figure 73. FTIR spectrum of gas phase composition in the photocatalytic reactor with titania-stainless steel mesh via 500 °C calcination, after 19 hours of visible light radiation.

In this project, we have also modified the conventional copper mesh substrate by e-beam deposition at Georgia Tech of 75nm nickel/chromium alloy on the surface of the copper substrate. The SEM & EDS analysis results of the modified copper mesh are shown in Figure 74, along with a photo of the coated copper mesh (bottom right).

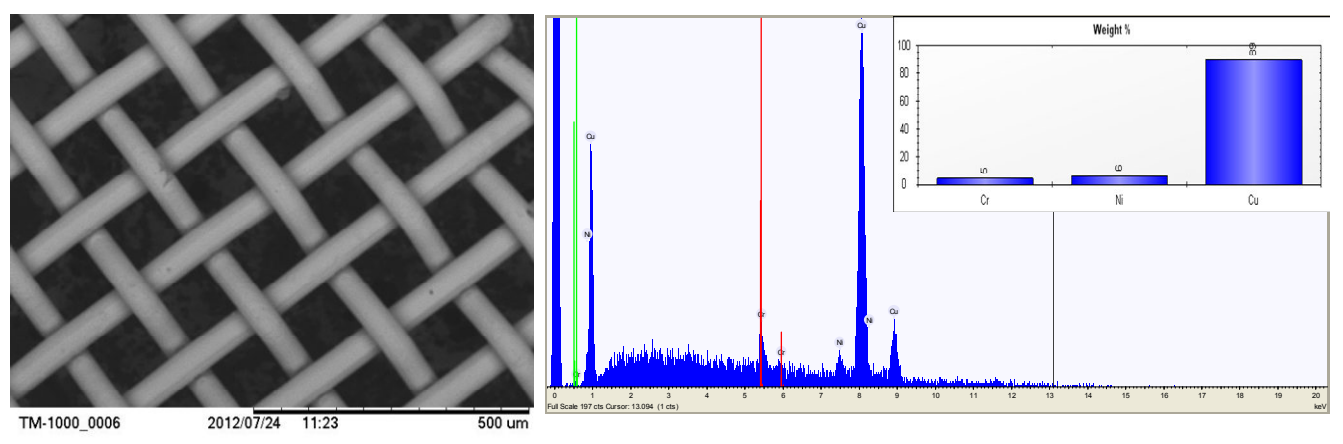


Figure 74. SEM & EDS analysis of copper mesh following e-beam deposition of 75nm nickel/chromium

The EDS results shown above (right) confirmed that there are 4.5% (weight percentage) chromium and 6.3 % (weight percentage) nickel on the modified copper surface.

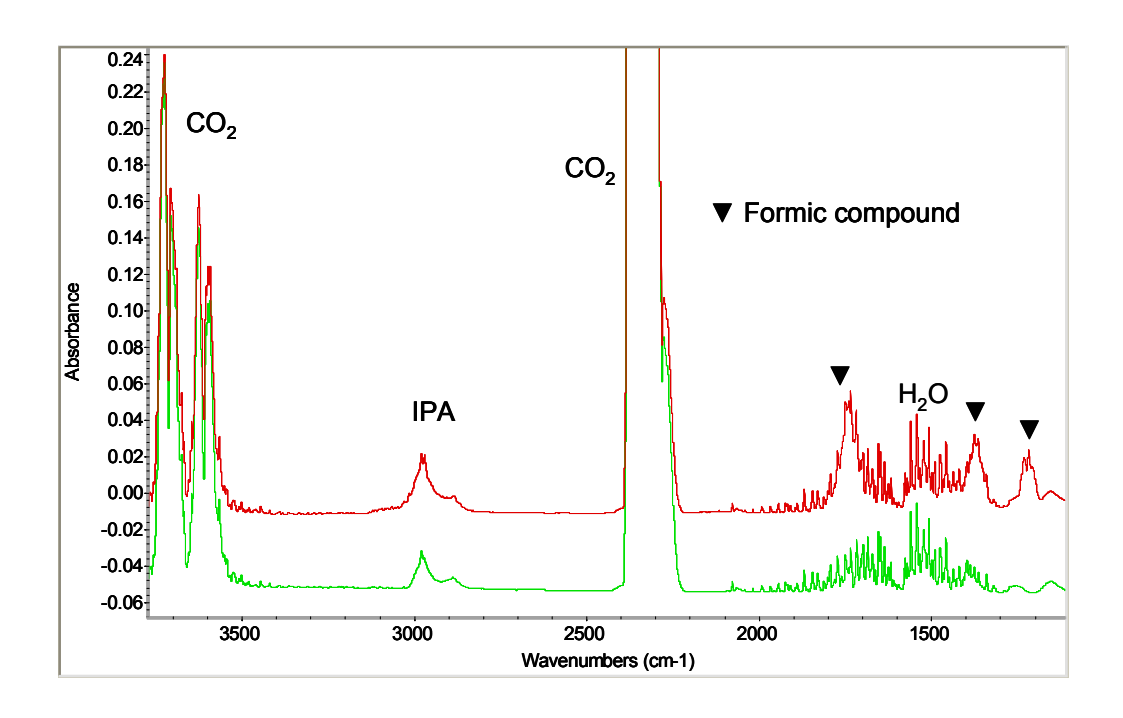


Figure 75. FTIR spectrum of gas phase composition in the photocatalytic reactor containing 0.0541g Degussa P25 titania powders immobilized on a nickel-chromium modified copper mesh with dimension of total 31.5 square inches, after 8 hours of sunlight radiation with average light intensity of 150 mW/cm².

Figure 75 shows the CO₂ reforming result from a photocatalytic reactor built with Degussa P25 titania-copper mesh with 75nm nickel/chromium layer. It was found that, after 8 hours of sunlight radiation, formic acid was produced from CO₂ and water in such a semiconductor-metal system. The energy efficiency of this photocatalytic system was only 0.013%.

Figure 76 shows the photocatalytic activity of a titania-Cu₂O-copper mesh based system. Formic acid was produced in this system after only 110 min of solar simulator radiation. Our former work had demonstrated that a titania-copper system can produce methane under solar simulator radiation. Considering that Cu₂O is a narrow band gap semiconductor, which can better utilize visible light, the formation of Cu₂O on the surface of the copper substrate may prove helpful in improving the selectivity of formic acid product from CO₂ and water under visible light irradiation.

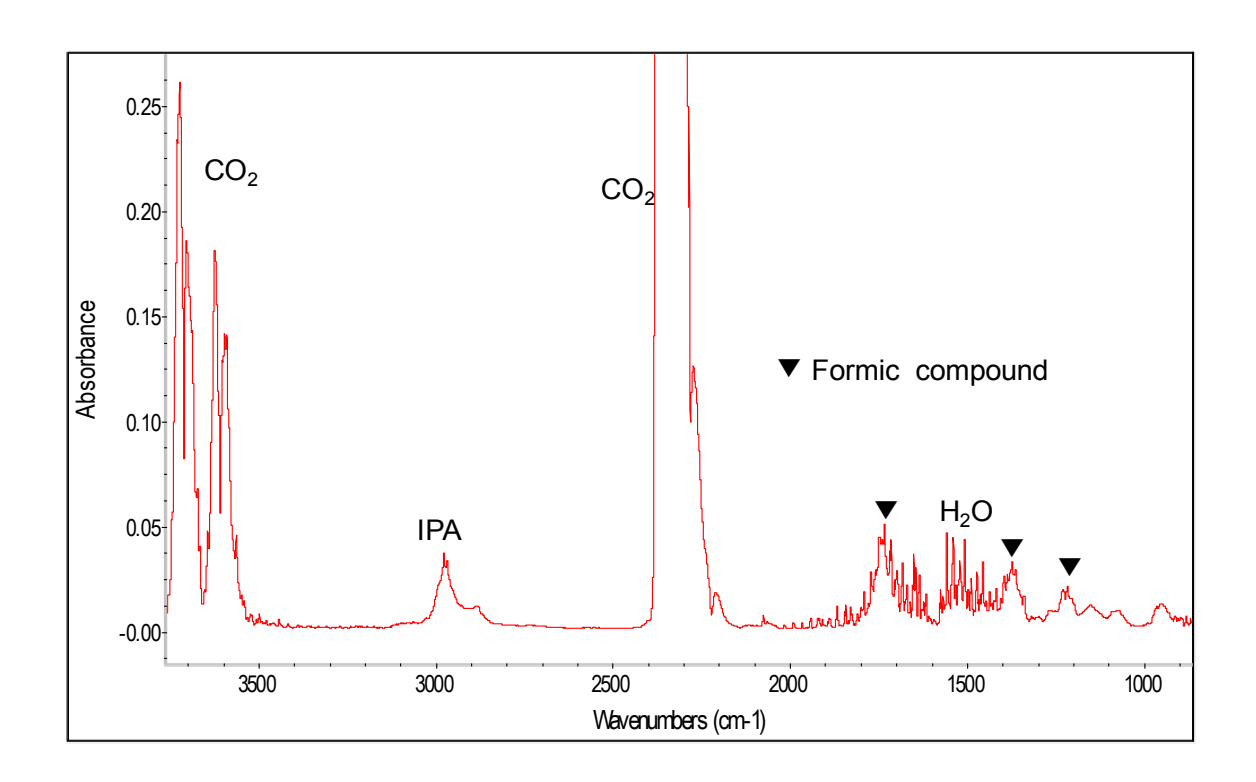
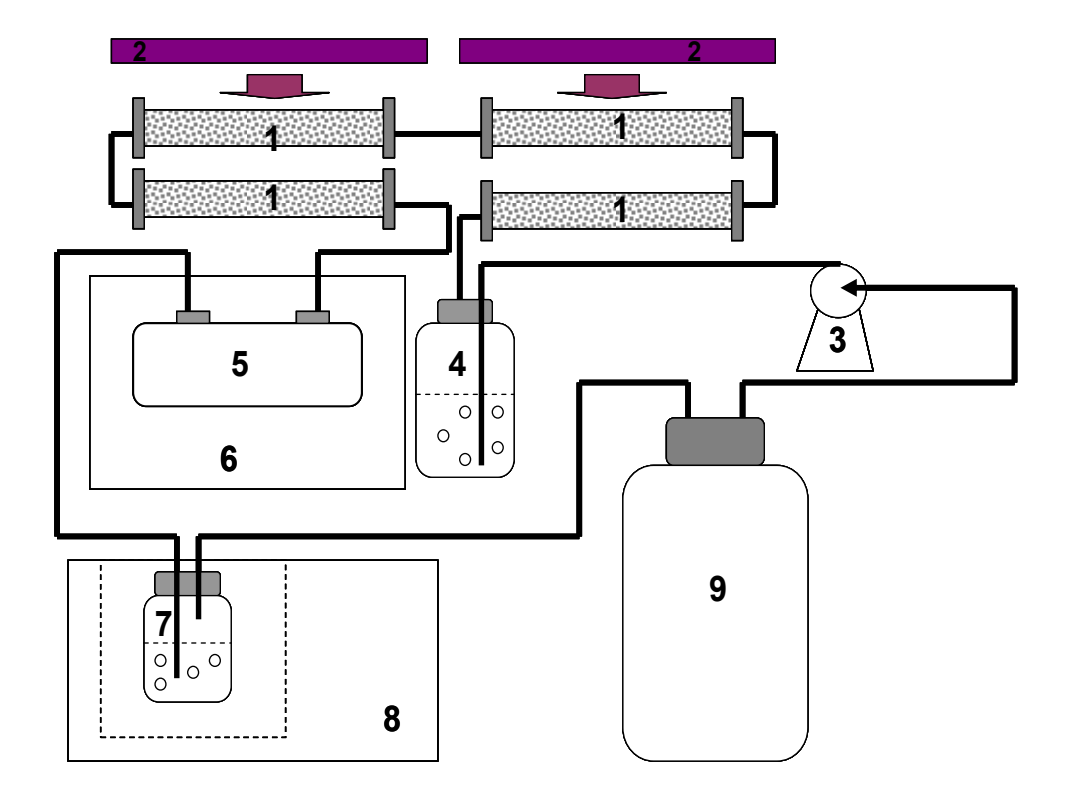


Figure 76. FTIR spectrum of gas phase composition in the photocatalytic reactor containing 0.2 g Degussa P25 titania powders attached on a Cu2O-copper fine mesh with dimension of 49 square inches, after 110 min of solar simulator radiation with average intensity of 200 mW/cm2.

Furthermore, in this project, we demonstrated a continuous and scalable fixed-bed photocatalytic reactor system and tested its long-term stability and photocatalytic activity for converting CO₂ and water into formic compounds. A diagram illustrating the experimental scheme is shown in Figure 77, which was built using Degussa P25 titania stainless steel structures since those were proven to be promising and stable semiconductor-metal structures for converting CO₂ and H₂O to formic acid. In this experiment, we've employed 4 separate small quartz reactors each having 15 ml of volume, and a total amount of P25 titania photocatalyst of 0.4g, which was attached on the stainless steel meshes with total dimension of 3×7 inches. Space velocity (SV) of such a system was about 9.1 hour⁻¹. As shown in Figure 77, CO₂ gas from storage tank 9 bubbles through tank 4, which contains 25% (volume ratio) IPA/H₂O solution. The vapors and CO₂ gas then travel through the irradiated reactors and the resulting composition is analyzed by the gas cell (#5) using the FTIR system (#6). The excess vapors are then collected into tank 7, which is placed inside a condensing unit apparatus with temperature of about -5 °C to trap most vapors. The remaining CO2 gas then continues and recycles back into the reactors for further reforming,



1. photocatalytic reactor with each 15 ml volume, 2. UV lamp with average intensity of ~ 8 mW/cm², 3. Tubing pump, 4. Tank containing IPA/H₂O solution, 5. FTIR quartz cell, 6.FTIR instrument 7. Excess vapor collection tank, 8. Cooling apparatus, 9. 2 Liter bottle containing CO₂ gas

Figure 77. Experimental scheme of the continuous fixed-bed photocatalytic reactor system

The CO₂ photocatalytic reforming results obtained using the above setup are shown in Figure 78. This data demonstrates that a continuous reactor system can effectively convert CO₂ and H₂O into formic acid. The amount of formic acid produced within this highly stable and scalable photocatalytic reactor continuously increases, while the amount of CO₂ within the system continues to decrease. It appears from the shown reaction time data (Figure 79) that the system reaches steady state conditions in the first 2 hours followed by a constant reforming rate for the next 24 hrs. In fact, it was also confirmed that formic acid production continued to increase for over 48 hours of reaction time and that, as long as there is enough CO₂ gas inside the system, such a photocatalytic reactor can continue to effectively convert CO₂ gas and water vapors into formic acid.

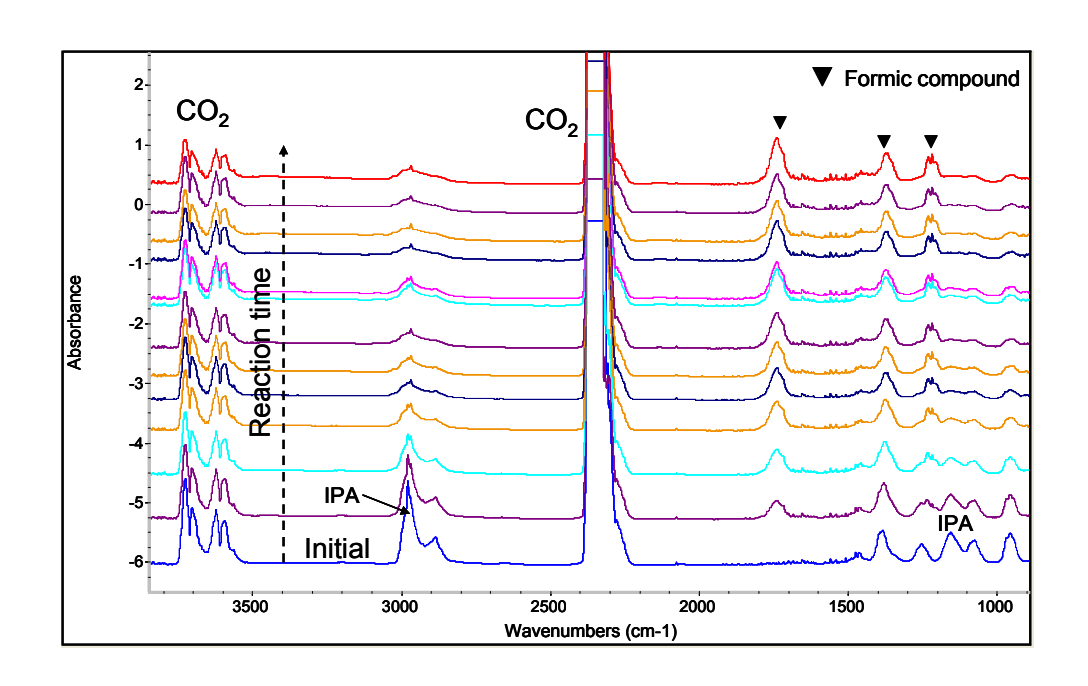


Figure 78. FTIR spectra of gas phase composition in a continuous photocatalytic reactor system under UVA radiation with average intensity of ~8 mW/cm²

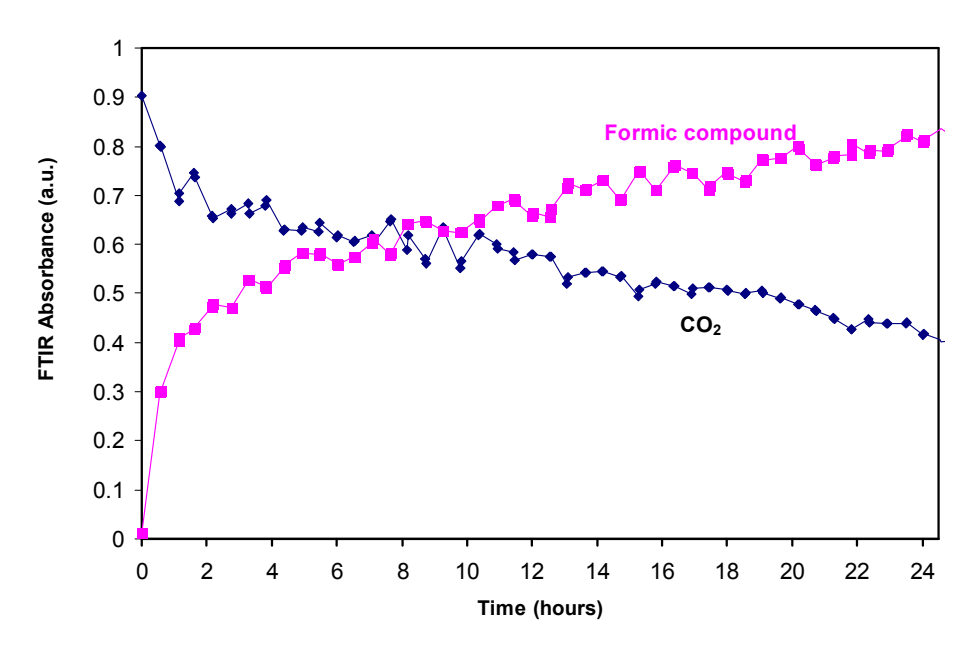
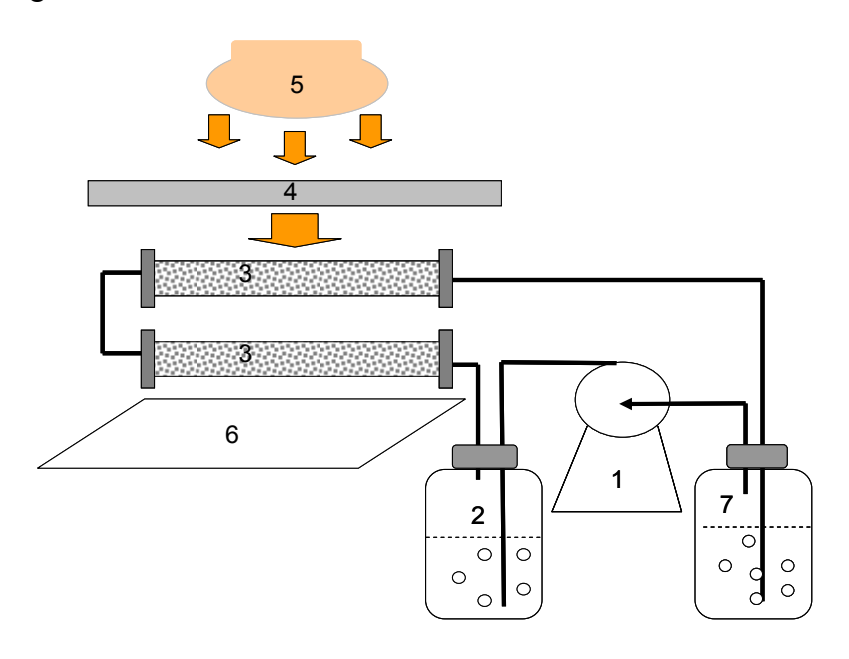


Figure 79. Time evolution of CO₂ and formic acid concentrations from reactor

Based on the objectives of this project, we demonstrated a continuous and scalable modular photocatalytic reactor system and tested its stability and photocatalytic activity for converting CO₂ and water into formic compounds under concentrated (using linear Fresnel lens) visible radiation from the Oriel solar simulator. A diagram illustrating the experimental scheme is shown in Figure 80, which was built using a titania-stainless alloy mesh modified by Ni and Cr metal nanostructures deposited at Ga Tech using the GLAD technique. In this experiment, we've employed 2 separate small quartz reactors

each having 15 ml of volume, and a total amount of P25 titania photocatalyst of 0.08g, which was attached on the modified stainless substrate with total dimension of 3×7 inches. Prior to solar light radiation, the system was circulated with pure CO₂ gas and purged for about 15 min. As shown in Figure 80, the vapors and CO₂ gas then travel through the irradiated reactors and the resulting composition is analyzed by FTIR following various time periods. The excess vapors are then collected into tank 7, which is placed inside a condensing unit apparatus with temperature of about -5 °C to trap most vapors. The remaining CO₂ gas then continues and recycles back into the reactors for further reforming.



1. Tubing pump, 2. Tank containing IPA/H₂O solution & CO₂ gas, 3. Photocatalytic reactors with 15 ml volume each, 4. Fresnel lens, 5. Solar simulator, 6. Reflector, 7. Excess vapor collection tank

Figure 80. Experimental scheme of the continuous modular photocatalytic reactor system with 9ml/min gas flow rate

The CO₂ photocatalytic reforming results obtained using the above setups are shown in Figure 81. This data demonstrates that a continuous modular reactor system can effectively convert CO₂ and H₂O into formic acid under solar radiation. After only 2.5 hours of photocatalytic reaction, formic compounds can be detected in both gas and liquid phase. In Figure 81, the FTIR spectrum labeled as "(b) gas phase" comes from a gas sample taken directly from within the photocatalytic reactor, while the FTIR spectrum labeled as "(a) liquid phase" comes from the liquid collected in collection tank 7. The relatively high photocatalytic activity of this system is attributed to the formation of green NiO (p-type) semiconductor, which has a narrow band gap capable of absorbing visible light.

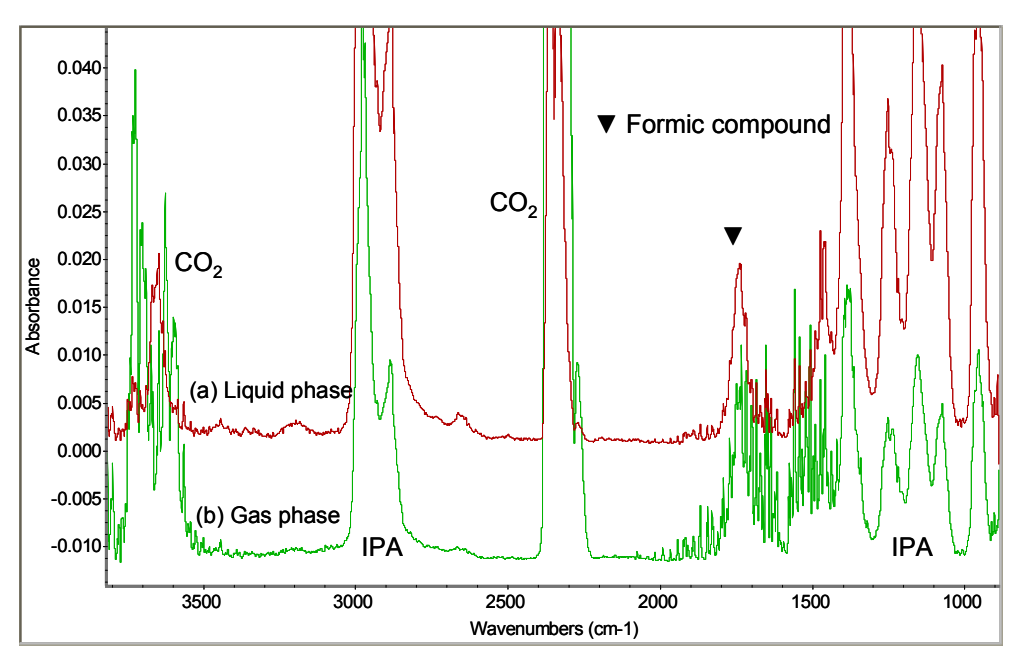
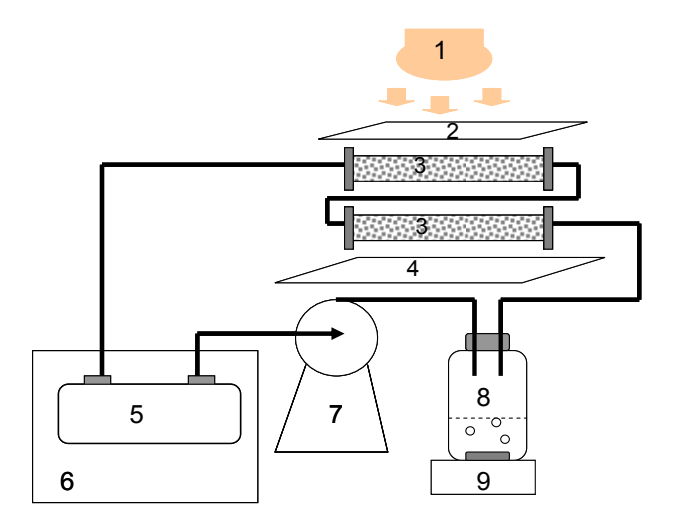


Figure 81. FTIR spectra of gas phase composition in a continuous photocatalytic reactor system with 0.08g Degussa titania-stainless steel modified by Ni and Cr metal nanostructures. After 2.5 hours of concentrated solar simulator radiation with light intensity of ~150 mW/cm2.

In addition, we built and demonstrated a continuous photocatalytic reactor system using a titania-stainless structure modified by Cr&Ni nanostructures (via a post heat treatment process (at 500°C) and tested its photocatalytic activity for converting CO₂ and water into formic compounds under concentrated (using linear Fresnel lens) visible radiation from an Oriel solar simulator. A diagram illustrating the experimental scheme is shown in Figure 82. Prior to solar light radiation, the system was circulated with pure CO₂ gas and purged for about 30 minutes. As shown in Figure 82, the vapors and CO₂ gas then travel through the irradiated reactors and the resulting composition is analyzed by FTIR following various time periods. The excess vapors are then circulated into tank 8, which is placed on a magnetic stirrer in order to maintain constant gas vapor pressure and mixture throughout the system. The gas mixture then continues and recycles back into the reactors for further reforming.



1. Solar simulator, 2. Fresnel lens, 3. Photocatalytic reactor tubes with 15 ml volume, 4. Reflector, 5. FTIR cell, 6. FTIR instrument, 7. Tubing pump, 8. Solution

Figure 82. Experimental scheme of the continuous modular photocatalytic reactor system containing titania-stainless steel mesh modified by Cr&Ni nanostructures, which had been oxidized in the oven with 500 °C. The flow rate of gas is 9 ml/min.

The FTIR data of the photocatalytic reforming results obtained using the above setup is shown in Figure 83. Figure 84 shows the evolution of the CO₂ and formic acid absorbance peaks as a function of reaction time for the first 350 minutes. This data demonstrates that a continuous modular reactor system can effectively and quickly convert CO₂ into formic acid under concentrated solar light. After about 4 hours, virtually all of the CO₂ gas is gone and the formation of formic acid begins to reach a plateau, as illustrated in Figure 84.

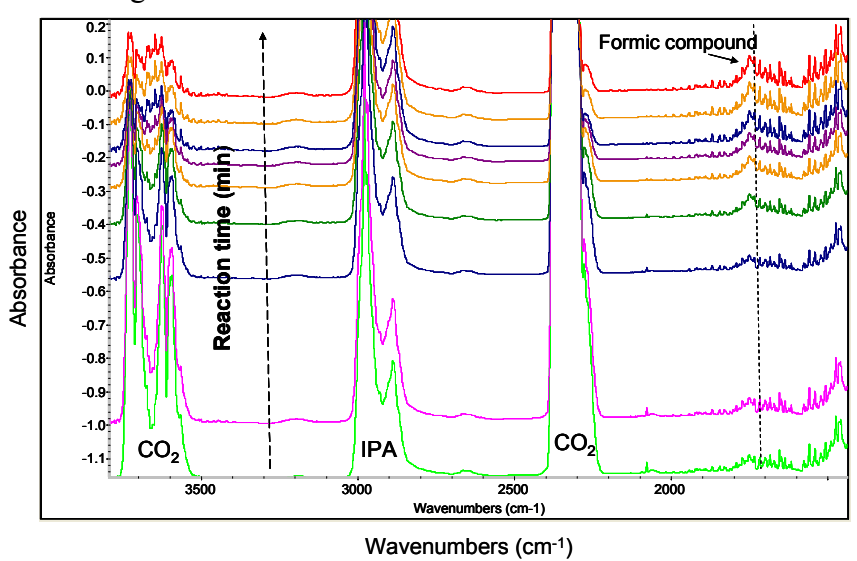


Figure 83. FTIR spectra of gas phase composition in a continuous photocatalytic reactor system under solar simulator light radiation with intensity of 300-400 mW/cm².

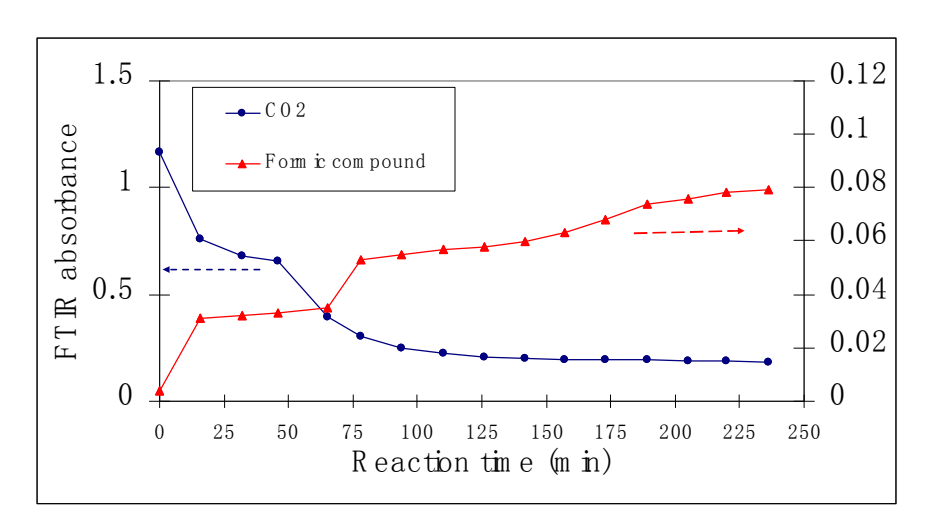


Figure 84. FTIR absorbance of CO_2 and formic compound as a function of reaction time using a continuous modular photocatalytic reactor system under solar simulator light radiation with intensity of 300-400 mW/cm².

During the third year of this project, we've explored and demonstrated the use of whey acid (unprocessed raw material) as a hole scavenger or sacrificial agent inside several different CO₂ photocatalytic reactors, and under both artificial light and natural solar radiation. We observed extremely quick reforming of CO₂ into several fuels and chemicals without adding any other artificial chemicals or water. Acid whey, an environmentally toxic and widely available by-product of the dairy industry, was used as the only agent in the reaction.

According to recently published reports, 150 million gallons of acid whey are produced annually by the US Northeast alone. Whey acid composition is toxic to the natural environment, robbing oxygen from streams and rivers and destroying aquatic life over potentially large areas. According to the same reports, dairy producers are so desperate to get rid of the whey, they pay farmers to take it off their hands and use it in fertilizers. ²

Acid whey seems to be an ideal organic feedstock for solar-based CO₂ reactors, not just because of its virtually zero cost and wide abundance worldwide, but also since it naturally contains 93-94% water and, therefore, eliminates the need for a supplementary water source. We have been able to confirm these extraordinary results and achieve repeatable performance using UV light (Figure 85), natural sunlight (Figure 86), as well as simulated sunlight (Figure 87). There are still many unexplained observations such as an unprecedented 50% drop in CO₂ levels in under 3 hours and several yet unidentified intermediate and final products. In addition to the usual formic acid (CH₂O₂) compound,

³http://www.medicaldaily.com/articles/15876/20130524/greek-yogurt-toxic-waste-yogurt-byproduct-whey-acid-water-pollution.htm

² http://modernfarmer.com/2013/05/whey-too-much-greek-yogurts-dark-side/

we have so far identified the presence of methanol (CH₄O), methane (CH₄), formaldehyde (CH₂O), and carbon monoxide (CO). Considering only formic acid, our low-end estimate of energy efficiency (EE) is currently at around 0.4%, which is 2X higher than the best EE achieved to date using isopropyl alcohol (previous sacrificial agent) and 16X higher than our originally proposed target. Once all other products are accounted for and our FTIR detection system is calibrated for the new chemicals, we anticipate the total EE will be much higher and might even exceed the photosynthetic efficiency of typical crop and biofuel plants (1-3%).

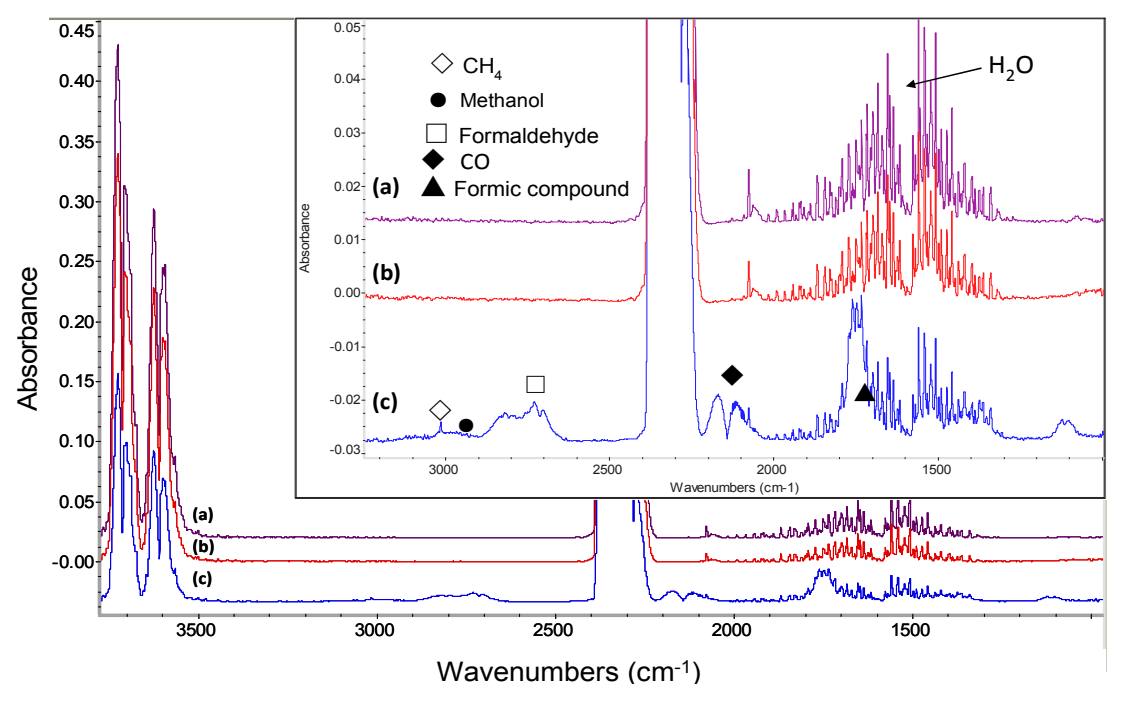


Figure 85. FTIR spectra of gas phase composition in the photocatalytic reactor (batch reactor mode, 40 ml) containing 0.1 g titania attached on stainless steel alloy (3×7 inches) and 3 ml whey acid solution. Temperature: ~30 °C, UV light radiation with average light intensity of ~8 mW/cm². (a) Initial, (b) 1 hr adsorbance (without UV radiation), and (c) after 69 hours of UV radiation.

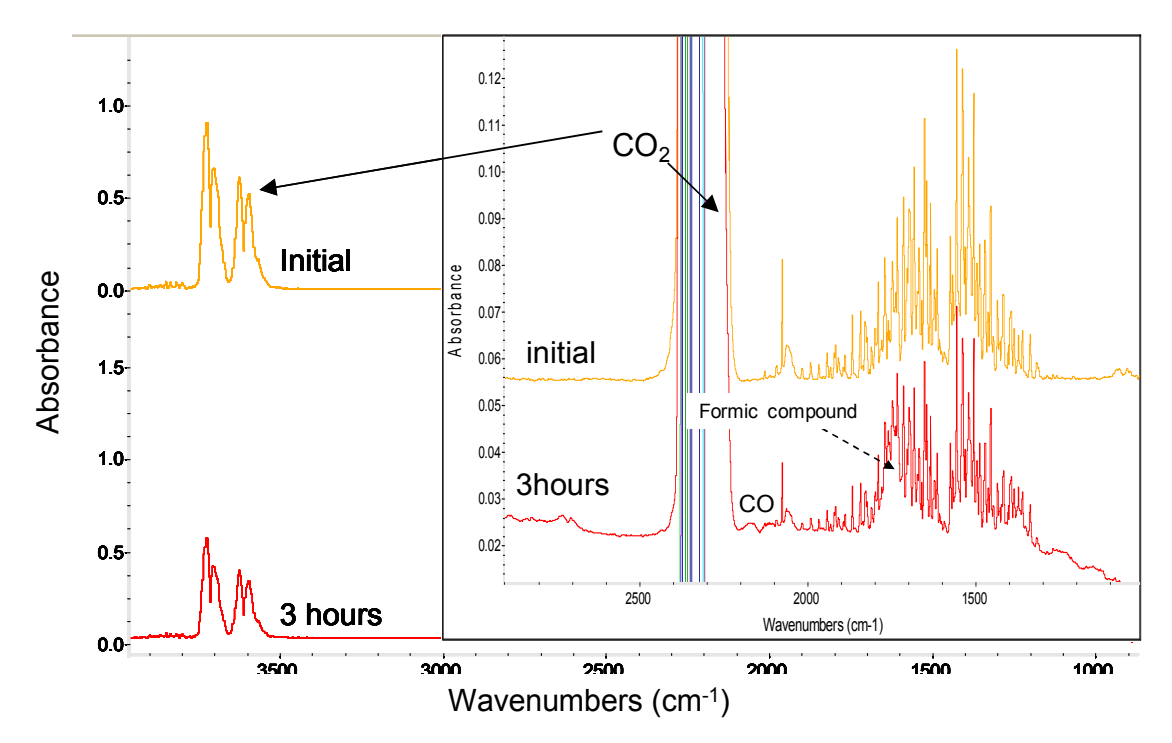


Figure 86. FTIR spectra of gas phase composition in the photocatalytic reactor (batch reactor mode) containing 0.1 g titania attached on the stainless steel alloy and 3 ml whey acid solution. Temperature: ~ 40 °C, natural sunlight radiation with average light intensity of ~ 100 mW/cm².

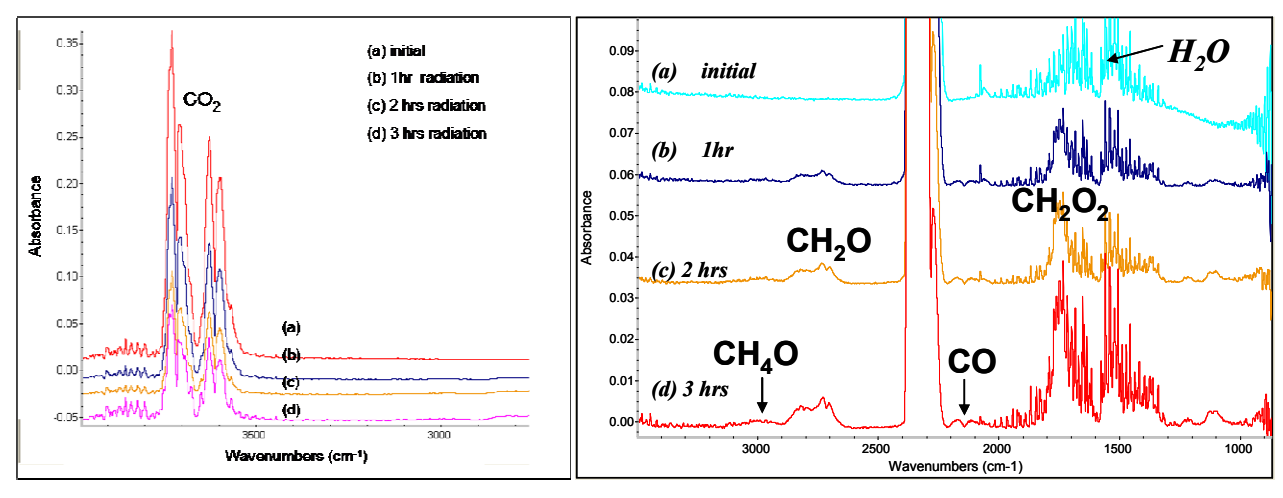


Figure 87. FTIR spectra of gas phase composition in the photocatalytic reactor (batch reactor mode) containing 0.12 g titania attached on a stainless steel alloy (3×7 inches) and 3 ml whey acid solution (94% $\rm H_2O$). Temperature: ~ 60 $\rm ^{o}C$, solar simulator radiation with average light intensity of ~350 mW/cm². (a) Initial, (b) 1 hr radiation, (c) 2 hrs radiation, and (d) 3 hrs radiation.

Task 5.0 Build and Demonstrate CO₂ Reactor Prototype

In order to evaluate the energy efficiency of the titania-stainless steel mesh based photocatalytic system under sunlight radiation, we used 0.096 g of P25 titania immobilized on a stainless steel mesh with total 95 sq inches into a 45 ml glass photocatalytic reactor, which was placed outdoors and radiated by sunlight with an average 120 mW/cm² sunlight intensity. The result was shown in Figure 88 The energy efficiency (only considering formic acid) of such a photocatalytic system reached 0.015%, which is 3X that (0.005%) reported by Nishimura¹⁵.

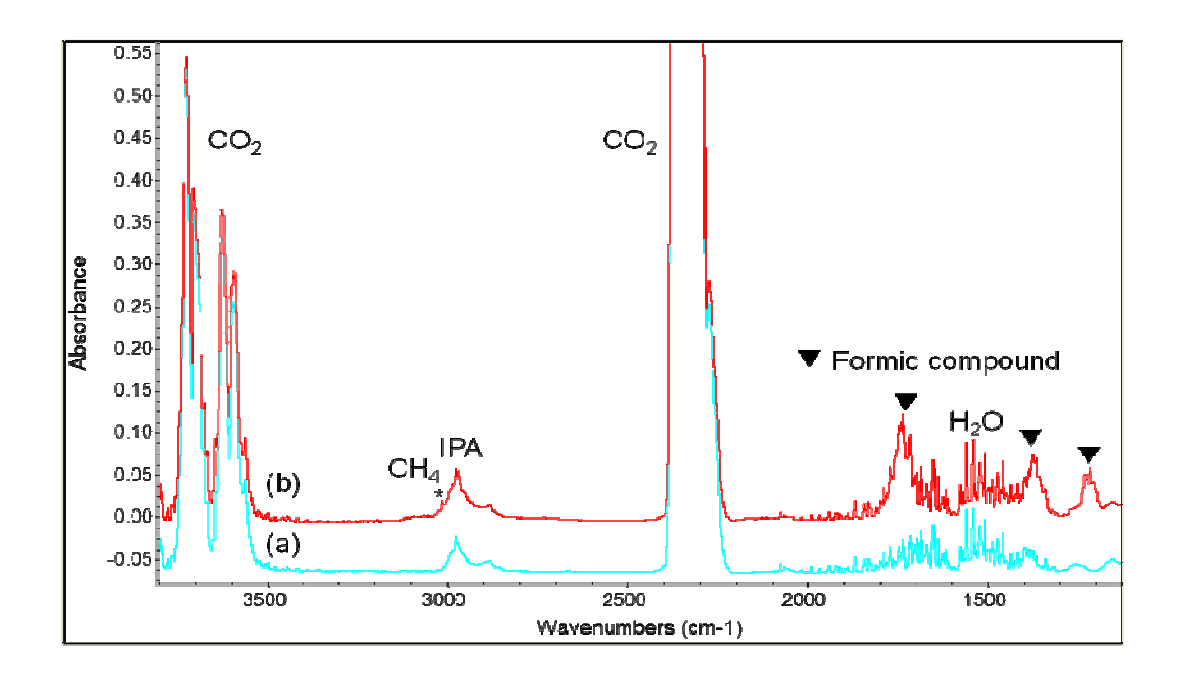


Figure 88. Top: FTIR spectra of gas phase composition in the photocatalytic reactor containing 0.096g Degussa P25 titania powders immobilized on used stainless steel meshes with dimension of total 95 square inches under sunlight radiation with average light intensity of 120 mW/cm2. (a) initial and (b) after 2 hours.

In addition, we built the first radiator-style fixed-bed photocatalytic reactor system (Figure 90) for larger-scale demonstration of CO₂ reforming into formic acid and methane by sunlight.

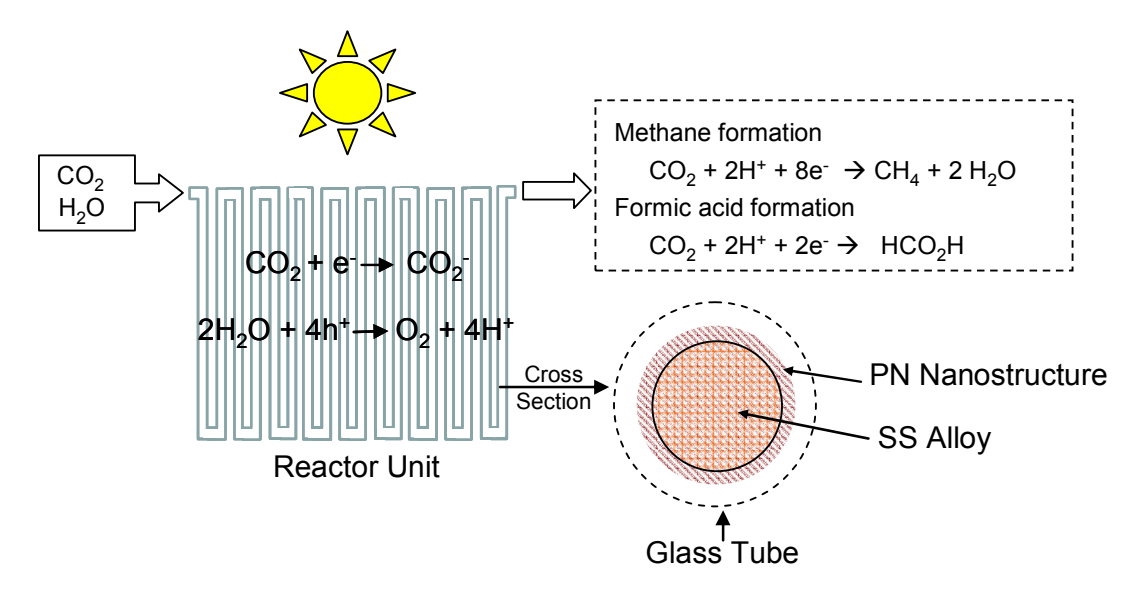


Figure 89. Design of CO₂ reforming reactor prototype previously reported in Q7



Figure 90. Photos of actual CO₂ reforming reactor prototype built using PN nanostructure on stable stainless steel substrates

Quartz glass was used in the construction of the reactor units due to the quartz superior optical transmission for both UV and visible sunlight radiation. The length of each photocatalytic unit shown above is 14.75 inch with an inner diameter of around 0.438 inch. There was 0.13g Degussa P25 titania nanoparticles used in each tube and the dimension of the stainless steel substrates placed in each unit was 14×0.75 inch.

Figure 91 shows the result of photocatalytic conversion of CO₂ and water into formic acid in the prototype reactor units under sunlight radiation. We tested the module for functionality in a continuous one-pass experiment using a low gas flow rate. Even in such a configuration, which was made using only 10 units in series, formic acid was detected from the reactor following 4 hours of photocatalysis under sunlight radiation. This suggests that a one-pass configuration can potentially be used as a flue gas reforming reactor, assuming the modules can be built large enough and with significantly higher number of reactor units in order to generate large volumes of formic acid from CO₂. Gas separation membranes and trapping modules can also be used jointly with such a

configuration to isolate the desired product(s) and recycle excess CO₂ back into the reactor.

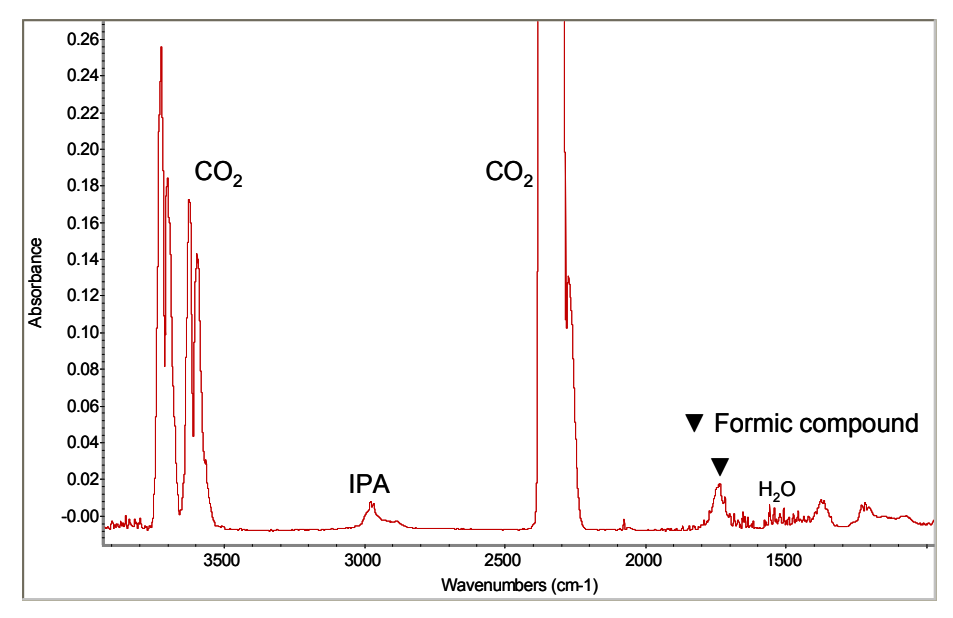


Figure 91. FTIR spectrum of gas phase composition in continuous photocatalytic units. The length of each tube in the photocatalytic units is 14.75 inch and the tube inner diameter is 0.438 inch. After 4 hours of sunlight radiation with light intensity of \sim 70 mW/cm2, temperature \sim 15 °C.

We've also investigated the effectiveness of the modular photocatalytic reactor system for CO₂ reforming using gas feedstock containing lower concentrations of CO₂ gas in order to simulate conditions comparable to flue gas sources. Critical for the potential commercialization of the modular photocatalytic reactor system is its capability for solar-driven photocatalytic reforming of CO₂ gas from various greenhouse-contributing industrial emission sources (e.g., flue gas), which have CO₂ concentrations in the 10-15 % range.

Figure 92 shows a comparative FTIR absorbance results for the photocatalytic conversion of CO₂ to formic compound (batch reactor mode) with both high (66.7%) and low (33.4%) initial CO₂ concentrations. Each reactor contained 2 ml aqueous solution (IPA:H₂O=7.5:100 (v/v)). As expected, the reactor containing lower initial CO₂ concentration resulted in a lower formic compound yield. However, after only 2 hours of solar light radiation, the FTIR absorbance peaks for formic acid could still be observed. Such a result suggested that the current titania-stainless steel alloy structure exhibits good photocatalytic activity, even at relatively lower concentrations of CO₂.

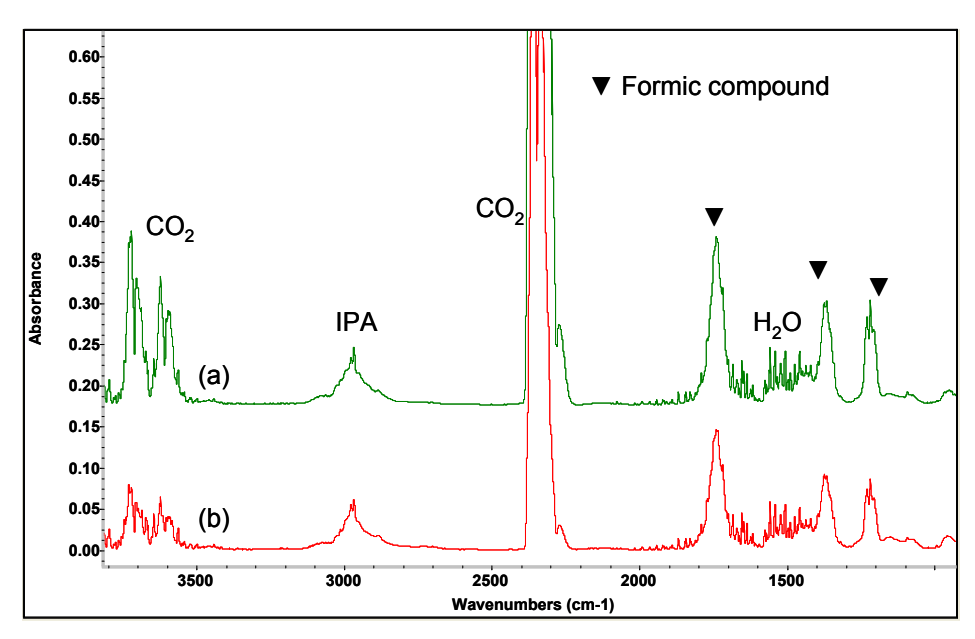
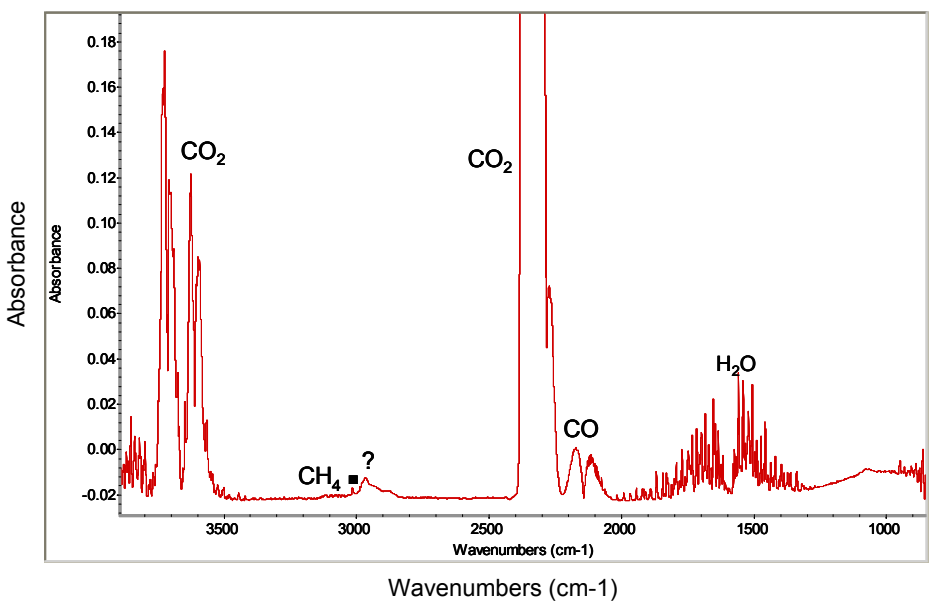


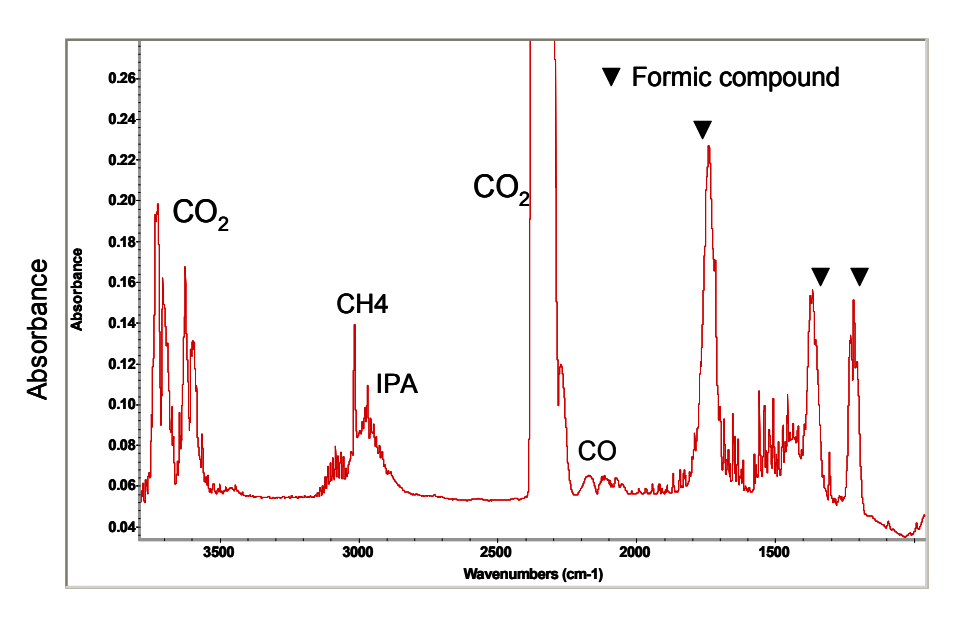
Figure 92. FTIR spectra of gas phase composition in the photocatalytic reactors (batch reactor mode) containing titania-stainless steel structures and a) high (66.7%) initial CO_2 concentration and (b) low (33.4%) initial CO_2 concentration. Reaction time: 2hr, reaction temperature: 63°C, solar simulator radiation with average light intensity of ~150 mW/cm².

In order to test this structure at CO₂ levels close to those of flue gas compositions, we analyzed the gas mixture obtained from a typical internal combustion engine after it was cleaned by the catalytic converter system (car exhaust gas). Figure 93 shows the FTIR spectrum of car exhaust gas, which in fact was partially diluted by air. It can be observed that, in addition to CO₂, some CO and even some methane was detected. The analysis showed that the FTIR absorbance peak of CO₂ at the wavenumbers of 3625 cm⁻¹ is 0.198, which corresponds to 13% CO₂ concentration. Therefore, this gas mixture was confirmed to have CO₂ concentration in the range of that of typical flue gas (i.e., 10-15%). In addition, the data in Figure 93 shows that the car exhaust gas contained about 1% CO, which is much higher than that contained in typical flue gas composition.



wavenumbers (cm-1)

Figure 93. FTIR spectrum of car exhaust gas (13% CO₂) mixed with air



Wavenumbers (cm⁻¹)

Figure 94. FTIR spectrum of gas phase composition in the photocatalytic reactor containing 0.3g titania attached on stainless steel mesh with dimensions of 3×7 inches (batch reactor mode), after 24 hours of UV light radiation with light intensity of 2.5 mW/cm².

Figure 94 shows the result of the photocatalytic conversion of CO_2 from car exhaust gas using a titania-stainless system under UV radiation. Both methane and formic acid were produced, with both CO_2 and CO levels dropping, indicating that both gases were contributing to the reactions. Similar results were also obtained from the reactor under sunlight radiation, as shown in Figure 95 and Figure 96. The results in Figure 96 indicate that formic acid can be produced after only 1 hour of sunlight radiation inside a reactor with low (20-25% initial CO_2 concentration).

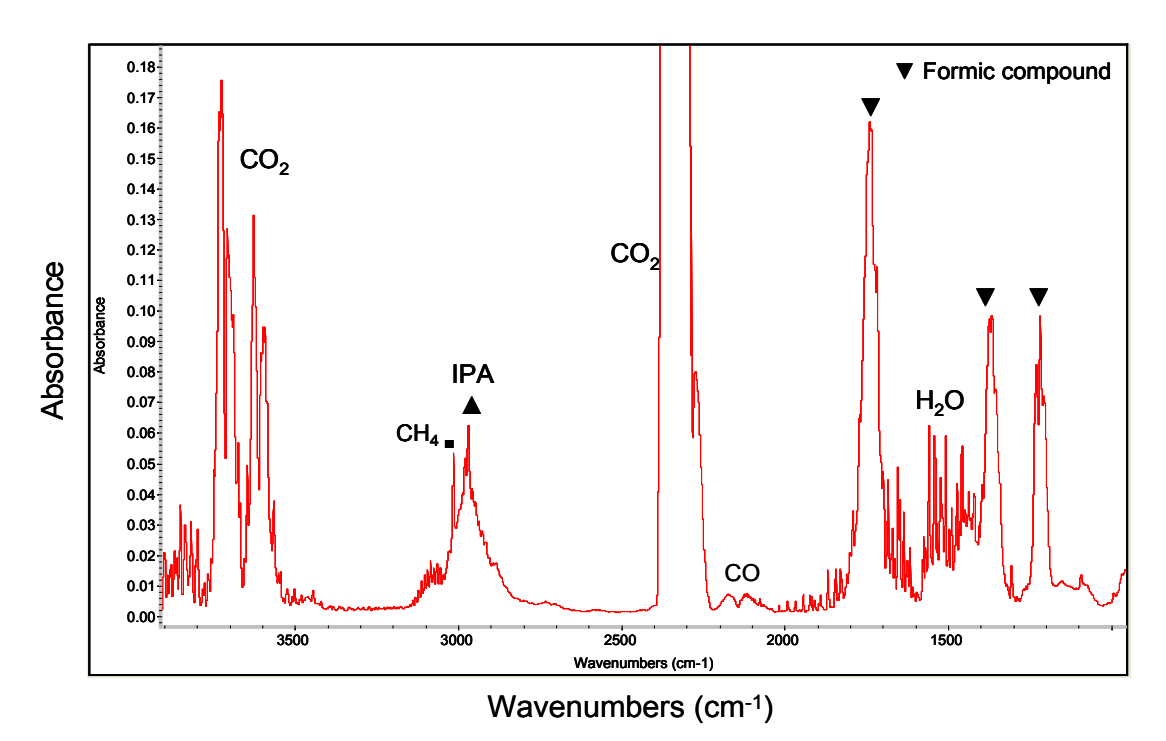


Figure 95. FTIR spectrum of gas phase composition in the reactor containing 0.3g titania attached on stainless steel structure with dimensions of 3×7 inches (batch reactor mode), after 4 hours of sunlight radiation in a cloudy weather. CO_2 from car exhaust gas was used in this experiment.

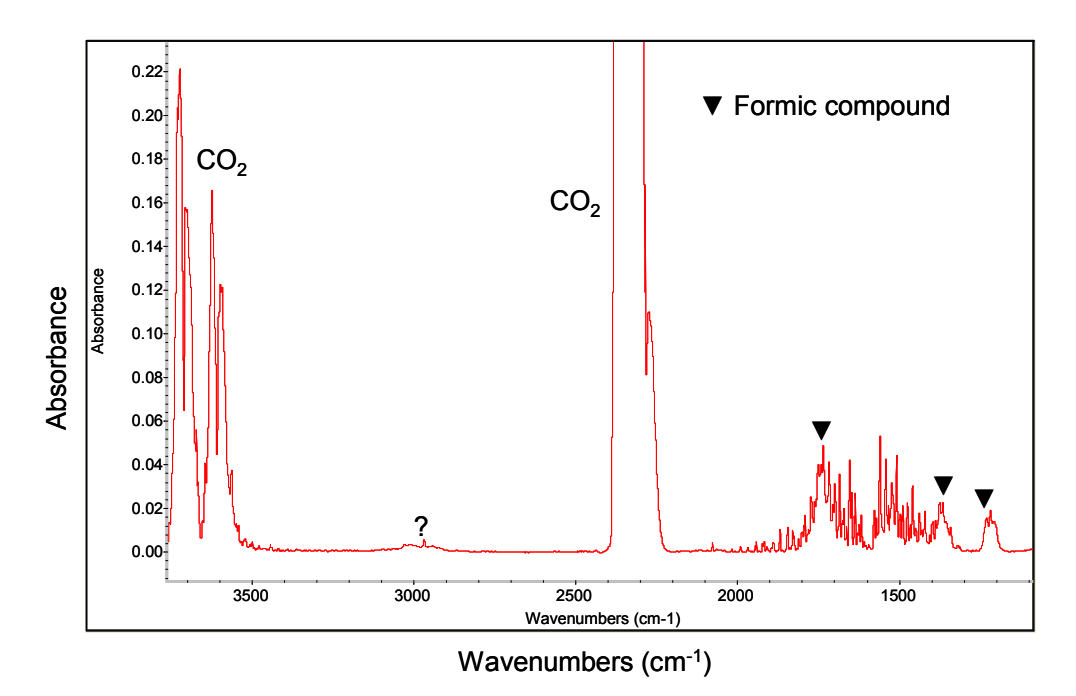


Figure 96. FTIR spectrum of gas phase composition in a photocatalytic unit with about 20-25% initial concentration of CO_2 (continuous circulation of reactor mode), after 1 hour of sunlight radiation with light intensity of ~100 mW/cm2. The flow rate of gas was 9 ml/min.

We've continued the optimization of the radiator-style fixed-bed photocatalytic reactor system for pilot-scale demonstration of CO₂ reforming by sunlight. One of the important operation parameters of the photocatalytic reactor system shown above is the flow rate of the CO₂ gas. In this project, we investigated the effect of higher gas flow rates, so as to achieve better yield of formic compound. High flow rates of CO₂ and water vapors improve the mass transfer of the corresponding molecules to the surface of the photocatalytic coating. For these experiments, the pilot scale photocatalytic unit was operated in a circulation flow mode (closed system) without continuously introducing CO₂, water, or a sacrificial agent. Figure 97 shows the result of CO₂ reforming using such a mode following 1 hour of sunlight exposure. Prior to sunlight radiation, the reactor unit was flushed with low concentration (about 25%) of CO₂ gas mixed with small amount of CO (collected from automobile exhaust gas), as well as IPA (hole scavenger) & water vapor mix. It was found that after only 1 hour under sunlight radiation, formic acid was detected along with small amounts of methanol and carbon monoxide, and with virtually no traces of IPA left inside the reactor.

In addition, we've investigated the photocatalytic performance of the pilot scale reactor unit using a relatively constant supply of CO₂ gas bubbling into an IPA/water (1:2) source under direct sunlight and high circulation flow rate (closed system). The FTIR results are shown in Figure 98. Following only 1 hour of operation under sunlight radiation, large amounts of formic acid was detected, indicating that fast reforming of CO₂ can be achieved under high circulation flow rates, if CO₂, water, and a sacrificial agent are continuously being introduced into the system.

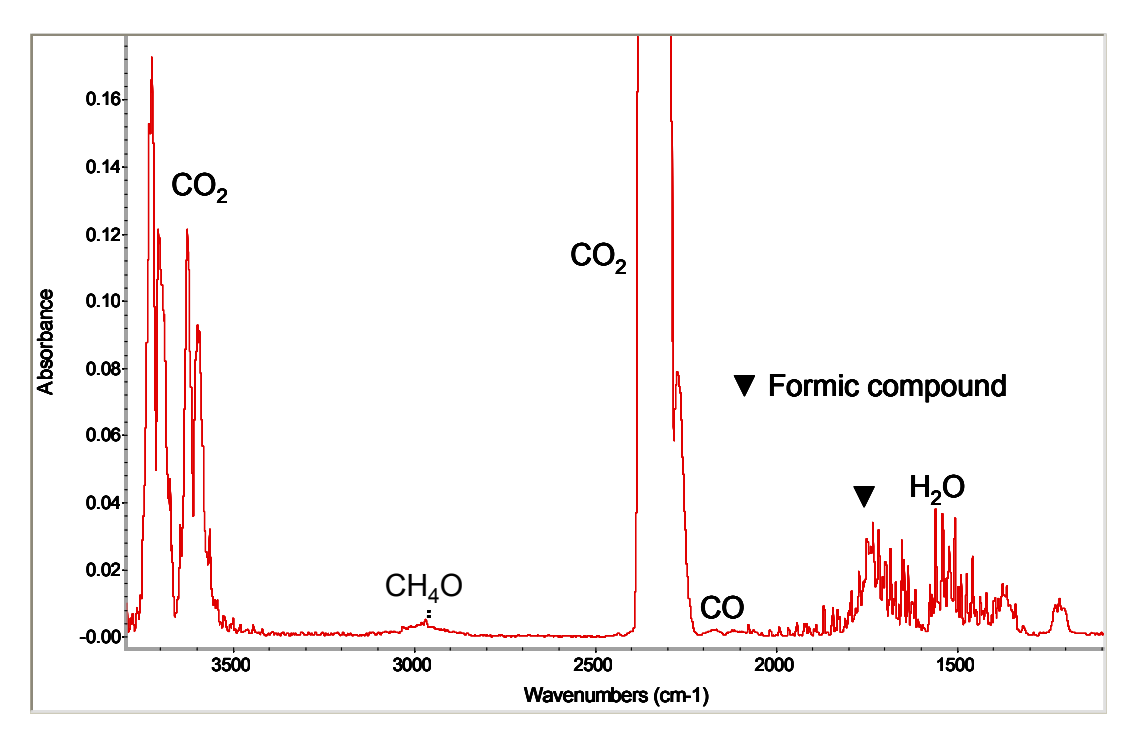


Figure 97. FTIR spectrum of gas phase composition in the pilot photocatalytic reactor in closed circulation mode using a flow rate of ~27 ml/min, following 1 hour of sunlight radiation with average light intensity of ~120 mW/cm². Temperature: 45° C. In this case, fixed amounts of CO_2 gas and $IPA:H_2O$ solution (1:2) are pre-loaded into the reactor.

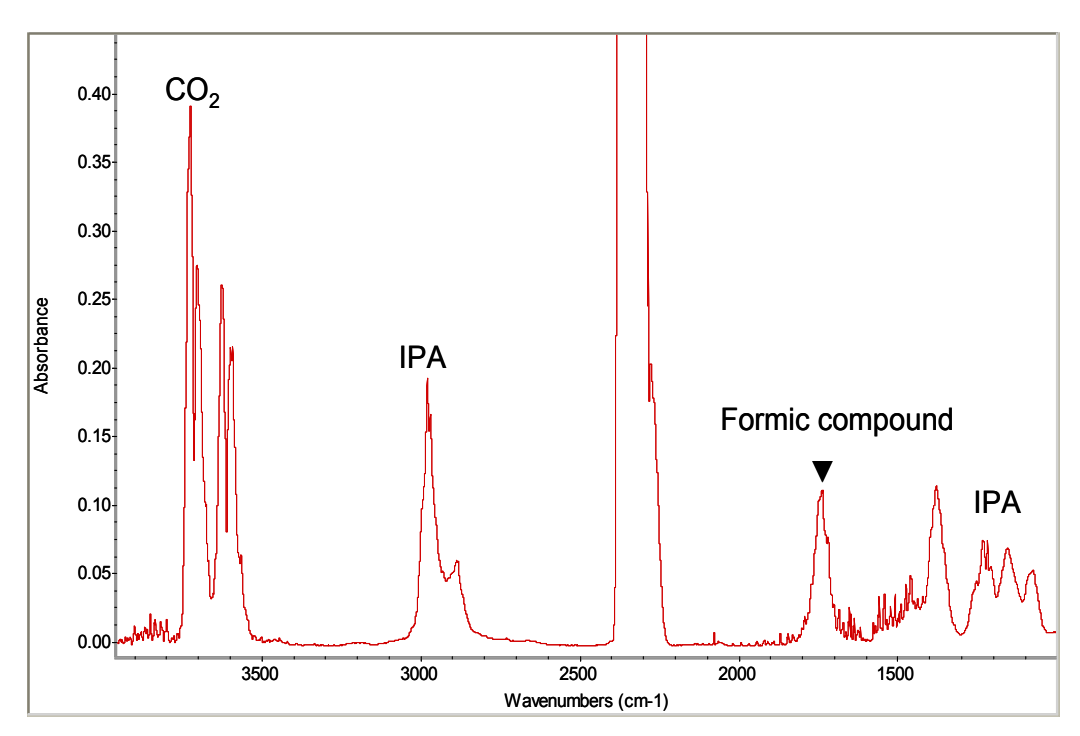


Figure 98. FTIR spectrum of gas phase composition inside the pilot photocatalytic reactor in continuous circulation mode using a flow rate of \sim 27 ml/min, following 1 hour of sunlight radiation with light intensity of \sim 150 mW/cm². Temperature: 45°C. In this case, a 2 L container of CO₂ gas is continuously bubbling into an IPA solution (IPA: H2O=1:2 (v/v))

Furthermore, we've evaluated the photocatalytic performance of the pilot reactor unit in a one-pass reactor mode (open system) under sunlight radiation. Despite the fact that the produced gas products were continuously being removed by the high CO₂ gas flow rates, formic acid was still detected inside the reactor in under 1 hour. Figure 99 illustrates the results of CO₂ reforming using the one-pass flow mode (at 0.1 ml/min, open system). The FTIR spectrum after 2 hours of sunlight operation shows a relatively strong formic acid absorbance peak (0.1). Based on these results, we can conclude that both types of reactor mode operation (closed circulation and open one-pass) are feasible, as long as the operation parameters are optimized for each mode.

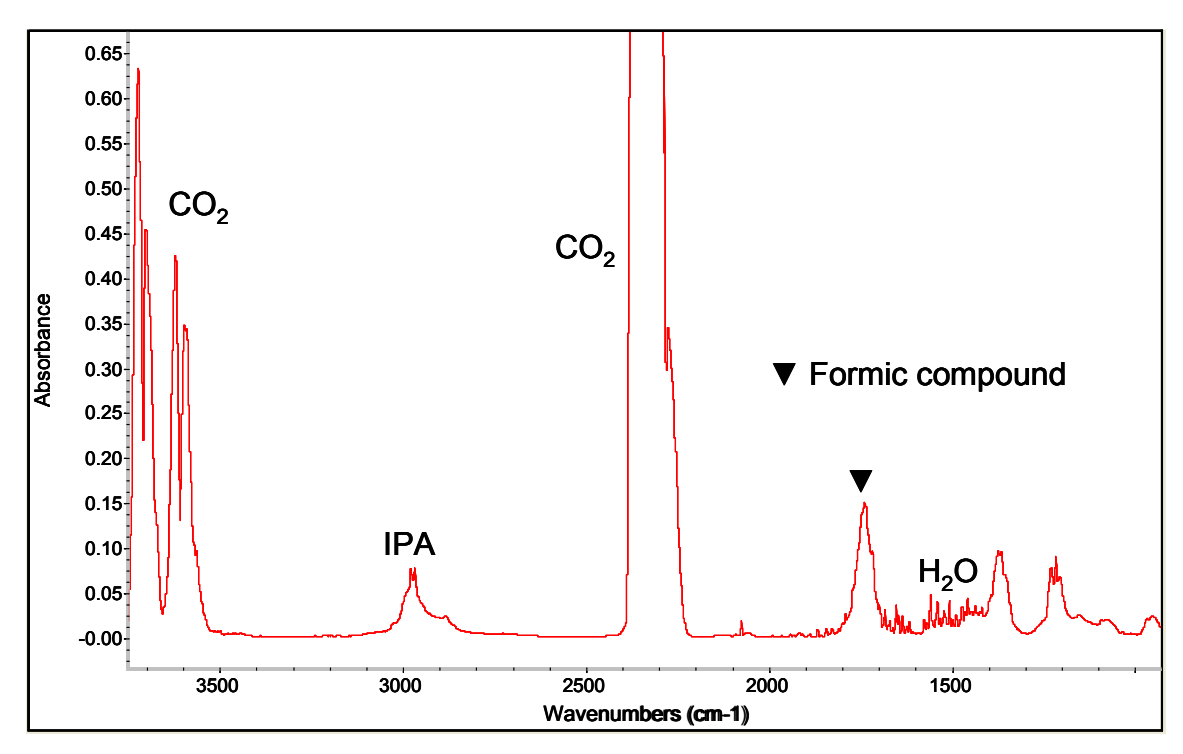


Figure 99. FTIR spectrum of gas phase composition inside the pilot scale photocatalytic units with gas flow rate of 0.1 ml/min (one-pass reactor mode), after 2 hours of sunlight radiation with average light intensity of \sim 100 mW/cm², temperature: 35 °C.

List of Significant Accomplishments

- Completed all project milestones planned to-date & updated project management plan
- Nanorods of narrow-bandgap materials synthesized with absorption up to 600nm
- TiO₂ nanorods successfully grown on Ti substrates by electrochemical deposition
- New semiconductor metal oxide PN structure exhibited significant absorption of visible light and near-infrared
- Achieved the highest reported CO₂ to CH₄ reforming yields (382 uL/h.g-catalyst) using TiO₂/Ti reactor and sunlight. (compared to 280 uL/h.g reported in 2010 using comparable system¹⁴)
- Achieved the highest reported CO₂ to CH₄ reforming yields (1823 uL/h.g-catalyst) using proprietary non-TiO₂ narrow-bandgap PN structure and sunlight. (no similar structure has ever been reported in the literature for CO₂ reforming)
- Nanorods and thin-films of narrow-bandgap materials synthesized with absorption up to 650nm
- Low-cost solution-based and thermal processes were successfully used to grow thinfilms (< 100nm) of highly reactive visible light photocatalyst structures
- Various wide-bandgap thin-films and nanorods were grown by Glancing Angle Deposition (GLAD) on metal substrates

- Demonstrated thin-film PN structure with average VIS/NIR light absorption at 27%
- Demonstrated improved optical and thermal performance from 3-dimensional narrow bandgap nanocrystal structures
- Demonstrated continuous CO₂ reforming into methane and formic acid for more than 7 days using a very stable TiO₂/Ti nanorod structure.
- Demonstrated techniques for enhanced oxidation resistance of copper substrates for photocatalytic applications.
- Demonstrated new metal-oxide PN structures for CO₂ reforming into formic acid (CH₂O₂) under sunlight conditions.
- Demonstrated stable stainless steel based structures for CO₂ reforming into formic acid (CH₂O₂) under sunlight conditions.
- Improved the CO₂ reforming properties of the stable stainless steel photocatalytic reforming structure by modifying the surface using metal alloy thin-films
- Built a continuous fixed-bed photocatalytic reactor system for a larger-scale demonstration of CO₂ reforming into formic acid
- Built & tested a continuous modular photocatalytic reactor system for CO₂ reforming into formic acid
- Demonstrated increased stability and oxidation resistance from surface-modified stainless-based photocatalytic structures
- Demonstrated a one-pass solar-based reforming of CO₂ into formic acid using modular reactor made of 10 units with a total length around 150 in and inner diameter less than 0.5in.
- Demonstrated an improved solar-activated titania-stainless photocatalytic structure modified using Cr/Ni nanostructures
- Demonstrated photocatalytic activity under both UV and sunlight using low concentrations of CO₂ gas comparable to that in flue gas compositions (10-15%)
- Demonstrated continuous CO₂ to formic acid reforming using a continuous modular photocatalytic reactor system under solar simulator light irradiation
- Demonstrated pilot-scale photocatalytic activity under sunlight using higher flow rates of CO₂ gas.
- Demonstrated fast CO₂ to formic acid reforming using both a continuous closedsystem circulating mode as well as a one-pass non-circulating mode under sunlight conditions.
- First time demonstration of fast CO₂ reforming into several fuels and chemicals under sunlight using environmentally toxic acid whey as a hole scavenger:
 - o 50% drop in CO₂ levels in under 3 hours was achieved inside closed reactor
 - Simultaneous production of formic acid, methanol, formaldehyde, methane, and carbon monoxide without any additional chemicals or water supply
- A presentation was made to the project manager at a project kick- off web meeting held on November 22nd, 2010.
- Publication/presentation accepted at the 242nd ACS conference in September 2011

- Delivered an invited presentation at the 2012 Energy Materials Nanotechnology Meeting in Orlando, FL, April 16-20, 2012.
- Invited to present at Heterogeneous Catalysis Symposium, ACS Philadelphia Meeting in August 2012.
- Accepted for poster presentation at the 17th International Conference on Semiconductor Photocatalysis and Solar Energy Conversion (SPASEC-17), Jacksonville, Florida, USA November 11-15, 2012.
- A new paper summarizing latest results is planned for publication early in 2014.

Conclusions & Future Roadmap

The extremely fast and unprecedented solar-based reforming of CO_2 achieved during this reporting period has demonstrated that acid whey is a highly effective hole scavenger for a photocatalytic reactor system. Even when accounting for formic acid alone, the relatively high energy efficiency (0.4%) achieved for this new system is 16X that of our original project goal and higher than anything ever reported for a solar-based photocatalytic reactor.

A comprehensive literature search has revealed no prior work related to using acid whey as a hole scavenger for CO₂ reforming by photocatalysis, indicating that this is a very novel discovery that has not yet been explored and should have the potential for significant improvements. All the optimization tasks completed to date in this project have focused on using the standard IPA (electronic grade) as a hole scavenger and our pilot solar reactor was designed and built for such a system. However, even if access to IPA in wastewater is realized (near a semiconductor manufacturing plant, for example), such an approach remains problematic due to its limited implementation potential and difficulties in accounting for any other organic wastes present that may be detrimental to the photocatalytic structure. On the other hand, the organic content and variability of an acid whey solution will always be known and no detrimental effects have been observed to date on any component of the photocatalytic reactor. Therefore, an optimized commercial scale solar reactor can be designed and built using such an approach and without requiring any other organics or a supplementary water source.

The optimization tasks performed over the past two years using our standard photocatalytic reactor have resulted in efficiency increase from an initial 0.02% to about 0.25% (12.5X). If a comparable increase in energy efficiency can be achieved using an acid whey photocatalytic reactor, then this would translate into energy efficiency around 5%, which would have immediate applications and would far exceed the photosynthetic energy efficiency of most crop and virtually all biofuel plants. Furthermore, a photocatalytic reactor based on this approach will be far more superior to biofuel technologies since it can be installed in any geographical region, including deserts, and does not require an arable land or continuous maintenance.

Given the limited time available for completion of this program, achieving such an

ambitious target will be far outside the scope of the current project. However, we believe such work is critical in order to achieve a truly transformational impact from this solar-based photocatalytic CO₂ reforming technology. Breaking the 5% energy efficiency threshold will be crucial for wide adoption of this technology in any industrial setting. We therefore recommend the following roadmap, which we believe could help achieve such target in next generation solar-based CO₂ photocatalytic reactors:

- Determine optimal acid whey levels inside photocatalytic reactor
- Investigate relationship between CO₂ flow rates and reforming yields
- Determine optimal water content of acid whey solution
- Investigate relationship between reactor temperature and reforming yields
- Investigate relationship between sunlight intensity and reforming yields
- Full characterization & analysis of intermediate and final products (solution & gas phase)
- Investigation of existing methods to separate and store produced chemicals and fuels
- Build and demonstrate pilot-scale photocatalytic reactor using acid whey
- Perform lifecycle analysis of the pilot-scale photocatalytic reactor based on acid whey
- Work with a major producer of acid whey waste to implement technology on-site

References

- 2 Ardalan, P; Brennan T.P; Lee, H; Bakke, J. R.; Ding, I.; McGehee, M. D.; Stacey F. Bent, S. F.; ACS Nano 2011, 5, 1495.
- 3 Talapin, D. V.; Nelson, J. H.; Shevchenko, E. V.; Aloni, S.; Bryce, S.; Alivisatos, A. P. Nano Lett. 2007, 7, 2951.
- 4 Varghese, O. K.; Paulose, M.; LaTempa, T. J.; Grimes, C. A. Nano Lett. 2009, 9, 731.
- 5 Tan, S. S.; Zou, L.; Hu, E. Sci. Technol. Ad. Mater. 2007, 9, 89.
- 6 Adachi, K.; Ohta, K.; Mizuna, T. Sol. Energy 1994, 53, 187.
- 7 Anpo, M.; Yamashita, H.; Ichihashi, Y.; Ehara, S. J. Electroanal. Chem. 1995, 396, 21.
- 8 Y. Chen, A. Thamban, M. T. Nguyen, H. Menkara. Highly Selective Photocatalytic Conversion of Carbon Dioxide and Water into Methane. Submitted for publication to the Division of Fuel Chemistry, 242nd ACS National Meeting, Denver, CO. Aug. 28 Sept. 1.2011.
- 9 Cyrus S. Rustomji, Christine J. Frandsen, Sungho Jin, and Michael J. Tauber. the Journal of Physical Chemistry B 2010 114 (45), 14537-14543.
- 10 Varghese, O. K.; Paulose, M.; LaTempa, T. J.; Grimes, C. A. Nano Lett. 2009, 9, 731.
- 11 Tan, S. S.; Zou, L.; Hu, E. Sci. Technol. Ad. Mater. 2007, 9, 89.
- 12 Adachi, K.; Ohta, K.; Mizuna, T. Sol. Energy 1994, 53, 187.
- 13 Anpo, M.; Yamashita, H.; Ichihashi, Y.; Ehara, S. J. Electroanal. Chem. 1995, 396, 21.
- 14 Somnath C. Roy, Oomman K. Varghese, Maggie Paulose, and Craig A. Grimes, "Toward Solar Fuels: Photocatalytic Conversion of Carbon Dioxide to Hydrocarbons", ACS Nano Review, VOL. 4, NO. 3, 1259–1278, 2010
- 15 A. Nishimura et al., "CO2 Reforming into Fuel using TiO2 Photocatalyst and Gas Separation Membrane", Catalysis Today, 148, 341-349 (2009)

¹ A. Nishimura et al., "CO₂ Reforming into Fuel using TiO₂ Photocatalyst and Gas Separation Membrane", Catalysis Today, 148, 341-349 (2009)